NON-INVASIVE BIOMEDICAL IMAGING AND RADIOBIOLOGY

INVESTIGATIONS IN PRE-CLINICAL PROSTATE

TUMOR MODELS

by

DEREK A. WHITE

Presented to the Faculty of the Graduate School of

The University of Texas at Arlington in Partial Fulfillment

of the Requirements

for the Degree of

DOCTOR OF PHILOSOPHY

THE UNIVERSITY OF TEXAS AT ARLINGTON

August 2015

Acknowledgements

First, I would like to thank my CREATOR for allowing me to make incremental progress in supporting my family and pursuing my chosen career. Second, I would like to acknowledge the wife of my youth and wonderful children. This dissertation is dedicated to them. It represents another commitment I have toward them. To my wife, Linda, te amo muñeca con una pasión cada desde la secundaria y yo sé que me amas lo mismo. Gracias por su paciencia y apoyo amoroso especialmente en las muchas actividades en las que participé . En consecuencia , yo realmente estar creen que estas cosas que me nutrieron con combustible añadido a mis ambiciones en la vida . To my children, Lauran, Elizabeth, Derek, and Trinity, I am proud to be your father and pray that you will not let anything or anyone hinder your goals in life. I would challenge you to exceed expectations and develop a legacy for your children. Third, I would like to give gratitude to my research mentor, Dr. Ralph P. Mason. His continued mentorship and scientific research training laid the foundation for me to acquire experience in hypothesis-driven research development and implementation leading to a hybrid independent research and clinical career in medical physics. Also, without the help of Dr. Mason's lab group I would have been totally lost so I truly am grateful for Rebecca, Jeni, Ramona, Zhongwei, Heling, and Li Li. Fourth, I would like to also acknowledge and thank my committee members for their consultation and suggestions. Dr. Hanli Liu, my graduate and medical imaging track advisor, for really taking the time to review my academic and professional status and encouraging me to follow through on commitments. Drs. Dawen Zhao and Ananth Madhuranthakam for their educational training on imaging modalities I use as applications for my investigations. Dr. Paul Medin for taking the time out of your very busy schedule to join my committee at the last minute when I needed to find a replacement committee member.

July 30, 2015

Abstract

NON-INVASIVE BIOMEDICAL IMAGING AND RADIOBIOLOGY

INVESTIGATIONS IN PRE-CLINICAL PROSTATE

TUMOR MODELS

Derek A. White, Ph.D.

The University of Texas at Arlington, 2015

Supervising Professor: Ralph P. Mason

Oxygen deficiency (hypoxia) in prostate tumors can hinder the biological effectiveness of radiotherapy. Therefore the ability to assess tumor hypoxia non-invasively *in vivo* in man could significantly improve therapy outcome. Magnetic resonance (MR) imaging is increasingly applied in clinical evaluation of prostate cancer. Therefore, an oxygen sensitive technique would be very attractive and the utility of oxygen-enhanced MRI (OE-MRI) has shown promise for predicting tumor growth delay in syngeneic rat prostate tumors following radiotherapy. In this dissertation, the overall goal was to investigate a potential imaging biomarker for predicting tumor response to image-guided radiotherapy (IGRT).

First, I used *in vivo* bioluminescence imaging (BLI) and *in vivo* ultrasound (US) imaging as cancer screening tools to follow the growth of subcutaneous and orthotopic human PC3-*luc* xenografts in nude rats. Surprisingly *in vivo* BLI signals were inconsistent despite growing tumors as revealed by US, MR imaging, or mechanical calipers. Nonetheless, they were ultimately available for OE-MRI.

Second, OE-MRI responses were acquired using a 4.7T small animal MR scanner in subcutaneous and orthotopic syngeneic Dunning R3327-AT1 and in orthotopic

human PC3-*luc* xenografts. OE-MRI responses showed potential for stratifying animals based on their "apparent" oxygen status.

Third, the rats with large AT1 tumors (tumor size ≥ 3 cm^3) were exposed to either air or oxygen during a single dose of x-rays consisting of 30 Gy and the results indicated that their tumor growth delay correlated with ΔR_1 and BOLD %ΔSI suggesting stratification. However, no extra growth delay benefit was shown when inhaling oxygen during irradiation suggesting that the influence of hypoxic cells on tumor radiosensitivity remained a major factor.

Fourth, I examined the influence of inhaling air or oxygen during a split-dose of x-rays with the same total dose of 30 Gy on small to intermediate (medium) sized tumors (0.5 cm^3 ≥ tumor size ≤ 3 cm^3). There were significant differences in the irradiated air or oxygen breathing groups and the unirradiated tumors. Inhaling oxygen during irradiation caused an increase in growth delay compared to inhaling air, suggesting a potential for modifying tumor hypoxia. Results showed significant correlations with tumor growth delay and pretherapy or between fraction OE-MRI responses. Increased OE-MRI responses after the first fraction of dose revealed tumor reoxygenation, which was confirmed by immunohistochemistry. Finally, a model for predicting tumor growth delay from split-dose fractionation was developed and validated.

Table of Contents

List of Illustrations

List of Tables

Chapter 1

Introduction

Common prostate cancer treatments include surgery (radical prostatectomy), hormonal therapy, chemotherapy, radiotherapy, or watchful waiting (active surveillance). Surgery involves removing the entire prostate gland in hope of curing prostate cancer. Hormonal therapy utilizes anti-androgens to block the production of androgens. Anti-cancer drugs are used for chemotherapy to combat advanced cancers when an individual is no longer responsive to hormonal therapy. Radiotherapy can be used as external (high energy photon beams) or internal (small radioactive seed implants or brachytherapy) sources for targeting prostate cancer. Considering that prostate examinations and treatments are so important in prostate cancer, it is important to improve early detection, treatment, and prevention of prostate cancer.

Despite the progress in prostate cancer management in recent years, approximately 220,800 American men are predicted to develop prostate cancer in 2015. Nearly 27,540 American men will die of prostate cancer, as estimated and reported by the American Cancer Society [1], which is an increase in estimated new cases (217,730). Furthermore, a decline in estimated deaths (32,050) since 2010 [2] is expected where the 5-year survival rate is now >99%. Prostate cancer screening and the development of new therapies seem to be two strategic methods to fight prostate cancer. Non-invasive imaging to assess the pathophysiology of the prostate has increasingly become the primary tool for experimental diagnostic imaging and therapeutics. The ability of biomedical imaging to non-invasively measure and characterize biological activities make it attractive to physicians. Moreover, monitoring prostate disease progression and assessing the efficacy of treatment non-invasively is powerful because it seeks to

1

determine the value directly related to the response of treatment and the early basis of local recurrence, respectively [3].

Patients identified at high risk of prostate disease progression and prostate cancer-specific mortality will have initial higher or rapidly rising serum PSA levels, biopsy Gleason scores, and the clinical stages of prostate cancer. These effects are considered the primary clinical prognostic factors that assist physicians with clinical assessments and decision making for prostate cancer treatment selections [3]. D' Amico *et al.* [4] determined that the short post-treatment PSA doubling time identified the high risk patients for prostate cancer-specific mortality after either radical prostatectomy or radiotherapy. In fact, pretherapy PSA and tumor grade have been evaluated as independent prognostic factors for stratifying patients or predicting treatment outcome [5]. Multivariate prognostic systems or predictive models for localized prostate carcinoma have been developed using multivariate statistical analysis to estimate patient treatment outcome following radiotherapy [6-8]. Adding the value of non-invasive imaging techniques can help stratify and identify those patients that will benefit from radiotherapy and forecast the patient's outcome [3].

There are many basic biomedical imaging modalities that have been experimentally used for assessing the treatment of tumors following radiotherapy. Each biomedical imaging modality comes with special imaging techniques that improve the ability to discern tumor progression or treatment-related changes. Common biomedical imaging modalities such as x-ray computed tomography (CT), magnetic resonance (MR) imaging, ultrasound (US), positron emission tomography (PET), and optics have be used to interrogate images of growing tumors and interventions. However, it is extremely difficult to identify tumors in the vicinity of normal tissue using CT because tumors have similar electron density to normal tissue. Consequently, absorption of photons from the

primary photon beam by the interactions with electrons in the tissue results in poor contrast between tumors and the surrounding normal tissue. On the other hand, MR imaging can provide excellent contrast between tumors and surrounding normal tissues because abnormal tissues such as cancer possess different physical parameters (spin density, longitudinal relaxation time (T_1), or transverse relaxation time (T_2) values) depending on the basic trio of parameters (flip angle (θ), echo time (TE), or repetition time (TR)) used in an image sequence; thus, more parameters to exploit for achieving high contrast. A drawback of MR imaging is that it requires a magnet and the cost to maintain this magnet is exceedingly expensive. Soft tissue contrast using US is fairly good, but the challenge of using US in soft tissues is in the limitation of the penetration depth at higher acoustic frequencies. The acoustic attenuation tends to decline as the frequency of the probe or transducer used increases. Thus, a trade-off would be to use lower frequencies to image a non-palpable prostate tumor but at the risk of a subjective interrogation of US images by the biased operator. Tumor metabolism and potentially treatment response can also be assessed by ^{18}F-Fluorodeoxyglucose Positron Emission Tomography ([18]FDG PET). However, [18]FDG PET requires the injection of a positron emitting radioisotope and the spatial resolution is poor compared to MR imaging. Optics for biomedical imaging uses non-ionizing light in the visible, ultraviolet, or infrared range as a radiation source. Small molecules such as tumor cells can be imaged in addition to tissues and organs. Optical imaging is limited due to tissue scattering and depth of tissue penetration.

As mentioned above, there are multiple biomedical imaging modalities that have been used experimentally for investigating the response of tumor treatment following radiotherapy. In regards to non-invasive assessments of the response of prostate cancer following radiotherapy, [18]FDG PET [9-12] and MR [13-17] imaging with specialized

techniques have extensively been investigated. For example, there have been correlations based on PET of radionuclide-labeled hypoxia markers and histology of biopsies, but to date there is no routine non-invasive approach available in the clinic to assess tumor oxygenation and help predict treatment outcome [18]. In addition, it is known that the outcome of radiotherapy is poor due to the presence of hypoxic cells which is a result of inadequate supply of oxygen to tumor cells [19]. Tumor hypoxia is increasingly regarded as an important factor and a potential prognostic biomarker for tumor aggressiveness and response to therapy [18]. The fundamental studies of Gray *et al*. demonstrated the influence of hypoxia on the response to radiation [20,21]. More recently, polarographic needle electrode measurements of pO_2 distributions and hypoxic fractions in patients confirmed poor outcome for hypoxic tumors in several disease sites including cervix [22-24], head and neck [25], and prostate [26]. Furthermore, there is direct evidence that hypoxic regions exist in human prostate carcinoma as investigated by Movsas *et al*. [27] using an Eppendorf electrode system to measure the partial pressure of oxygen (pO_2) in patients with prostate carcinoma. A decrease in oxygen measurements (pO_2) compared to normal muscle was observed and the fractions of hypoxia associated with oxygen measurements less than 5 mmHg (HF_5) or 10 mmHg (HF_{10}) correlated with clinical stage and the patient age [28] or biochemical failure (two consecutive rises in serum PSA levels without returning to baseline) [29] for those receiving implant radiation treatment or brachytherapy.

In terms of radiotherapy, hypoxia is increasingly recognized to play a fundamental role in resistance [30]. Hitherto, there has been no satisfactory approach to assessing hypoxia non-invasively to allow effective treatment planning based on hypoxia. Indeed, the meta-analysis of Overgaard *et al*. [31] indicated that interventions to overcome hypoxia provided a marginal benefit, but it was concluded the lack of efficacy

was likely related to the inability to identify, which patients would benefit. Consequently, attempts have been made to incorporate measurements of tumor oxygenation by means of non-invasive advanced imaging techniques for patient stratification [30,32-35] and many pre-clinical studies are underway to develop and validate novel methods [36-41].

Radiation oncologists and medical physicists have made significant contributions to accurately irradiate tumors with the precise targeted radiation while minimizing damage to neighboring healthy tissue [42]. Advanced medical imaging application techniques in radiotherapy of cancer patients provided innovative treatment applications such as image-guided radiation therapy (IGRT) or intensity-modulated radiation therapy (IMRT). As radiation oncologists and medical physicists are increasingly faced with complex treatment of cancer due to a tumor's adaptability, it has become more important to develop innovative applications to implement the destruction of cancer cells without destroying normal cells while maintaining acceptable radiation tolerances [18,21]. This has led to innovative radiotherapy treatments such as hypofractionated radiotherapy where a few high doses are delivered, as opposed to the conventional six-week course of treatment [18,21]. Remarkable results have been shown in non-surgically resectable advanced lung cancer [43] and the approach is being evaluated in many diverse diseases sites including prostate. This method provides a better therapeutic outcome for cancer patients undergoing radiotherapy treatments.

Traditionally, the practice of fractionationed radiotherapy relies on the so-called biological factor: the five Rs (radiosensitivity, repair, repopulation, redistribution, and reoxygenation). Reoxygenation allows hypoxic cancer cells to be more radiosensitive through the practice of fractionation radiotherapy from subsequent radiation doses. Since it has been determined that complete reoxygenation of cancer cells cannot be accomplished by fractionation alone, the diffusive movement of oxygen delivered to the

tumor hypoxic cells can enhance the efficacy of radiation cancer treatment. Consequently, it is important to measure the dynamics of an individual tumor's oxygenation directly when treating it with oxygen to enhance radiosensitivity.

New hypofractionated treatment approaches are gaining interest for several reasons: i) fewer treatment sessions are convenient to patients and physicians; ii) precise treatment plans may be developed for each irradiation; iii) recent clinical trials are showing enhanced outcome [43]. However, it is thought that hypoxia will be particularly crucial especially when implementing large single- or multi-fractional dose regimens used by SBRT (stereotactic body radiotherapy), since there is no opportunity for tumor reoxygenation as thought to accompany with traditional CFRT (conventional fractionated radiation therapy) [44,45].

There is evidence that Oxygen-Enhanced MRI (OE-MRI) may give insights into tumor hypoxia and appropriate interventions designed to modify hypoxia [22,23,25,26,46-50]. Hallac *et al*. discovered interesting correlations among oxygen-sensitive parameters such as dynamic percent signal intensity changes from blood-oxygen level dependent (BOLD) and tissue-oxygen level dependent (TOLD) images obtained from syngeneic Dunning R3327-AT1 prostate tumors implanted subcutaneously in Copenhagen rats and termed this imaging technique as the interleaved BOLD/TOLD or IBT. In addition, the investigators noticed a correlation with the apparent transverse relaxation rate (ΔR_2^*). A comparison against change in partial pressure of oxygen (ΔpO_2) measurements obtained from the Fluorocarbon Relaxometry using Echo planar imaging for Dynamic Oxygen Mapping (FREDOM) was tested against these parameters and found to correlate [37]. Also, other investigators have reported changes from both the intrinsic longitudinal relaxation rate (ΔR_1) and the apparent transverse relaxation rate (ΔR_2^*) in a diverse group of tissues [51] and tumors [35,37,49,52]. These parameters were compared

6

against oxygen electrode measurements [24,48,53], nuclear medicine methods such as positron emission tomography [48,53], phosphorescence quenching [54], and immunohistochemistry [26,50].

Thus, investigating tumor radiobiology non-invasively has clinical relevance and biomedical image analysis of tumor oxygenation is novel, feasible, and potentially useful. Consequently, the overall goal of my research was to find imaging biomarkers for predicting tumor response non-invasively to hypofractionated radiotherapy using IGRT. The benefit of such a prediction will allow radiation oncologists and medical physicists to use it as a prognostic factor during the course of radiotherapy treatment planning. My investigations include extending studies from the work implemented by Hallac et al. [37]. I investigated syngeneic Dunning R3327-AT1 prostate tumors implanted subcutaneously in Copenhagen rats, a well-established and effective model that has been used for assessing tumor hypoxia. I extended investigations to large subcutaneous tumors, orthotopically implanted tumors, and for a split-dose fractionation scheme. I also extended investigations to human tumor xenografts (specifically, prostate PC3) implanted subcutaneously or orthotopically in adult male nude rats. My research effort aimed to gather experimental data that will answer the following questions: (1) can the tumor oxygenation of a subcutaneous or orthotopic prostate tumors be measured and quantified under dynamic hyperoxic gas conditions? (2) can OE-MRI be exploited to quantify and assess tumor hypoxia non-invasively as an imaging biomarker? (3) can the response to radiation therapy be predicted utilizing OE-MRI? The answers to these questions may allow radiation oncologists and medical physicists to provide personalized radiotherapy treatment planning when considering tumor hypoxia, while improving the response to therapy.

My overall hypothesis is that OE-MRI can serve as a non-invasive imaging biomarker to predict tumor oxygenation and response to radiotherapy. However, individual hypothesis are strategically investigated as listed below:

**Hypothesis 1**: Non-invasive bioluminescence imaging (BLI) can detect subcutaneous or orthotopic PC3-luc prostate tumors and correlate with high frequency ultrasound (US) imaging.

Aim 1: Monitor the growth of subcutaneous and orthotopic PC3-luc prostate tumors using adult male nude rats. (**Chapter 3**)

Challenge: Differentiating prostate tumor tissue from normal prostate tissue in ultrasound images for tumor volume measurements.

Approach: Tumor growth was monitored _in vivo_ using BLI and US. I compared _in vivo_ BLI signal intensity with US tumor volume measurements.

Impact: Monitoring the growth of prostate tumors non-invasively and characterizing the type of tissue of sub-palpable orthotopic tumor models should allow implementing efficient tumor radiobiological studies in the future and for the following hypothesis (Hypothesis 2).

**Hypothesis 2**: _In vivo_ OE-MRI responses to oxygen can be validated using non-invasive global pulse oximetry arterial oxygen saturation (SpO_2) measurements.

Aim 2: Quantify and assess tumor oxygenation non-invasively using Oxygen-Enhanced MRI (OE-MRI) as a basis of predicting the response (tumor growth delay) to radiation. (**Chapter 4**)

Challenge: Tumor microenvironment can complicate the spatial and temporal measurements of tumor oxygenation due to noise.

Approach: Use digital image processing methods to assess increased signal intensities to inhaling oxygen on OE-MRI images. Validate results with global pulse oximetry arterial oxygen saturation (SpO_2) measurements.

Impact: Non-invasively quantifying tumor oxygenation can be establish as an imaging biomarker for tumor hypoxia.

Hypothesis 3: a) OE-MRI parameters from Specific Aim 2 are correlated with radiation response; b) Breathing oxygen can modify the response to radiation.

Aim 3: Evaluate the usefulness of OE-MRI to predict tumor radiation damage or response to radiation for translation to clinic. (**Chapters 5 and 6**)

Challenge: Tumor hypoxia can influence the response to radiation.

Approach: Gross tumor volume (GTV) will be irradiated using image-guided radiation treatment (IGRT). Tumor growth delay (TGD) will be compared to OE-MRI responses prior to irradiation. Develop a multivariate regression model to predict the response of prostate tumors to radiotherapy.

Impact: Improving radiotherapy treatment planning by providing individual evaluation of tumors before the implementation of radiation treatment.

I will wrap up the dissertation with **Chapter 7** discussing some potential pitfalls, future work, and conclusion.

Chapter 2

Fundamentals and Methodology

Introduction

Scientists and engineers are using non-invasive biomedical imaging to interrogate tumor vasculature and oxygenation to understand their effects on cancer radiation therapy. Bioluminescence (BLI), ultrasound (US), and magnetic resonance (MR) are powerful non-invasive biomedical imaging applications that are being explored for such a task. In this chapter, I discuss the unique make-up of tumor's microenvironment and a selection of biomedical imaging applications I chose to use for my investigations. This chapter is based on the books by Giancoli [55], Pittman [56], Silverthorn [57], Garrett [58], Hall [18,59], Khan [60], Griffiths [61], and Nishimura [62].

Oxygen Transport to Tumors

The amount of oxygen that can be dissolved in blood is an important factor for transporting available oxygen to tissue for metabolic activity. Oxygen generally has low solubility in any aqueous solution. Consequently, low solubility of oxygen is the reason why > 98% of oxygen is carried in the arterial blood by hemoglobin and < 2% by plasma (Figure 2.1).
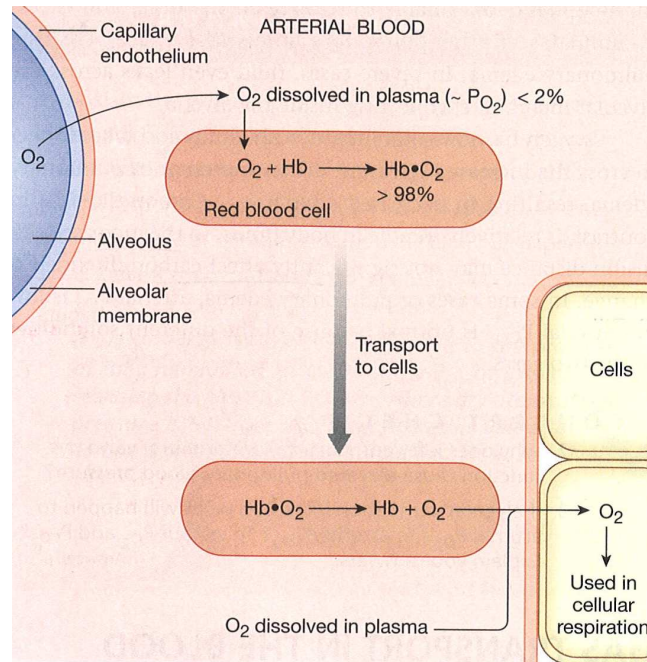
Figure 2.1 Oxygen Transport in the Blood (Figure adapted from Silverthorn [63].)

The partial pressure of oxygen (pO_2) is directly proportional to the amount of oxygen gas molecules dissolved in the blood as shown in Equation 2.1 where $[O_2]$ is the concentration of dissolved oxygen and α is the solubility of oxygen according to the Henry's Law [64]. Typically, oxygen gas will be directed to low areas of partial pressure from high areas of partial pressure. Higher areas of pO_2 exist in the alveolae of the lungs at approximately 100 mmHg assuming normal mechanics of respiration and gas exchange. Whereas, lower pO_2 exists in the far reaches of tissue capillaries at approximately 40 mmHg, since tissue cells are continuously consuming oxygen for oxidative phosphorylation [58,63]. Thus, oxygen diffuses from blood to tissue cells due to a partial pressure gradient across the capillary wall as shown in Figure 2.2.

$$[O_2] = \alpha \, pO_2 \qquad\qquad\qquad 2.1$$
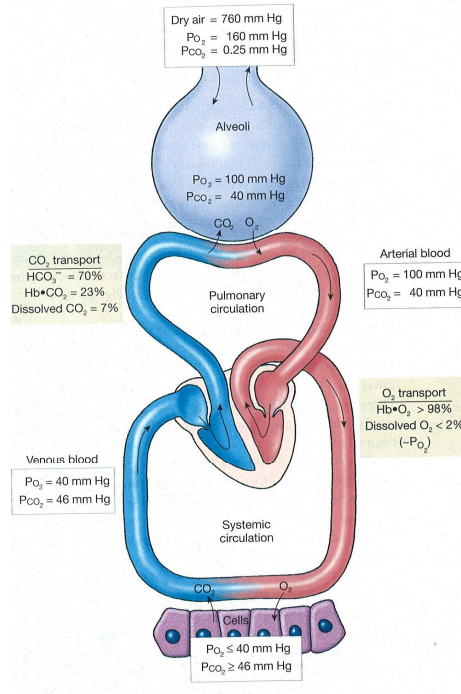
Figure 2.2 pO_2 Transport in the Blood (Figure adapted from Silverthorn [63].)

Tumor Physiology

Tumor microenvironment is known to be different than normal tissue [65]. Solid tumor vasculatures tend to be meandering and irregular in shape, lacking the basic internal surface elements such as an endothelial layer to interface with circulating blood [66] as illustrated in Figure 2.3. The microcirculation of solid tumors is leakier compared to normal tissue and tends to have sluggish blood flow where the oxygenation in the tumor becomes limited varies in location [67]. Consequently, the factors that determine the pO_2 in tumors consist of 1) the blood flow rate to tumors; 2) the oxygen content delivered to tumors; 3) the three-dimension (3D) capillary distribution network of tumors; and 4) the rate of consumption of tumors [68-72].
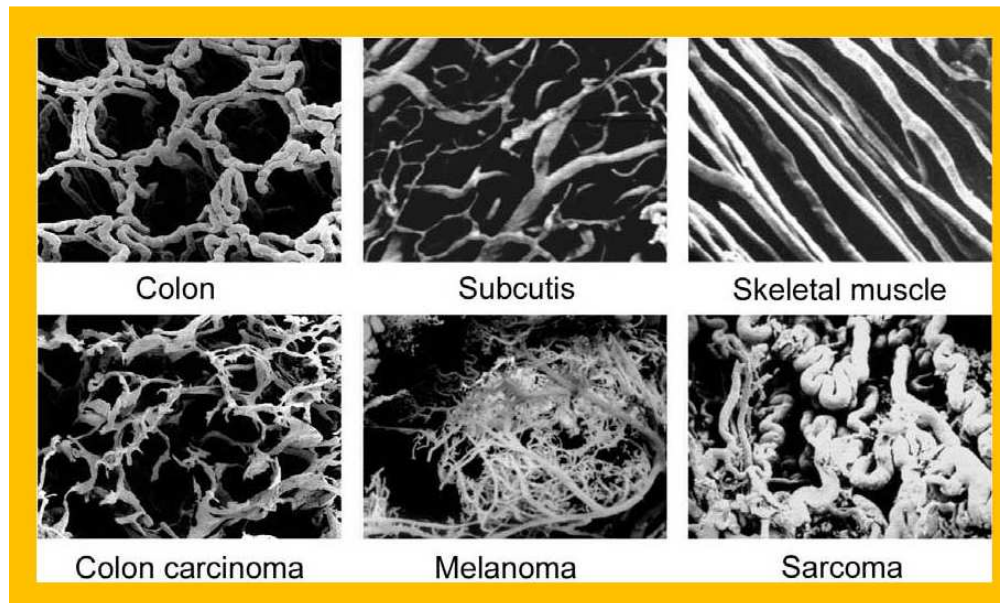
Figure 2.3   Illustrations in vascular differences between normal tissue (top row) and tumors (bottom row) (Figure adapted from Vaupel [65].)

Tumor Hypoxia

The presence of oxygen during irradiation has been a topic of investigation since the early 1950's [20]. Tumor hypoxia has been found to affect the response to radiation therapy [25,37,73] because hypoxic cells resist radiation damage up to 3 times compared to normal cells [20]. **Consequently, investigating tumor radiobiology non-invasively has clinical relevance**.

Tumor Radiobiology

The physical process of converting a neutral molecule into an ion is called ionization by the absorption of energy [59]. This process involves adding or removing charge particles such as electrons. External ionizing radiation used most often are

13

electromagnetic (EM) waves such as x-rays (photons) or gamma (γ)-rays. EM waves of this kind tend to have high frequencies and short wavelengths. They travel individually as high-energy packets [74]. The production of x-rays is accomplished by heating a cathode (filament) that emits electrons in a vacuum tube. The emitted electrons collide with a target (high atomic number material such as tungsten) producing characteristic and bremsstrahlung photons where the maximum photon energy produced at the target equals the kinetic energy of the electrons striking the target. An illustration (Figure 2.4a) and photo (Figure 2.4b) regarding the schematic design of an x-ray tube is shown in Figure 2.4. X-ray beams can be produced for diagnostic (10 – 150 kVp) purposes or for therapeutic (1 – 50 MV) purposes. Other forms of radiation include the production of electrons, protons, and other heavy charge particles such as carbon ions [59]. To be of valid use for radiotherapy, heavy charge particles must be accelerated significantly to high energies (> 100 MeV per nucleon) for sufficient therapeutic outcome.

Tumor radiobiology is investigated by directing ionizing radiation through living material. The overall goal of using ionizing radiation for investigating tumor radiobiology is to introduce radiation damage where energy is deposited into biological material to elicit a biological response. Gray *et al.* [20] investigated the response of cells to ionizing radiation and discovered that there was a significant biological response that depended on the presence of oxygen during irradiation. There have been numerous *in vitro* experiments that illustrated the effect of oxygen during irradiation [75,76] and that oxygen has the capabilities of modulating the radiosensitivity of mutant cell lines [77] as a function of dose and cell cycle phase.
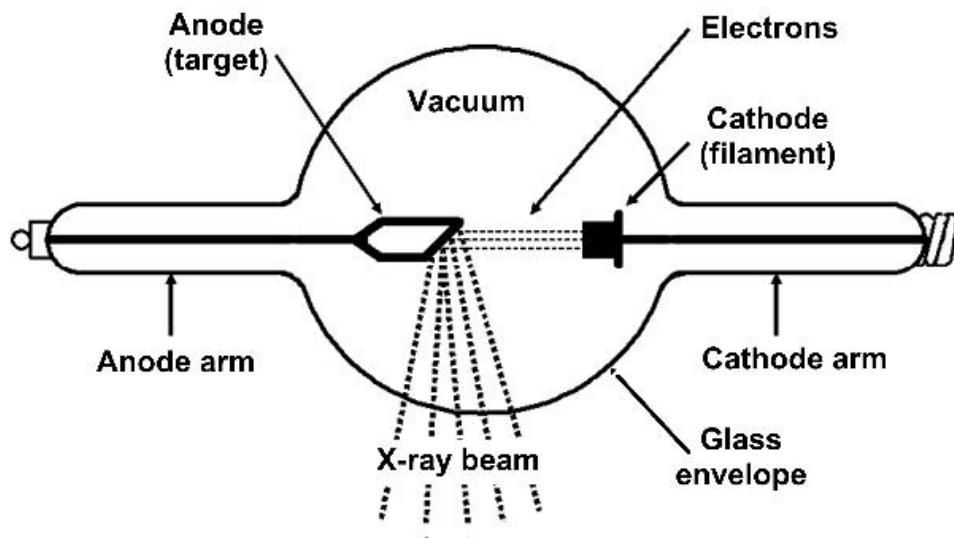
(a)

(b)

Figure 2.4 Common X-ray Tube illustrates (a) the schematic design and corresponding photo (b) used today in the clinic. (Figure adapted from Podgorsak *et al.* [78].)

Freyer *et al.* [77] were able to separate cells to pure populations of cell cycle phases under oxic and hypoxic conditions and the oxygen enhancement ratio of proliferating cells was found to depend on the particular cell cycle phase (Table 2.1). An illustration of a survival curve [79] of mammalian cells irradiated in cell culture under oxic or hypoxic conditions is shown in Figure 2.5. To achieve the same biological effect, the oxygen enhancement ratio (OER) can be determined by the following equation:

$$OER = \frac{RADIATION\ DOSE\ IN\ HYPOXIA}{RADIATION\ DOSE\ IN\ AIR} \qquad 2.2$$

The values of OER have been found to be in the range of 2.5 to 3.5 [59] but it was discovered that it is lower (Figure 2.6) for radiation doses below 3 Gy [80]. It is known that the OER increases with increasing partial pressure of oxygen (pO_2) as indicated by the range of physiological blood oxygen tension [79]. The OER is approximately 1.5 for pO_2 = 10 mmHg and 3.0 for pO_2 = 100 mmHg.

Table 2.1 Oxygen Enhancement Values for CHO-xrs6 Cells at Different Survival Levels as a Function of Cell Cycle Position (Table adapted from Freyer *et al*. [77])

Surviving fraction	Oxygen enhancement ratio				
(%)	Total	G_1 phase	G_1/S phase	S phase	G_2 phase
> 50	2.41 ± 0.085	2.31 ± 0.21	2.42 ± 0.22	2.97 ± 0.16	2.68 ± 0.31
< 10	2.89 ± 0.062	2.34 ± 0.098	2.86 ± 0.034	2.95 ± 0.11	2.78 ± 0.35
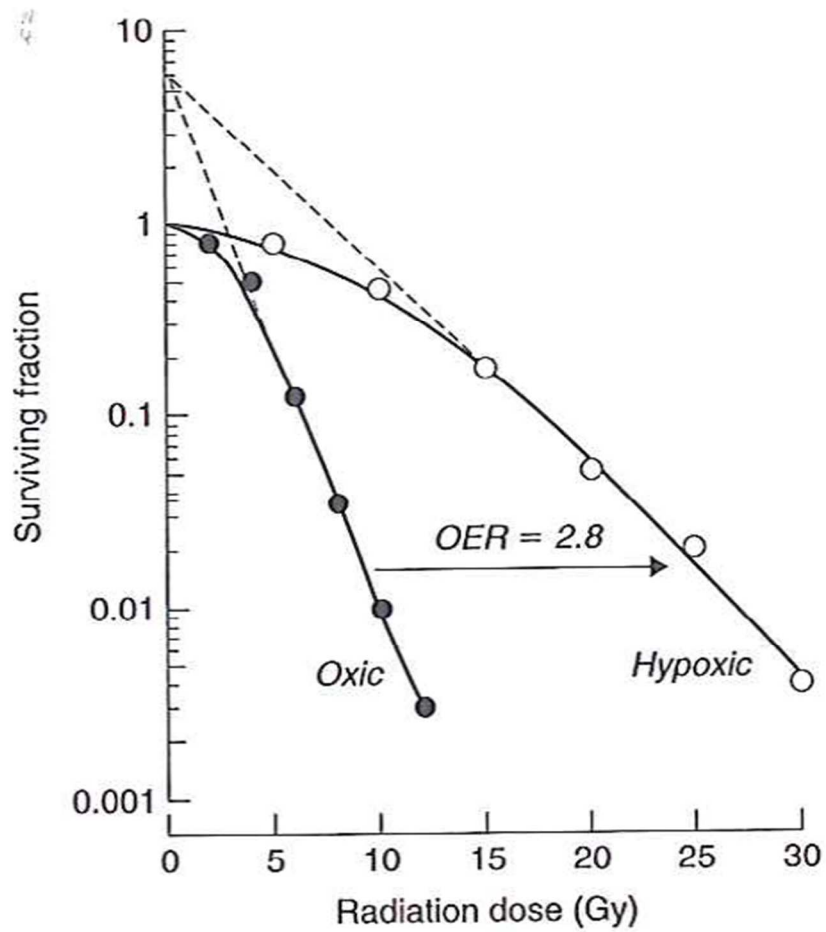
Figure 2.5 Oxygen Enhancement Ratio. Survival Curves for cultured mammalian cells exposed to X-rays with respect to oxic or hypoxic conditions, illustrating the radiation dose-modifying effect of oxygen. The curves extrapolate back to the same point to the surviving fraction axis (n = 6) (Figure adapted from Michael *et al*. [79]).
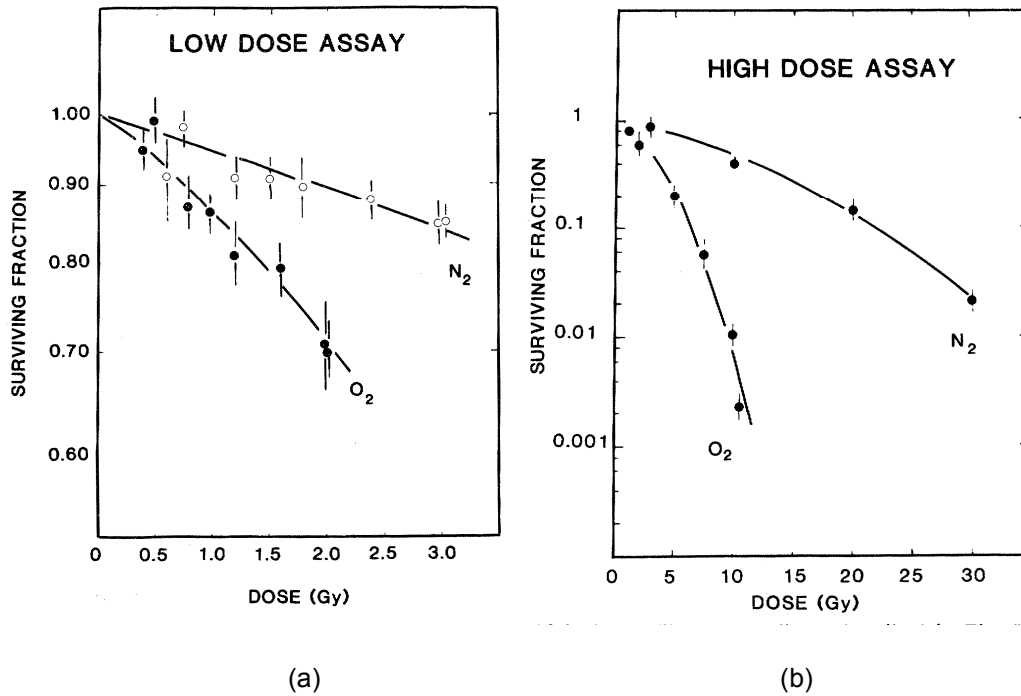
Figure 2.6 Oxygen Enhancement Ratio of CHO cells under hypoxic and oxic conditions as a function of (a) low dose and (b) high dose. Survival curves indicate that at SF = 0.9 survival at low doses the OER is assumed to be of value equal to 2.5 and the OER is assumed to be 3.5 at SF = 0.2 (Figure adapted from Palcic *et al*. [80]).

The tumor microenvironment plays an important role during the time of treatment [66]. Cell survival differences have been demonstrated in irradiated mammalian cells under aerated conditions compared to hypoxic conditions [79]. However, there is debate about what pO_2 level to use for distinguishing tumor hypoxia [81].
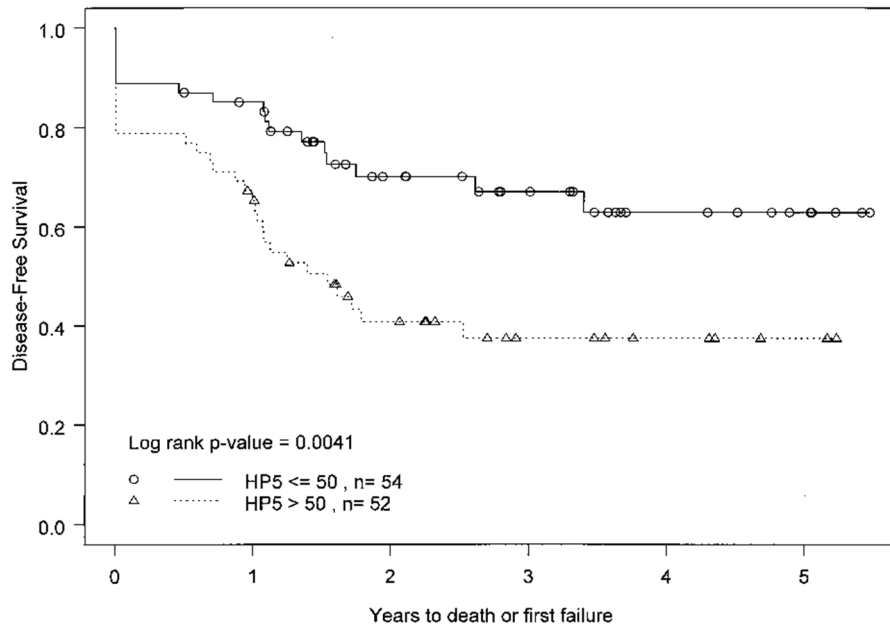
Figure 2.7 Survival probability for patients undergoing external-beam radiotherapy as a primary treatment of uterine cervix cancer (Figure adapted from Fyles *et al*. [81]).
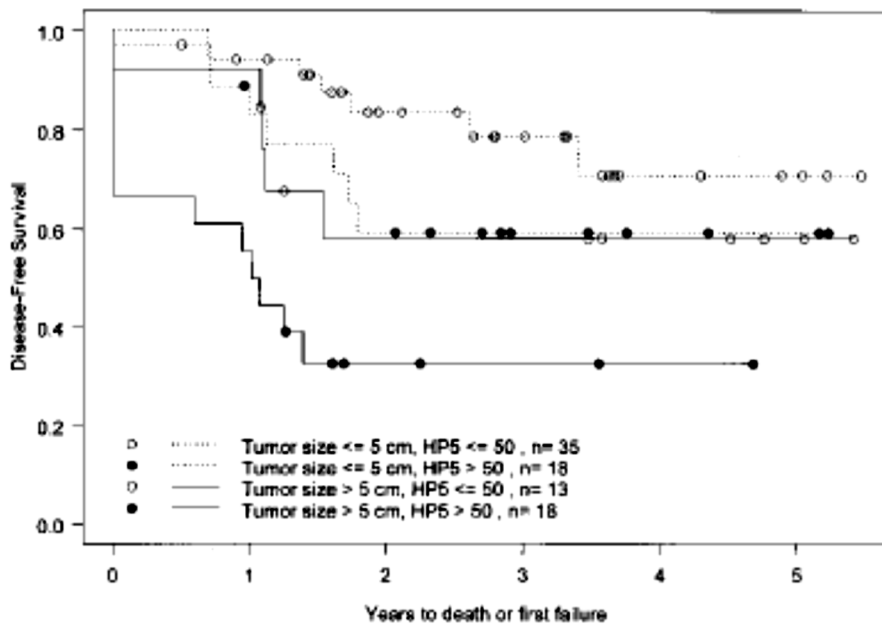
Figure 2.8 Survival probability for patients stratified by tumor size and hypoxic status (Figure adapted from Fyles *et al*. [81]).

Fyles *et al.* [81] evaluated patients with cervical cancer shown in Figure 2.8 with a hypoxic fraction (HF_5) at 5 mmHg. Figure 2.9 illustrates patients stratified by tumor size and hypoxic status indicating that patients with small tumors that are well-oxygenated will have a greater survival rate compared to patients with large and poorly-oxygenated tumors. Parker *et al.* [82] stratified prostate cancer patients using HF_5 from polarographic electrode (pO_2) measurements. Movsas *et al.* [83] stratified patients with prostate cancer to muscle ratios determined from pO_2 measurements and to predict biochemical control. With evidence that the tumor microenvironment may play an important role to prolong survival of patients undergoing radiation treatment, tumor physiology has been investigated [66] to determine which factors are predominately candidates in hindering the survival rate of patients.

As mentioned previously, tumor physiology is different than normal tissue [66] where tumor vasculature is highly irregular in shape or meanders in zigzags (Figure 2.9). The smooth muscle has not been seen in tumor vasculature compared to normal tissue and the endothelial lining and basement membranes are incomplete. The mechanism of tumor angiogenesis does not compensate for these inefficiencies for adequate oxygenation. The tumor microcirculation is inactive with sluggish blood flow. Since the tumor vasculature suffers from an incomplete endothelial lining and lack of smooth muscle, the tumor microcirculation will be leakier than normal tissue. Consequently, heterogeneity in tumor oxygenation (Figure 2.10) has been observed. Tumor cells may be classified as chronic hypoxia because of diffusion-limited delivery of oxygen to hypoxic cells at around 70 μm (Figure 2.11). Acute hypoxia occurs from perfusion limitation of oxygen delivery where blood vessels are temporarily closed. A steal effect process [84] where blood and consequently oxygen is redirected to normal tissue blood vessels has also been suggested as a reason for reduced tumor perfusion. Tumor hypoxia also

appears to stimulate mutations [85]. Consequently, some important independent indicators would be an aggressive tumor phenotype, the clinical stage of the tumor where it has been discovered that as a tumor grows so does the hypoxic fraction of the tumor [86], as a potential prediction of radiation response. It is clear that the important determination of tumor hypoxia may be responsible for the malignant behavior of cancers or response to radiation therapy or both. The presence of oxygen is required for the mechanism of the oxygen effect to be implemented either during or within a few microseconds after irradiation [59]. Consequently, in the presence of oxygen the damage to tumor DNA can become "fixed". Reoxygenation (Figure 2.12) between dose fractions is another investigated topic regarding the oxygen effect where the hypoxic cells that resisted radiation can become oxygenated due the cell kill of well-oxygenated tumor cells and restructuring of tumor vasculature from angiogenesis after irradiation [59].

— 100 µm

Figure 2.9 Image of tumor microvasculature of large rat DS-sarcoma (Adapted from Tatum *et al*. [66]).
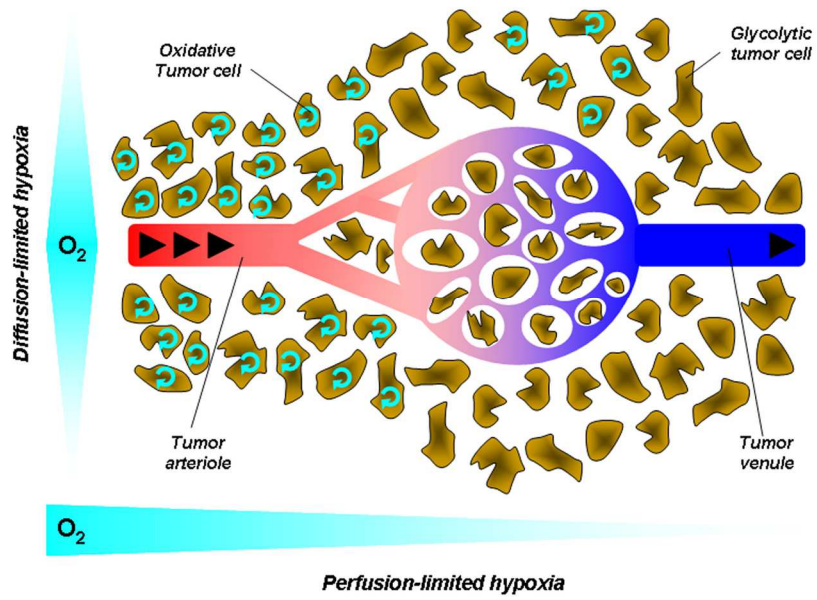
Figure 2.10 Tumor hypoxia microenvironment with respect to oxygenation (Adapted from Jorden *et al*. [84]).
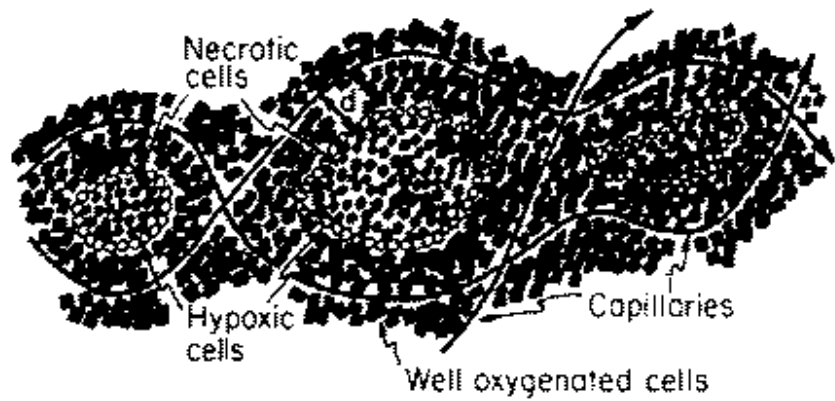
Figure 2.11 Illustration of the tumor microenvironment. Tumor cells that are beyond the diffusion distance (70 µm) from capillaries become hypoxic cells. As the tumor grows, the tumor can become necrotic and die (Adapted from Cunningham *et al*. [86]).
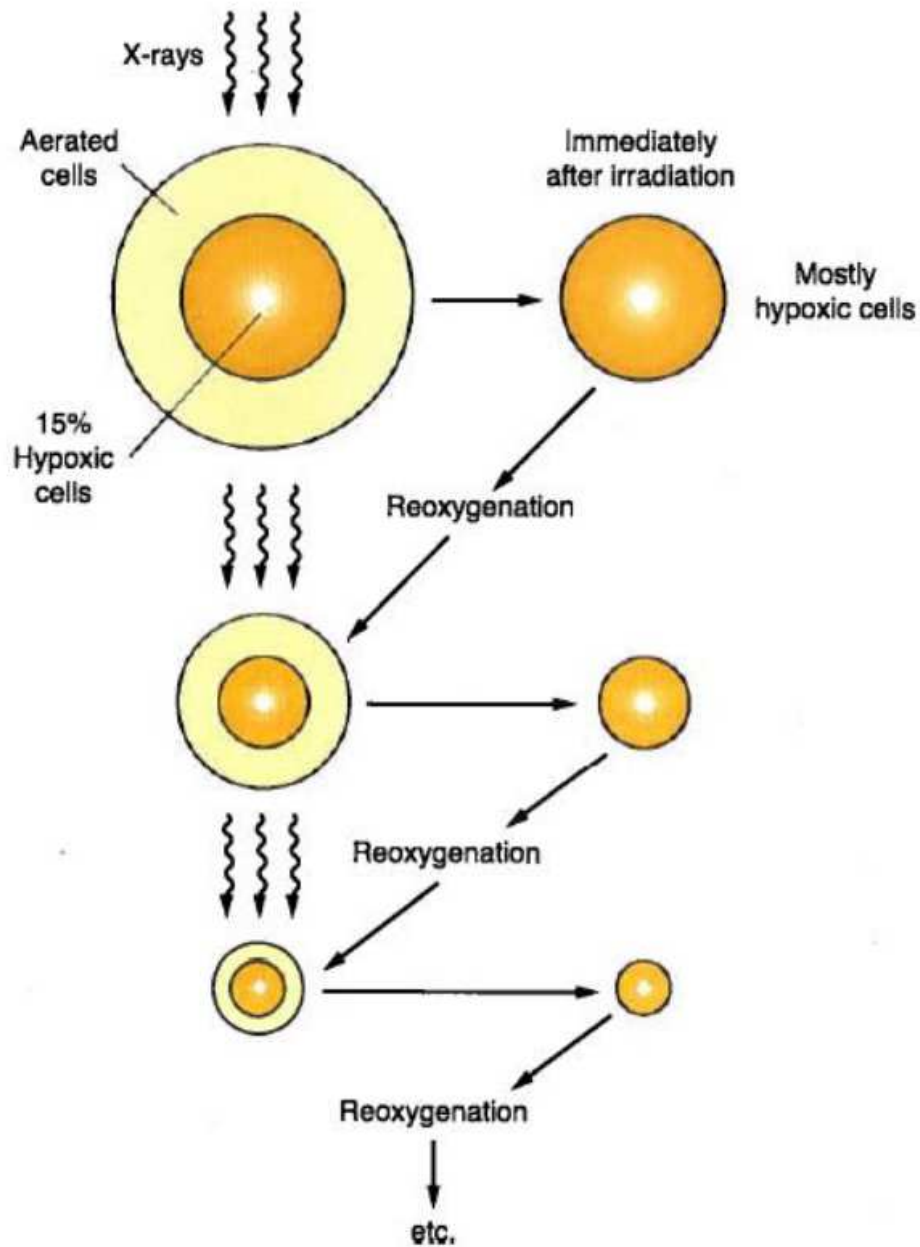
Figure 2.12 Tumor reoxygenation process when containing a mixture of well-oxygenated tumor cells and hypoxic cells. The well-oxygenated cells are destroyed while hypoxic cells remain and acquire access to oxygen to become aerated. Tumor shrinks during reoxygenation (Adapted from Hall *et al*. [59]).

However, the change in tumor morphology after irradiation with 5 Gy has been demonstrated [87] in R3230 Ac mammary adenocarcinoma in rats. Furthermore, Diepart et al. [88] investigated tumor reoxygenation in liver (TLT) tumors by administering arsenic trioxide (As_2O_3) in mice to inhibit mitochondria respiration. A decrease in tumor perfusion was demonstrated using Patent blue staining assay 90 minutes after As_2O_3 injection, suggesting decreased oxygen consumption of tumor cells after chemotherapy. In addition, doses > 10 Gy has shown to cause tumor vascular effects in syngeneic rat breast tumors (Walker 256 carcinoma) by increasing the vascular permeability several days after irradiation [89,90]. Song et al. [89] reasoned that tumor growth delay in response to irradiation was partly related to poor blood circulation due to tumor vascular damage. Thus, tumor reoxygenation may be the cause of decreased oxygen consumption by tumor cells and not from improved blood circulation caused by angiogenesis as speculated. Because of vascular damage, sufficient tumor reoxygenation may be absent after tumors are treated with high doses in Stereotactic Body Radiotherapy (SBRT) [90-92]. Consequently, diminished tumor reoxygenation may be countered using oxygen breathing during irradiation [93].

The effect of oxygen has demonstrated clear significance in terms of the response to radiation. Non-invasive methods to interrogate the microenvironment of tumors are becoming a significant need to stratify those patients that would benefit from radiotherapy. In addition, radiotherapy treatment planning systems such as Intensity-Modulated Radiotherapy (IMRT) will be more robust since biological spatial measurements of interrogated tumors will be readily available from the stratified patients, thus, providing more effective treatment planning. Consequently, investigating tumor radiobiology without invasive measurements has clinical relevance.

Bioluminescence Imaging

In this dissertation, *in vivo* bioluminescence imaging (BLI) was implemented to monitor the growth of subcutaneous and orthotopic prostate tumors for extended cancer studies. BLI was intended to non-invasively monitor increasing BLI signals over time as indicative of growing tumors. Bioluminescence occurs by a chemical reaction *in vivo* where the firefly luciferase enzymes act as catalysts for the production of light. The use of luciferase requires gene transfection of cells with a promoter (Figure 2.13). Substrate injections with D-luciferin and in the presence of oxygen (O_2) and cofactors (magnesium and adenosine triphosphate or ATP) are required for light production. The light emitted from bioluminescence is detected using a charge-coupled device (CCD) camera. Figure 2.14 illustrates a typical setup used in my investigations for *in vivo* BLI as previously described [94].
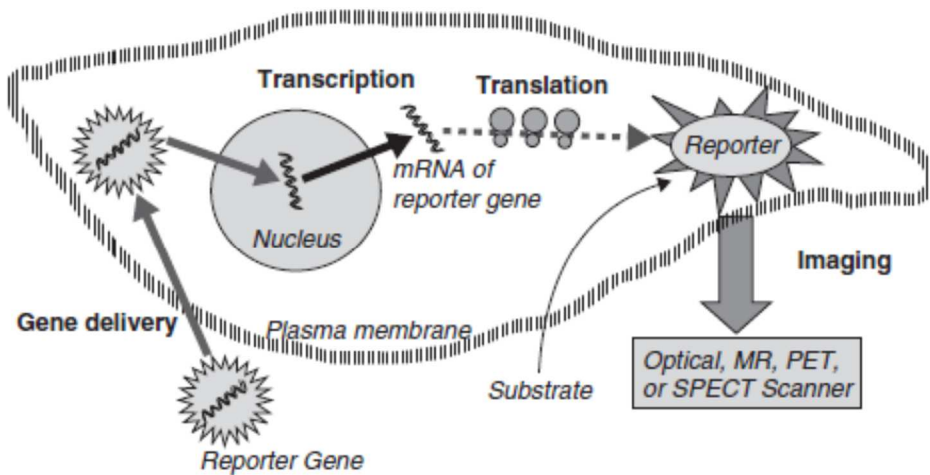
Figure 2.13 Overview of *In Vivo* Bioluminescence Imaging. The luciferase gene in the cell is transcribed and translated for subsequent imaging (Adapted from Feng [95]).
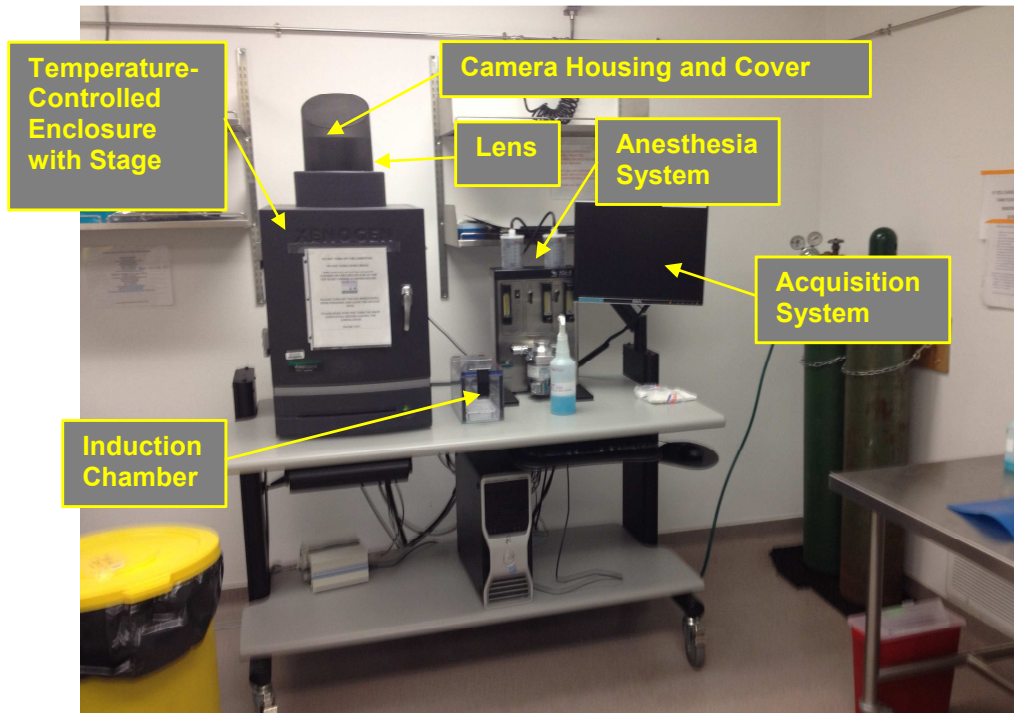
Figure 2.14 Photo of *in vivo* BLI setup using the IVIS® Lumina Imaging System

High-Frequency Ultrasound Imaging

Non-invasive experimental measurements of acoustic propagation parameters (sound speed, impedance, absorption, scattering, or attenuation) in biological tissue has been a topic of investigation since the early 1950's . Small animal or pre-clinical cancer research studies often rely on cancer cells implanted subcutaneously or orthotopically. Monitoring the growth of orthotopic tumors implanted in the prostate of small animals can be a challenge and using US as the initial step for implementing long-term pre-clinical cancer research studies is attractive. Consequently, non-invasive *in vivo* ultrasound

images were acquired using a pre-clinical high-frequency ultrasound system to correlate the results of *in vivo* BLI signals over the evolution of subcutaneous and orthotopic prostate tumor growth. Figure 2.15 illustrates a typical setup used in my investigations for acquiring *in vivo* ultrasound images.
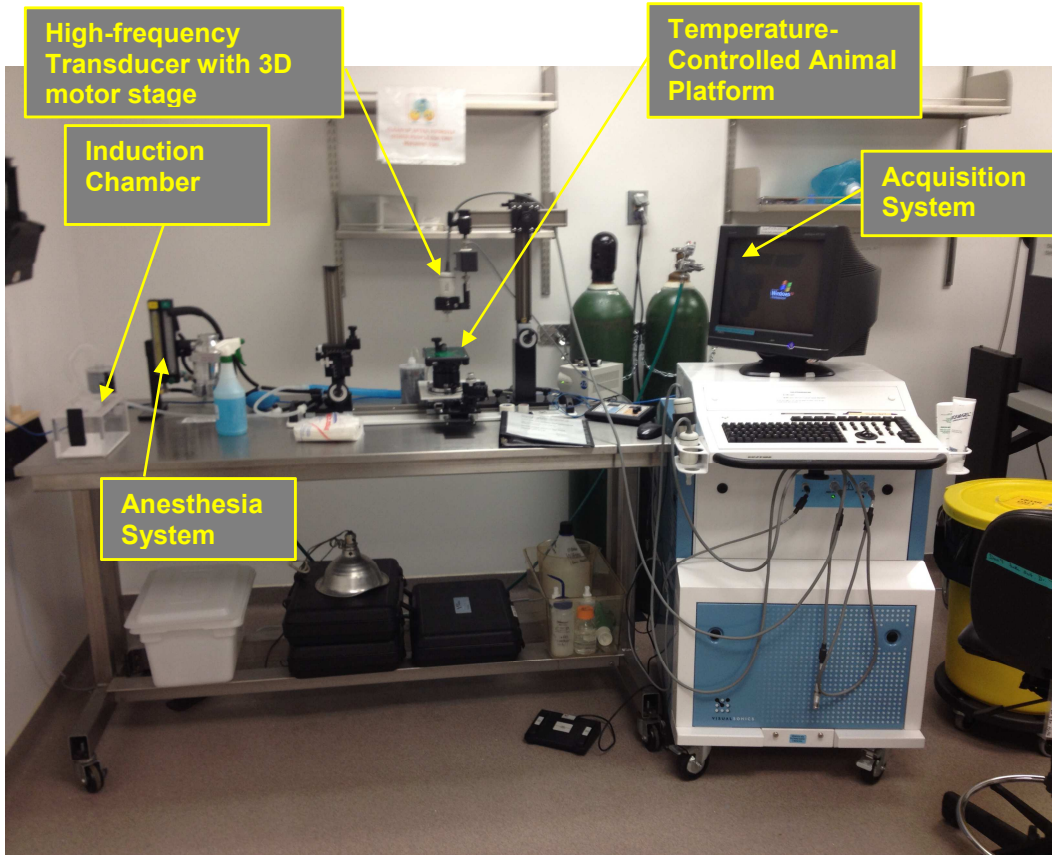
Figure 2.15 Photo of *in vivo* ultrasound imaging setup using the VisualSonics Vevo 770® High-Resolution *In Vivo* Micro-Imaging System

Oxygen-Enhanced Magnetic Resonance Imaging

Oxygen-Enhanced Magnetic Resonance Imaging (OE-MRI) is a non-invasive magnetic resonance (MR) imaging technique used to measure static or dynamic

responses to inhaling oxygen or carbogen relative to a baseline of inhaling air. OE-MRI exploits the basic principles of nuclear physics, electromagnetism (E&M), and MR imaging. Protons (abundant in tissue) have nuclear spin and precession when placed into an external magnetic field (B_o) forming nuclear magnetic dipole moments. Nuclear magnetic dipole moments from protons are dictated by the laws of quantum mechanics and can be detected by measuring the radiofrequency (RF) power emitted at proton resonance or Lamor frequency $(f) = \frac{\gamma}{2\pi}B_o$. The gyromagnetic ratio (γ) of the proton nucleus is $\frac{\gamma}{2\pi}$ = 42.577 MHz / Tesla. Consequently, protons in tumor tissue can be measured at a resonance frequency of approximately 200.112 MHz in a 4.7T small animal magnet scanner. A net magnetization (**M**) vector in the direction of B_o and in equilibrium represents the many nuclear magnetic dipole moments that exist in tumor tissue. Using a rotational frame behavior, a MR signal can be measured by applying an RF pulse or excitation angle tuned to 200.112 MHz in the transverse or *xy* plane of the **M** vector to perturb its equilibrium condition. The measurement of the **M** vector is governed by the principles of electrodynamics when the **M** vector precesses about B_o located along the *z*-axis. An RF coil can be used as a transmitter and receiver of the MR signal based on Faraday's (1831) ingenious creativeness:

A changing magnetic field _induces_ an electric field

Faraday demonstrated that the electromotive force (emf) or voltage potential is equal to the change in flux (Φ) with respect to time [61]:

$$emf = \oint \boldsymbol{E} \cdot \boldsymbol{dl} = -\frac{d\Phi}{dt} \qquad\qquad 2.3$$

$$\Phi = \int \boldsymbol{B} \cdot d\mathbf{a} \qquad \text{2.4}$$

where the $\boldsymbol{E}$ vector is the electrical potential integrated around a closed path. Consequently, the MR signal (as a function of time) that is measured in the RF coil is referred to as the free induction decay (FID). The behavior of the **M** vector is described by the following Bloch [96] equation:

$$\frac{d\boldsymbol{M}}{dt} = \boldsymbol{M} \times \gamma\boldsymbol{B} - \frac{M_x\mathbf{i} + M_y\mathbf{j}}{T_2} - \frac{(M_Z - M_O)}{T_1} \qquad \text{2.5}$$

where M_o is the equilibrium magnetization from B_o, the $\boldsymbol{B}$ vector represents various magnetic fields, and **i, j,** and **k** are unit vectors in the x, y, and z directions. The first term to the right of Equation 2.5 is the precession behavior of the **M** vector as a function of time as described by the curl. The next terms are exponential behavior for transverse and longitudinal relaxation components. The transverse component is the measured response when the **M** vector is perturbed to the xy plane. This component decays after the RF pulse is applied while the longitudinal component re-establishes the equilibrium condition. The solutions to the precession and relaxation components can be determined [62].

As mentioned previously, the $\boldsymbol{B}$ vector represents various magnetic fields. These nonuniform magnetic fields are time-varying gradients (**G** vectors) applied in the xyz directions of the tumor tissue to determine the relaxation times T_1 and T_2 from the following signal equation making MR imaging possible.

$$MR\ Signal = \int_x \int_y m(x,y)e^{-j2\pi[k_x(t)x+k_y(t)y]}\,dx\,dy \qquad\qquad 2.6$$

where

$$k_x(t) = \frac{\gamma}{2\pi}\int_0^t G_x(\tau)\,d\tau$$

$$k_y(t) = \frac{\gamma}{2\pi}\int_0^t G_y(\tau)\,d\tau$$

$$2.7$$

The Fourier Transform (FT) makes it possible to decompose complex spatial domain signals from $m(x,y)$ to the frequency domain as $M(k_x,k_y)$ as a function of time. The complex signal detected in quadrature where the RF signal is split into real and imaginary components in the spatial domain called the k-space. Discrete digital MR signals are encoded into k-space by using gradient coordinate systems. The sampling rate of MR signals is based on the principles of digital signal processing (DSP) where sampling must satisfy the Nyquist criteria ($\geq 2f_{max}$). Once the k-space is encoded, MR images are produced using the Inverse FT.

The MR images used in OE-MRI for my investigations were acquired using a set of pulse sequences with unique gradient coordinate systems as illustrated in Figures 2.16-2.20. First, scout images (Figure 2.16) were acquired at the minimum repetition time (TR) and echo time (TE) to initially locate the tumor. Second, an anatomical slice plan was determined for the tumor using a fast spin echo (FSEMS or T_2-weighted images) pulse sequence (Figure 2.17). The MR images that allowed the investigation of responses to inhaling oxygen compared to a baseline of air were T_1-weighted images

and T_2^*-weighted images [37].   The T_1-weighted images for quantitative T_1 measurements used a 2-D multi-slice spin echo (SEMS) pulse sequence as illustrated in Figure 2.18. The other pulse sequences used in my investigations were 2-D multi-slice spoiled gradient-echo (GEMS or T_1-weighted images) and 2-D multi-slice spoiled gradient-echo with multi-echo (MGEMS or T_2^*-weighted images) as shown in Figure 2.19 and Figure 2.20, respectively.
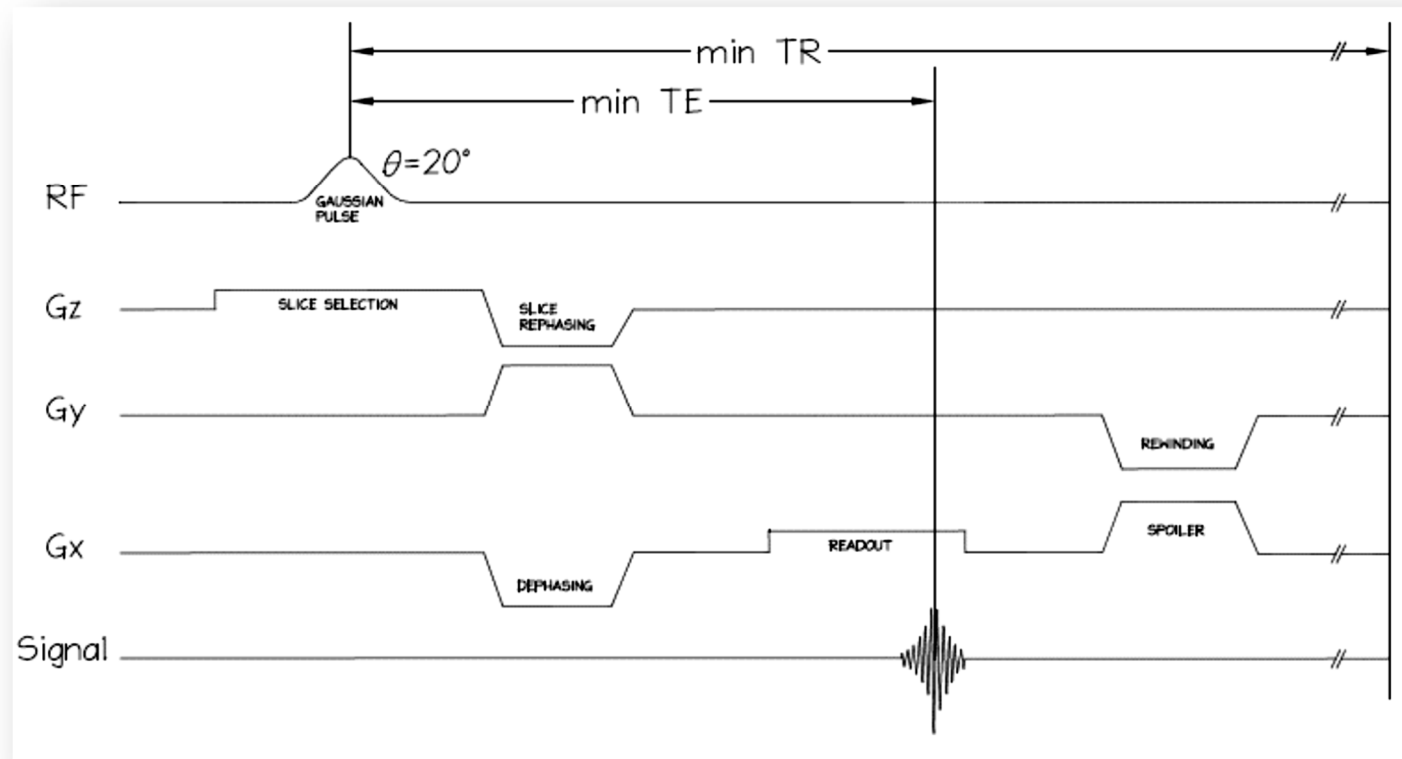
Figure 2.16 Gradient Coordinate System for Scout Images using 4.7T Varian Small Animal Magnet Scanner
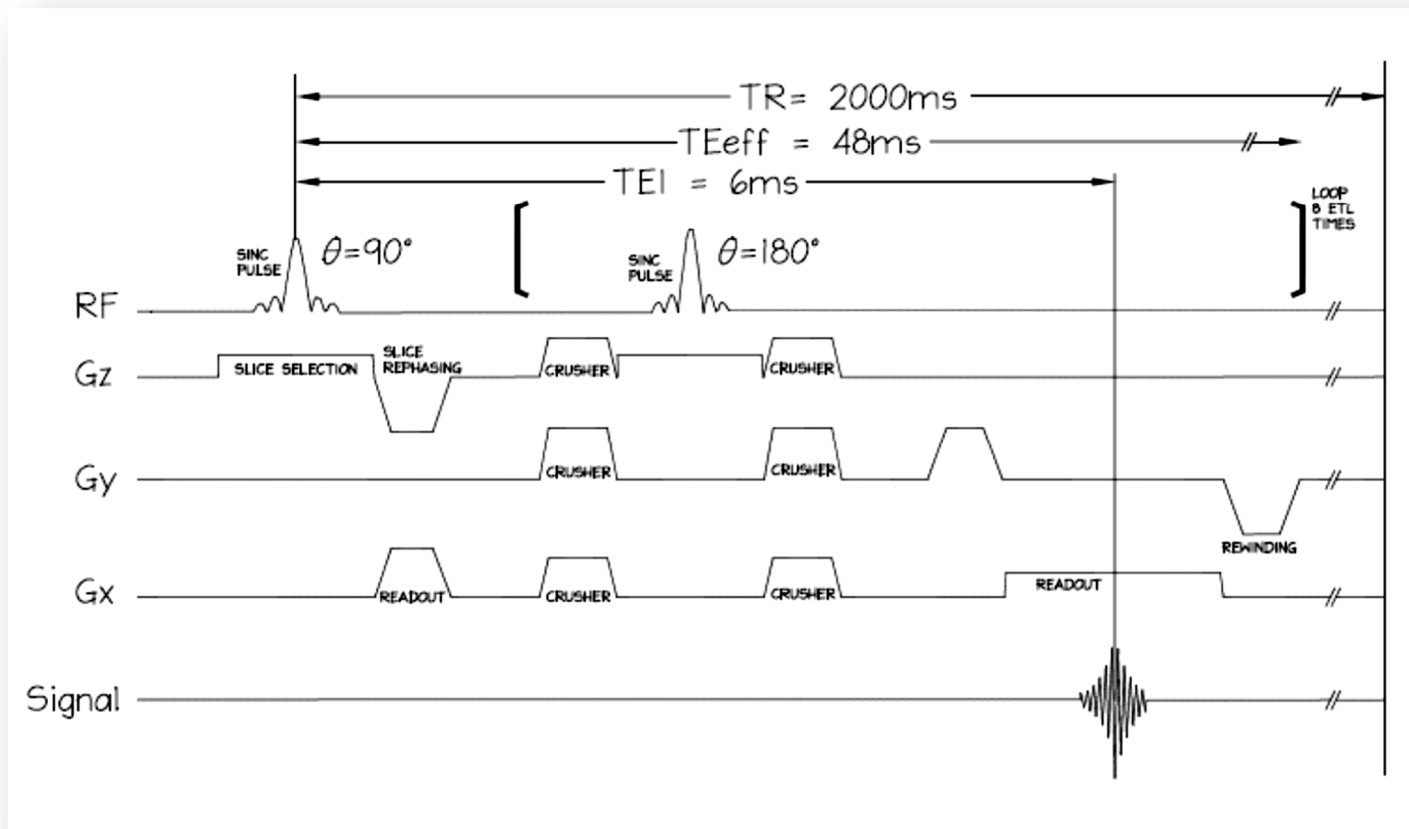
Figure 2.17 Gradient Coordinate System for Anatomical Images using 4.7T Varian Small Animal Magnet Scanner
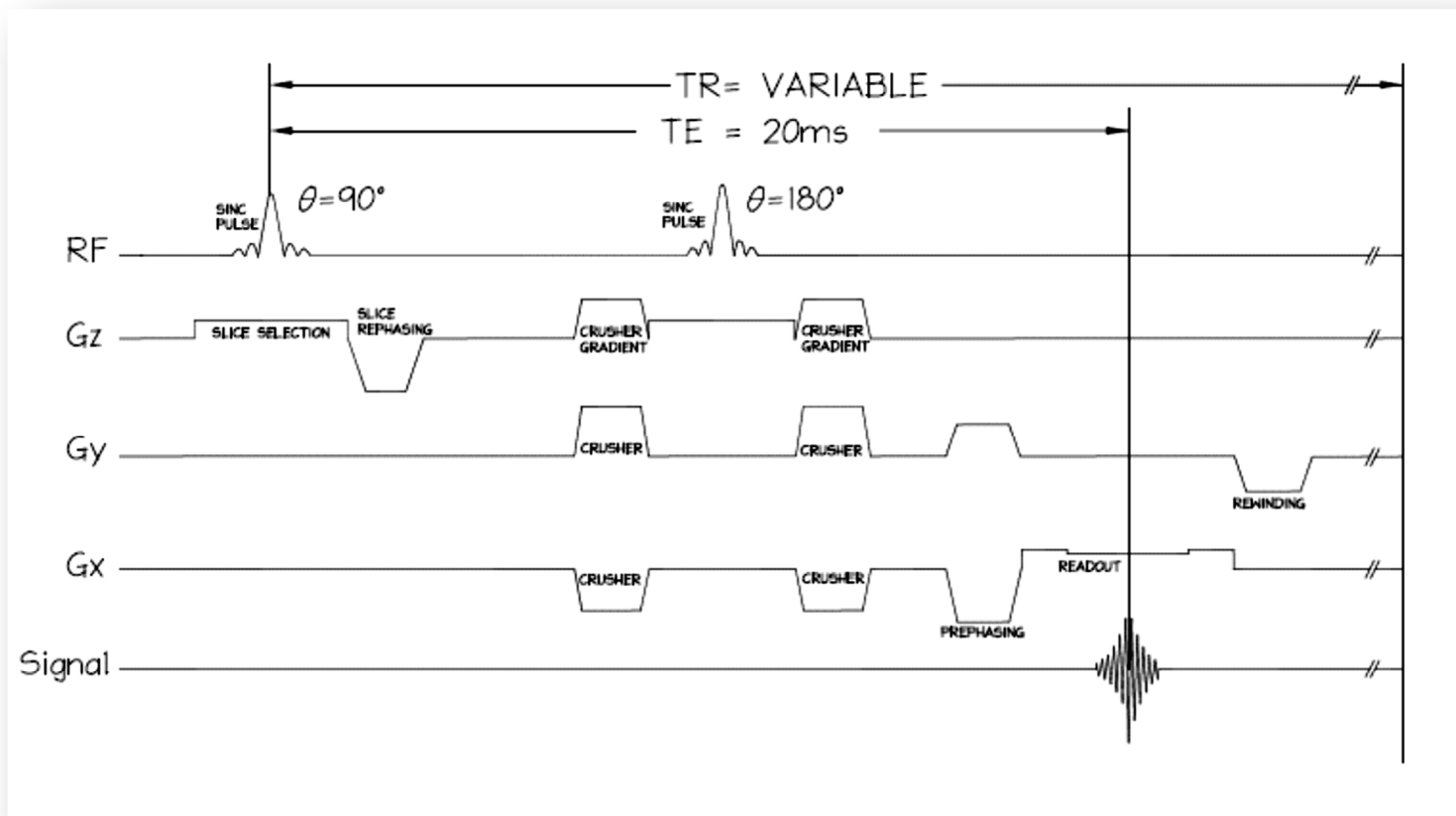
Figure 2.18 Gradient Coordinate System for Quantitative T_1 measurements using 4.7T Varian Small Animal Magnet Scanner
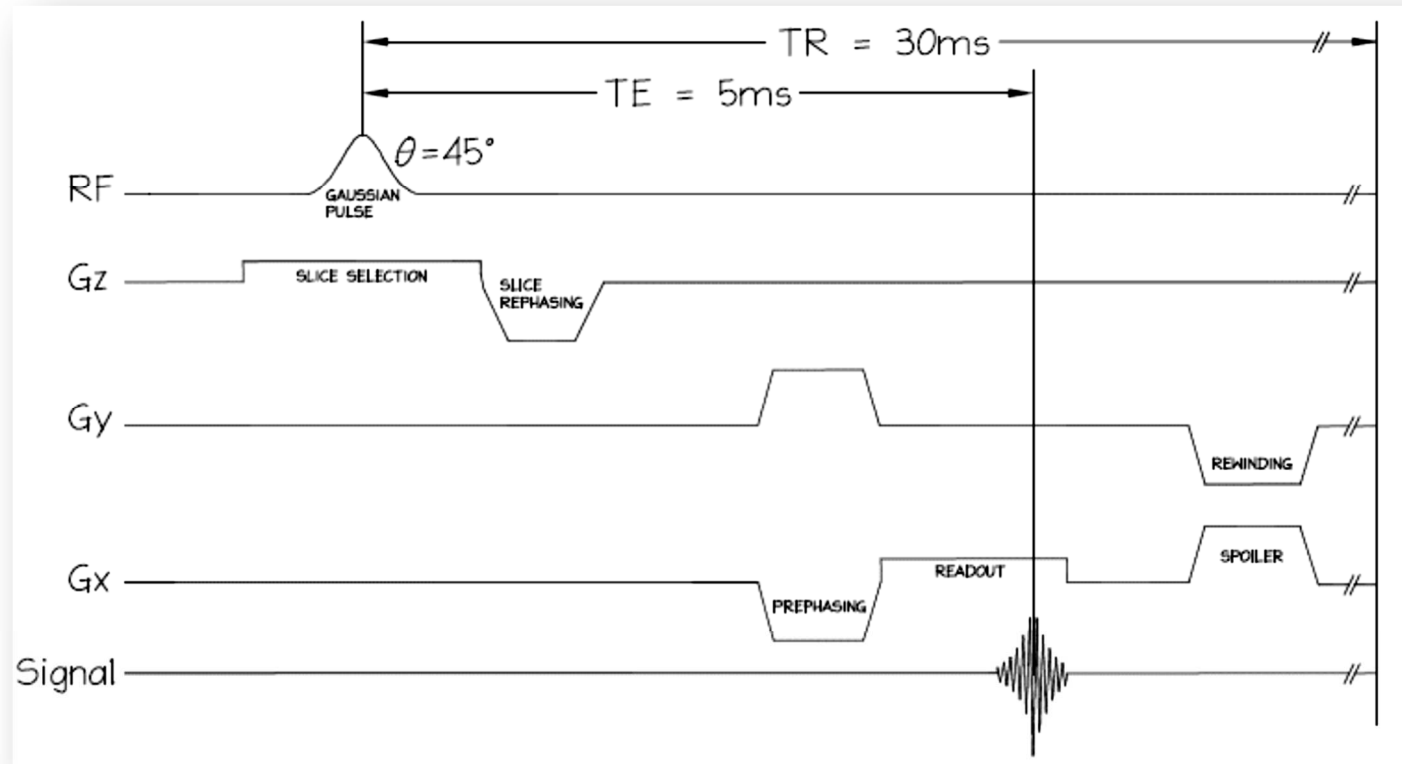
Figure 2.19 Gradient Coordinate System for T_1-weighted Images using 4.7T Varian Small Animal Magnet Scanner
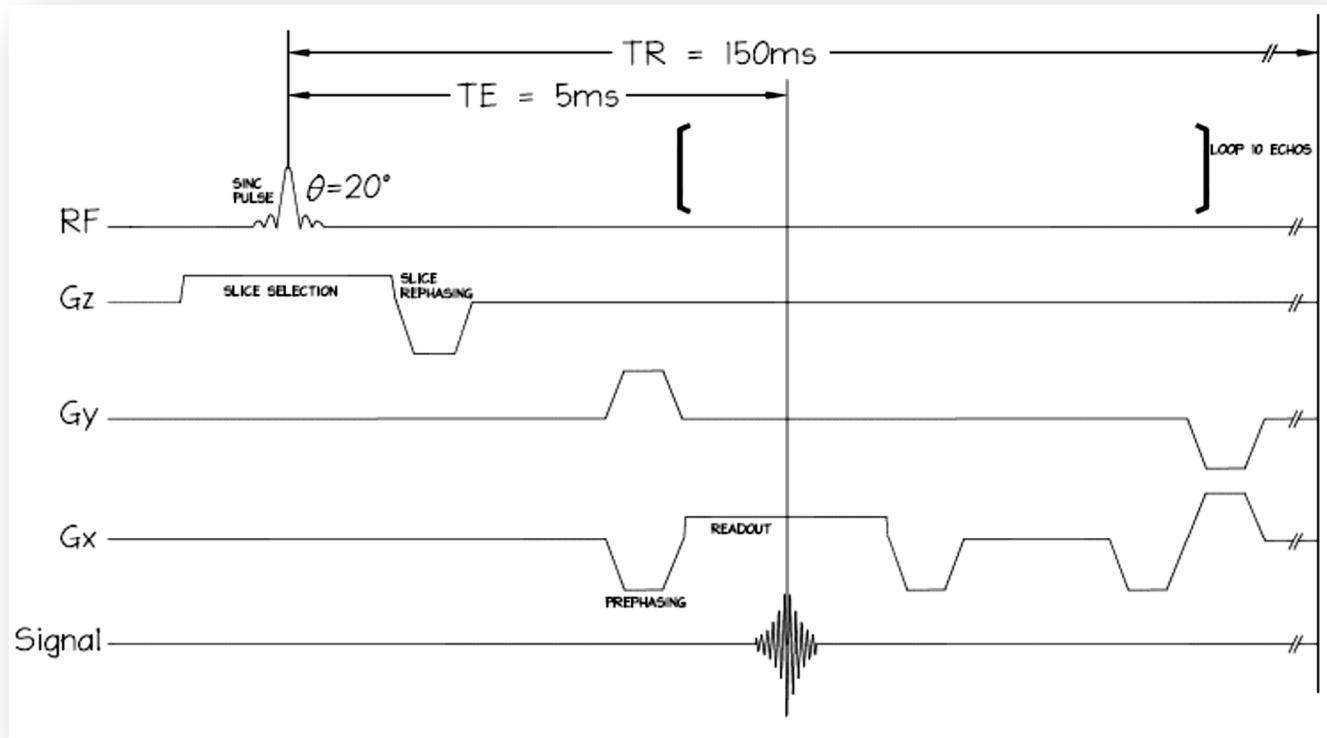
Figure 2.20 Gradient Coordinate System for T_2*-weighted Images using 4.7T Varian Small Animal Magnet Scanner

During OE-MRI, oxygen is used as an endogenous contrast agent. Oxygen is paramagnetic since it has two (2) unpaired electrons (e⁻). Thus, oxygen affects the water protons in tumor tissue by directly altering T_1 relaxation times due to the energy exchange between protons and oxygen unpaired e⁻. If tumor oxygenation increases when inhaling oxygen during MR imaging, the T_1 values decrease ($R_1 = \frac{1}{T_1}$ increases) and hence the MR signal increases relative to baseline air on T_1-weighted images. Similarly, gadolinium is paramagnetic. As shown in Appendix A, T_1 values were altered by gadolinium (seven (7) unpaired e⁻) using a Gadavist phantom. Oxygen also affects water protons indirectly by altering T_2^* relaxation times due to oxygen binding to deoxyhemoglobin. Consequently, T_2^* values increase ($R_2^* = \frac{1}{T_2^*}$ decreases) and the MR signal increases on T_2^*-weighted images.

Previous investigations have shown that the MR relaxation rates (R_1 and R_2^*) in tissues are affected by inhaling oxygen [35,97-99]. The R_1 and R_2^* relaxation rates in tumors can be illustrated where oxygenated tumors will recover faster compared to a baseline of air (Figure 2.22) and will have a longer signal decay compared to air (Figure 2.23), respectively. In addition, MR change in signal intensities on T_1-weighted and T_2^*-weighted images have been previously investigated [37], as illustrated in Figure 2.24. Figure 2.25 illustrates a typical setup used in my investigations for acquiring *in vivo* OE-MRI images. However, the BOLD (T_2^*-weighted images) and TOLD (T_1-weighted images) effects used in OE-MRI are affected by changes in oxygenation but also due to changes in blood flow and blood volume. Howe *et al.* [100,101] showed that the BOLD effect was significantly affected by blood flow and blood volume in GH3 prolactinomas tumors in rats. It was indicated that the ΔR_2^* decreased from blood volume reduction rather than by improved oxygenation and a correlation of ΔR_2^* with increase oxygenation

may be nonlinear. On the contrary, Howe *et al.* [102] found that when rats breathed 100% N_2 there were decreases in R_2^* ($1/T_2^*$) matching when breathing 100% oxygen in MNU tumors but to a lesser degree in GH3 tumors having regions of both increased and decreased R_2^* while breathing 100% N_2. They concluded that this was attributed to a decrease in blood pressure following death resulting in vascular collapse and thus, reduced blood volume. Jordon *et al.* [103] used oxygen consumption inhibitors (insulin and NS-398) to investigate the BOLD effect in murine FSaII tumors implanted in mice. They found that the BOLD signal decreased with infusion of the inhibitors and the ΔR_2^* remained the same while the tumor pO_2 increased when using EPR oximetry.
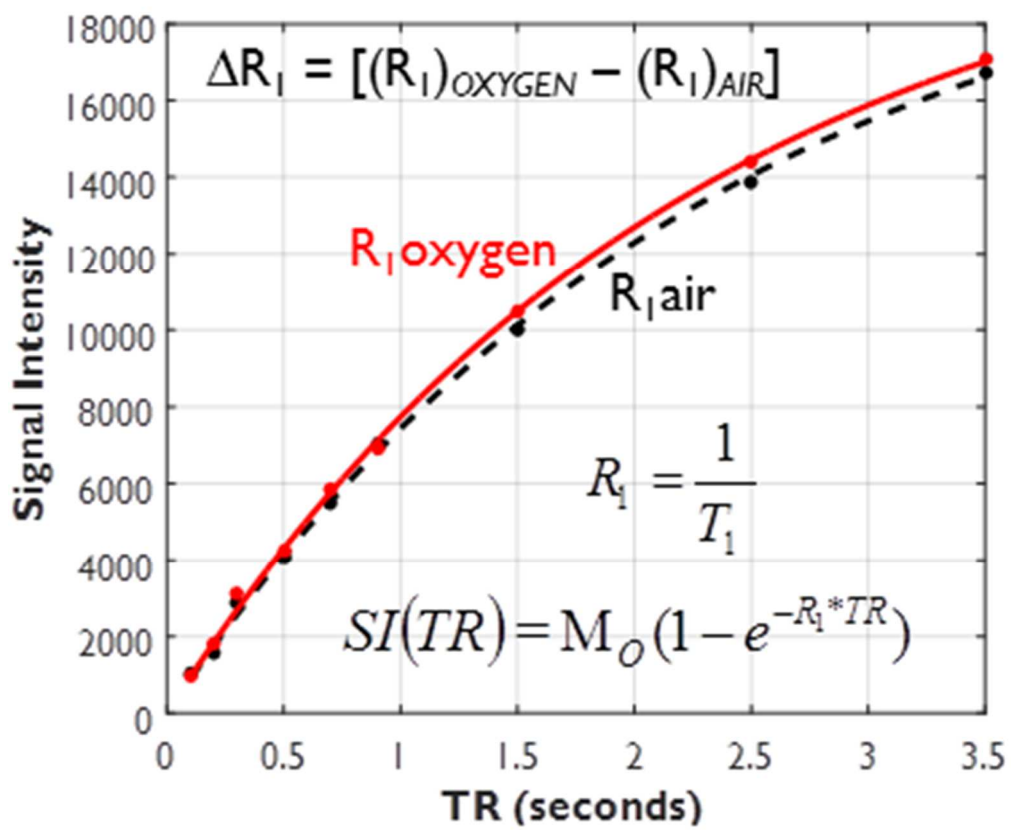
Figure 2.21 General representation of R_1 relaxation signal recovery curves when inhaling

air (black curve) or oxygen (red curve)
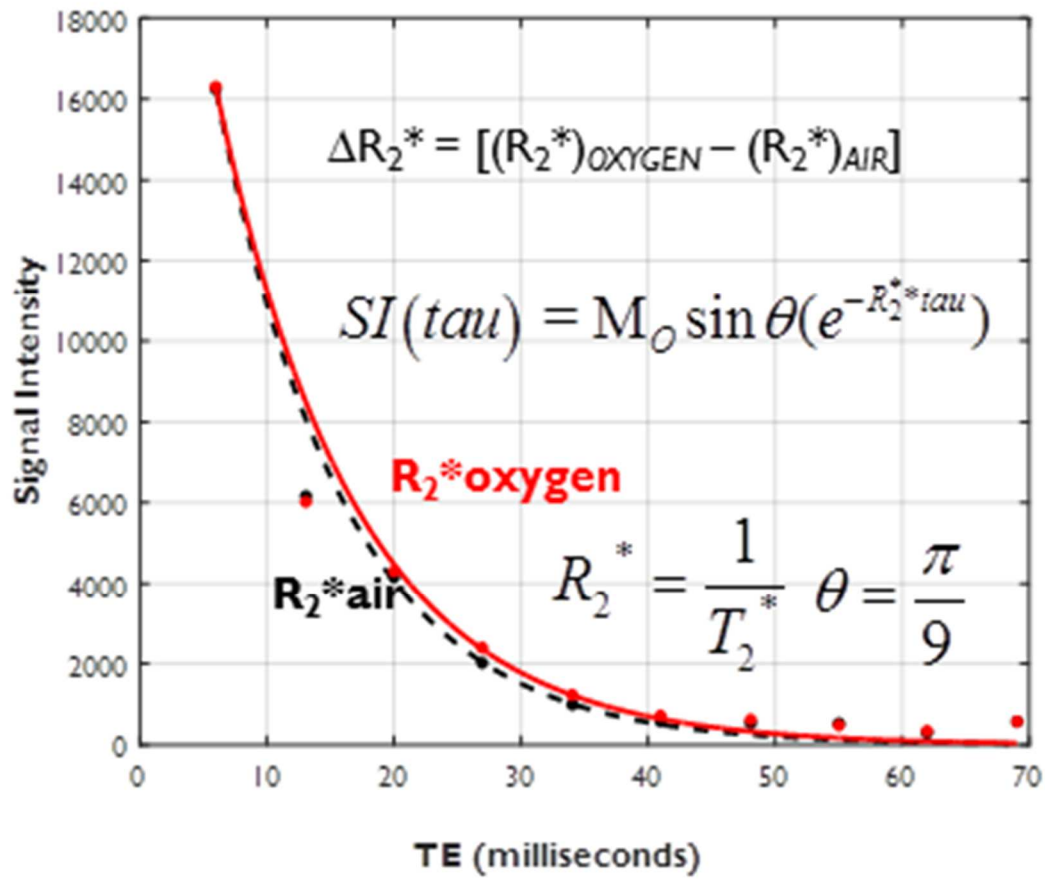
Figure 2.22 General representation of $R_2{}^*$ relaxation signal decay curves when inhaling

air (black curve) or oxygen (red curve)
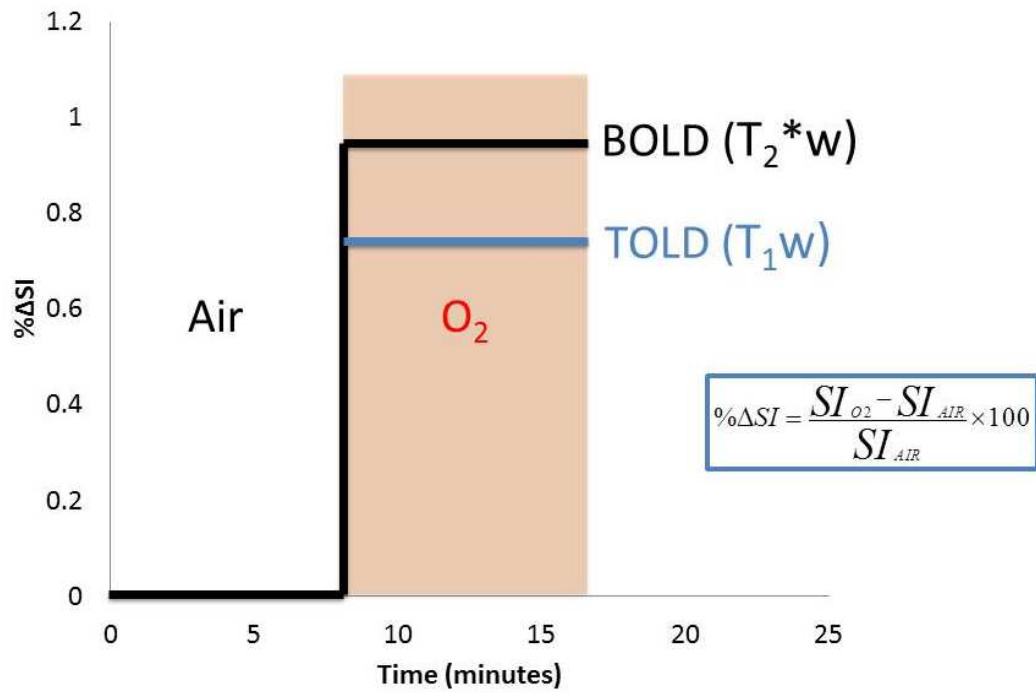
Figure 2.23 General representation of an interleaved dynamic acquisition of T_1 (blue line) and T_2^* (black line) weighted images when inhaling air or oxygen.

Gas valves and gage

4-8 mm diameter lead free plastic vinyl and appurtenances

Small animal isoflurane and gas flow machine

Acquisition System

Small animal magnet (horizontal bore)
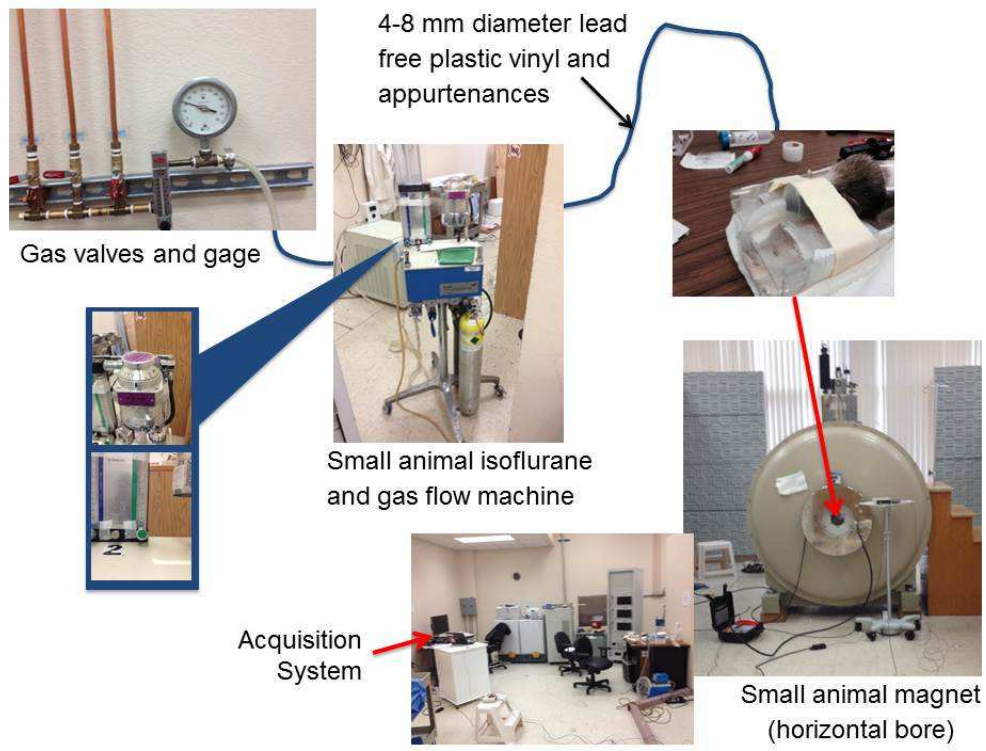
Figure 2.24 Photo of *in vivo* OE-MRI setup using the 4.7 T small animal MRI system

Small Animal Irradiator

A kilovoltage (superficial and orthovoltage) image-guided small animal irradiator (225kV) was used for all my tumor radiobiological investigations. The main component of a kilovoltage radiotherapy x-ray machine is the x-ray tube (Figure 2.4). The quality of an orthovoltage x-ray beam produced from an x-ray tube is determined by measuring the half-value layer (HVL) which is usually given in millimeter (mm) of copper (Cu). The HVL is the thickness of material that reduces the x-ray beam intensity to 50% of initial value [60]. The depth dose distribution in tissue is quantified by the percent depth dose (PDD) where the PDD is close to 100% at the surface of the tissue [60]. The main dose parameters involved in the delivery of external x-ray or photon beams from an kilovoltage unit are the depth of treatment, field size, the source-surface distance (SSD) or source-axis distance (SAD), photon beam energy, the number of beams used in dose delivery to the subject, and the treatment time [60]. The American Association of Physicists in Medicine (AAPM) developed a protocol (AAPM Report 76) for kilovoltage range units used for dosimetry measurements of x-rays in radiotherapy and radiobiology investigations. Figure 2.26 illustrates a typical setup used in my investigations implementing radiotherapy to the prostate tumors.

XRAD 225Cx Small Animal x-ray Irradiator

Superficial X-Rays
(4kV, 0.3mA)

Orthovoltage X-Rays
(225kV, 13mA)

AP   PA

Representative SQ AT1 prostate tumor
localized using x-ray before irradiation with
1F x 7.5 Gy AP/PA
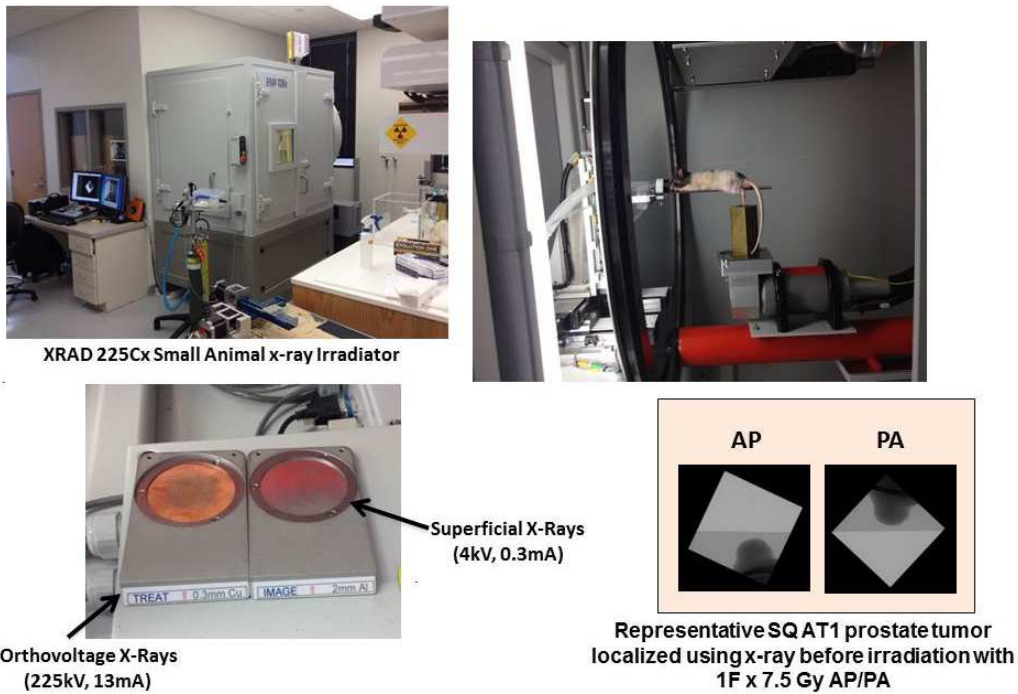
Figure 2.25 Photo of a radiotherapy setup using the XRAD 225Cx small animal x-ray
irradiator

In chapters 5 and 6, I evaluated the usefulness of OE-MRI measurements in small to large volume AT1 prostate tumors using a single- or spilt-dose of 30 Gy. Using image-guided radiotherapy, the gross tumor volume (GTV) was localized using superficial x-rays with 2 mm Al added filter (energy: 40 kV; current: 0.3 mA). The irradiation of tumors used orthovoltage x-rays at 1F x 15 Gy AP/PA or 2F x 7.5 Gy AP/PA with 0.3 mm Cu added filter (energy: 225kV; current: 13 mA). The dose rates varied with square field sizes (20 – 40 mm). Tumor growth measurements were recorded over time (approximately weekly) to assess the response to radiation. The pre-irradiation OE-MRI parameters were compared to the tumor growth delay (TGD) measured up to 40 days or

until tumors reached 2-4 times the irradiated tumor volume. An illustration of tumors responding to split-dose irradiation while inhaling oxygen compared to air is shown in Figure 2.27.
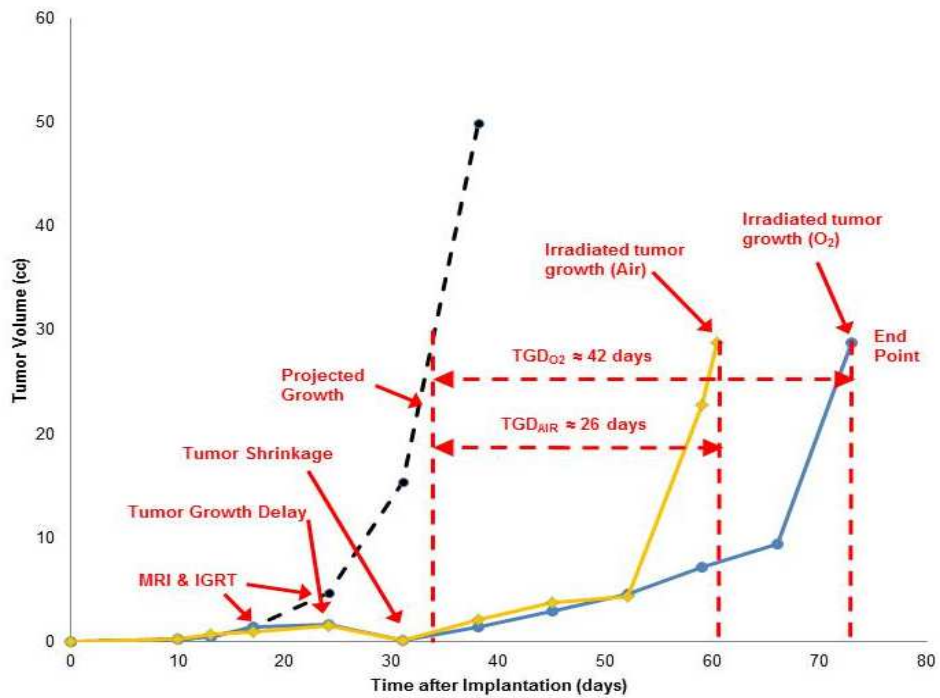
Figure 2.26 Illustration of Tumor Irradiation Response to inhaling air or oxygen

Chapter 3

Human PC3 Prostate Cancer Cells Transfected with Luciferase: A Limited In Vivo Bioluminescence Imaging Application in Nude Rat Tumor Models

Abstract

Introduction

Early detection is effective in the war against prostate cancer. Consequently, in pre-clinical cancer studies with or without intervention, *in vivo* bioluminescence imaging has been used as a non-invasive screening tool in regards to the growth of proliferating cancer cells in their early stages. Success in using luciferase transfected cancer cells has been notable in different tumor models [104-108]. However, I discovered that this was not the case in PC3 human xenografts implanted in adult male nude rats.

Purpose

To monitor the growth of subcutaneous and orthotopic PC3 prostate tumors in adult male nude rats.

Material and Methods

Human prostate cancer cell line PC3 (the American Type Culture Collection, Manassas, VA) were transfected with luc gene (PC3-luc) by Dr. Li Liu (UTSW Assistant Professor, Radiology). PC3-luc were implanted in adult male nude rats subcutaneously (n = 3) or orthotopically (n = 9) by Mason Lab technical support. *In vivo* bioluminescence imaging (BLI), high frequency ultrasound imaging (US), or mechanical calipers monitored the growth of the implanted tumors.

Results

No *in vivo* BLI signal was observed in Group 1 (n = 6), implanted without Matrigel™, even though ultrasound (US) or magnetic resonance (MR) images indicated the presence of

growing tumors. Group 2 (n = 6), implanted with Matrigel™, changes in the *in vivo* BLI signal intensity were observed but signals decreased with time for both subcutaneous and orthotopic tumors despite evidence of tumors, based on US or MR imaging.

Conclusions

This study indicates that *in vivo* bioluminescence imaging, although an excellent monitoring tool for detecting sub-palpable volumes in small animal studies involving mice, must be used cautiously when monitoring the growth of PC3-luc cells in adult nude rats.

Introduction

In vivo BLI has the capability to provide cell and molecular biological observations practically within any tissue type just by detection of the distribution of photons emitted once the substrate (luciferin) is catalyzed by the firefly enzyme (luciferase), if the tissue cells are transfected biochemically with luciferase. Metabolic active cancer cells require the presence of adenosine triphosphate (ATP) and oxygen (O_2) for energy and oxidation, respectively [106,109-112]. With the increase level of specificity and decrease in the level of background noise compared to other optical imaging techniques such as fluorescence, *in vivo* BLI is still subject to tissue scattering which is a major issue for optical imaging [113]. Up to five (5) small animals such as mice can be imaged at the same time allowing data sets to be collected per group. However, imaging more than one larger animal such as a rat at a time is more of a challenge due to the possible limitations with the field-of-view and available space in the imaging chamber.

In vivo BLI is a user-friendly biomedical imaging modality for observing the growth of tumors or response to interventions such as chemo- or radiotherapy, and acute response to vascular disruption agents in small animal studies [107,108,110,112,114-

120]. In fact, the vascular shutdown of tumors has been observed non-invasively using *in vivo* BLI with vascular disruption agents [114]. In addition, the irradiation of small sub-palpable tumor tissue volumes has been investigated using the distribution of *in vivo* BLI signals for off-line image guidance to enhance tumor target accuracy [121]. Using *in vivo* BLI to monitor the growth of proliferating cancer cells in their early stages has been a major impact on previous studies. BLI can provide speedy results. It has the sensitivity for detecting non-palpable tumor volumes and affordable while providing robust observations.

Longitudinal pre-clinical cancer studies with or without intervention has been notable with different tumor models expressing luciferase [104-108]. Also, investigators have demonstrated correlations of early proliferating cancer cells growth with the increase in the *in vivo* BLI signal intensity [104-108]. However, I have discovered that this is not the case in PC3-luc human xenografts implanted in adult male nude rats. In this study, I present experimental data that showed *in vivo* BLI signal does not always correlate with the growth of tumors. I identify potential causes for observed decreases in BLI signals and recommend opportunities to pursue additional investigations for finding solutions to this problem.

Methods and Materials

Ethical Statement

All investigations were implemented after the review and approval by the UT Southwestern Institutional Animal Care and Use Committee in accordance with Federal, State, and Local laws and guidelines.

48

Animals and Experimental Tumor Models

Twelve (12) adult male nude rats (strain model CR: NIH-RNU weighing approximately 287-300 g and six (6) weeks old) were obtained from the National Cancer Institute (NCI, Frederick, MD) and housed in a specific pathogen free facility of three (3) rats per cage. Rats were divided into two (2) groups. The two (2) groups are represented as Group 1 (*n* = 6), orthotopic prostate tumors implanted without Matrigel™, and Group 2 (*n* = 6), subcutaneous or orthotopic prostate tumors implanted with Matrigel™ [122]. Approximately 2.5 x 10^6 PC3-luc human prostate cancer cells [114,123], cultured at 37°C in a 5% CO_2 humidified incubator, were implanted subcutaneously in the right flank [114] or orthotopically into the actual prostate to generate tumors for experimental studies as previously described [124].

In vivo Bioluminescence Imaging

In vivo bioluminescence imaging (BLI) was performed within 2-7 days after implantation. Typically, the animals were anesthetized with 3.0-4.0% isoflurane/oxygen for induction followed by 1.5-2.0% isoflurane/oxygen for maintenance (oxygen flow = 1 L/min). Approximately 500 µl of fresh *D*-luciferin (150 mg/kg in saline, sodium salt, Gold Biotechnology, St Louis, MO) was administered subcutaneously in the fore back neck region using an insulin syringe, as previously described [114,115]. Eye lubricating ointment was applied to the eyes to prevent drying. Using an IVIS® Luminia Imaging System (Caliper Life Sciences, Hopkinton, MA), *in vivo* BLI images were acquired ten (10) minutes post-injection of *D*-luciferin for 3 minutes exposure time, binning = 8, and f/stop = 1. *In vivo* BLI was periodically performed (weekly) until the evolution of an appropriate tumor volume (determined by mechanical calipers or ultrasound imaging).

Ultrasound Volume Measurements on Experimental Tumor Models

Each nude rat was anesthetized and placed on a temperature-controlled platform to keep the animal warm. For the subcutaneous PC3-luc prostate tumors (PC3-luc-SQ), ultrasound imaging (US) was implemented using a VisualSonics Vevo 770 High-Resolution Imaging System (Visual Sonics Inc, Toronto, Ontario, Canada) to correlate the growth of the PC3-luc-SQ with BLI or mechanical caliper measurements. An ultrasound transducer with a 17.5 MHz or 40 MHz probe in B-mode was used to image the tumor region with imaging gel for coupling. All PC3-luc-SQ tumor volumes were calculated using US or mechanical caliper as previously described [114,125-127].

Magnetic Resonance Imaging on Experimental Tumor Models

During the MR imaging experiments using a Varian 4.7T small animal scanner, the anesthetized (typical) animals were provided with a circulating warming pad to maintain body temperature at approximately 37°C. To achieve a MR signal at optimum conditions, the radiofrequency (RF) body and/or volume coil was tuned to proton (^{1}H) resonance frequency (200 MHz) and matched to the characteristic impedance of the coil to approximately 50 Ohm. The magnetic field in the MR scanner underwent a manual shimming process to improve the homogeneity of the magnetic field in the region of interest.   This maximized the MR signal during the MR imaging experiment. After shimming the magnetic field, scout images (axial, coronal, and sagittal images) were acquired by using a fast spin echo sequence or a gradient echo sequence. These images were used to plan for acquiring anatomical images. Anatomical images or T_2-weighted images (TR/TEeff = 2000/48 ms, ETL = 8, NEX = 8, Matrix = 128 x 128, FOV = 60 mm x 60 mm, Slices = 20, Slice Thickness = 2mm, Scan Time = 4 min 16 sec) were acquired.

Ex vivo Bioluminescence Imaging

An e*x vivo* bioluminescence imaging (BLI) experiment was implemented on one (1) excised orthotopic prostate tumor bearing nude rat. The excised orthotopic prostate tumor was fragmented into pieces. BLI images were acquired after adding *D*-luciferin dropwise onto tissue pieces.

Data Analysis on Experimental Tumor Models

Tumor regions of interest (ROI) were selected in the vicinity of the greatest BLI signal intensity in each experimental tumor. Using the manufacturer's software (Living Image 4.2) provided with the IVIS® Lumina Imaging System, the total photon flux (ϕ = Photon / (Image Acquisition Time x Area)) was determined as a function of time after tumor implantation [114]. Tumor volumes for each experimental tumor model were calculated as recommended [114,125-127] and compared with the BLI signal intensity.

Statistical Methods on Experimental Tumor Models

A Spearman rank correlation model was used to determine the correlation between caliper or US tumor volume measurements with the change in BLI signal intensity as function of time after tumor implantation for all PC3-luc-SQ tumors and for all PC3-luc orthotopic prostate tumors (PC3-luc-ORTHO). Mann-Whitney U tests were used to compare statistical differences between the tumor measurement types (BLI, US, or caliper). A Student's t-test was used for comparison of BLI signal intensities as a function of time for tumors implanted subcutaneously or orthotopically. *P*-values less than 0.05 were deemed statistically significant. All analyses were done using Microsoft Excel 2007 or Matlab Statistical Toolbox R2013b.

Results

Growth of Experimental Prostate Tumors

The growth of the experimental prostate tumors was investigated using BLI for a period of approximately 14 days for Group 1 (n = 6) (Figure 3.1a) and up to 37 days for Group 2 (n = 6) (Figures 3.1b and 3.1c). Figure 3.1a illustrates that at day 14 Group 1 (n = 6) showed no signs of the *in vivo* BLI signal orthotopically. Within three (3) to nine (9) days, the detection of an *in vivo* BLI signal in Group 2 (n = 6) was observed in both subcutaneous (n = 3) and orthotopic (n = 3) tumors as illustrated in Figure 3.1b and Figure 3.1c, respectively. For Group 2, Figure 3.2. illustrates the change in the *in vivo* BLI signal as a function of time after tumor implantation for both experimental tumor models. *In vivo* BLI signal intensity changes over time for subcutaneous prostate tumors and orthotopic prostate tumors in Group 2 demonstrated no significant (P > 0.50) difference between the two experimental tumor models.

Since the growth of tumors in mice or rats has been found to coincide with the change in BLI signal intensity over time, I tested the hypothesis if tumor volume measurements calculated using a mechanical caliper or US imaging can be compared with *in vivo* BLI results. My observations on Group 1 (n = 6) showed no *in vivo* BLI signal as previously mentioned in the orthotopic prostate tumors. However, physical examination in the vicinity of the prostate or bladder indicated the evolution of solid mass in one (1) nude rat. On the same day after *in vivo* BLI, an US image revealed an orthotopic prostate tumor of approximately 1.56 cm^3.
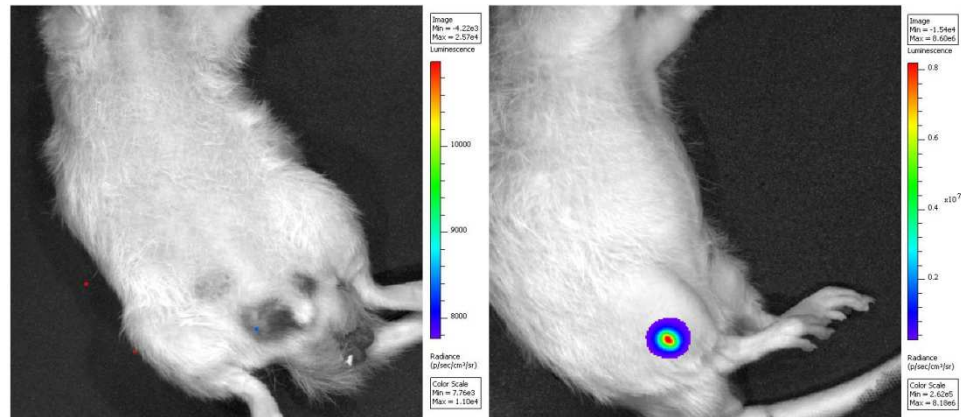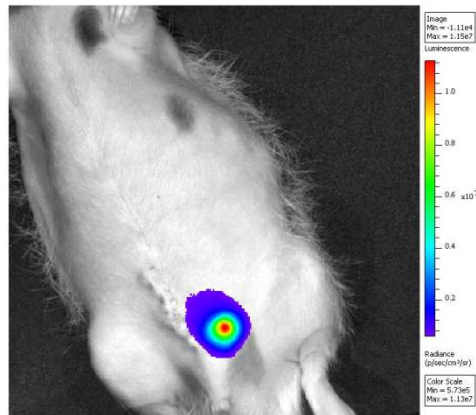
Figure 3.1 a-c - Examination of PC3-luc prostate tumors (Group 2) in a representative adult male nude rat using *in vivo* bioluminescence imaging. No detection, orthotopically, of *in vivo* BLI signal collected for 3 minutes exposure time, binning = 8, and f/stop = 1 at day 14 after tumor implantation. Detection of an *in vivo* BLI signal in (b) subcutaneously (exposure time = 3 min, binning = 4, and f/stop = 1) and (c) orthotopically (exposure time = 3 min, binning = 4, and f/stop = 1) at day 9 after tumor implantation.
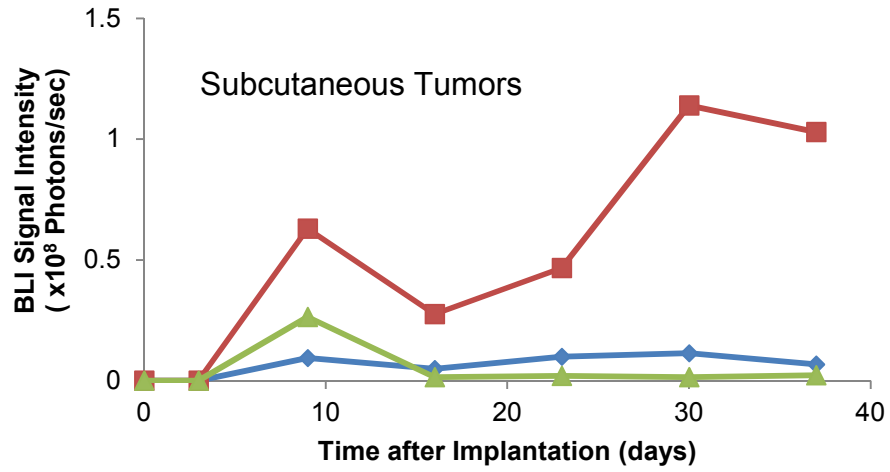
(a)
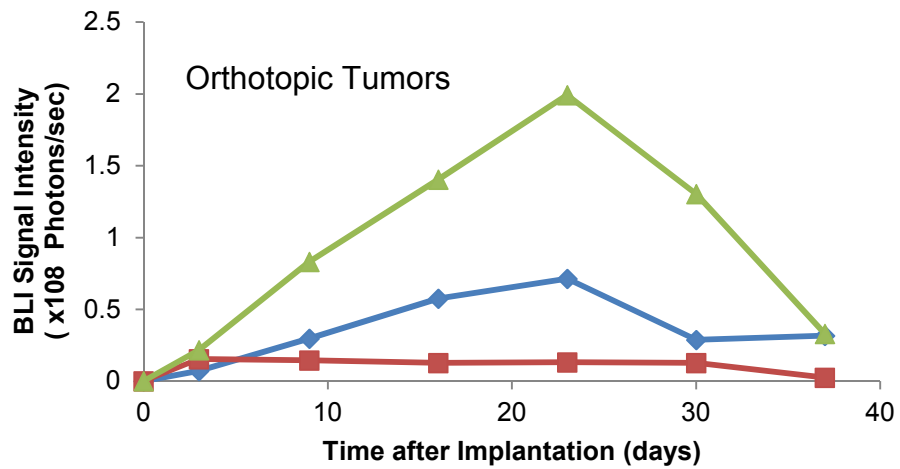
(b)

Figure 3.2 *In vivo* bioluminescence imaging intensity at 3 minutes exposure time after tumor implantation for two (2) experimental models (Group 2). (a) Subcutaneous PC3-luc prostate tumors (PC3-luc-SQ) (*n* = 3). (b) Orthotopic PC-3-luc prostate tumors (PC3-luc-ORTHO) (*n* = 3).

To minimize experimental cost and since no *in vivo* BLI signal was observed in Group 1, only US imaging was continued up to approximately twenty-three (23) days for monitoring the growth of the orthotopic prostate tumor bearing in the nude rats. US imaging detected solid tumors in all animals bearing PC3-luc cancer cells from Group 1. Group 2 (n = 6) subcutaneous prostate tumors (n = 3) grew monoexponentially (Figure 3.3) based on the results of caliper ($P < 0.00004$) or US ($P = 0.00149$) tumor volume measurements compared to the results of the change in the *in vivo* BLI signal intensity, respectively. Consequently, *in vivo* BLI signal intensity changes over time showed that there was a significant difference between mechanical caliper and US tumor volume measurements in subcutaneous PC3-luc prostate tumors (PC3-luc-SQ) implanted in adult male nude rats. In regards to PC3-luc-SQ, one (1) animal died, the second (2nd) animal died during a magnetic resonance (MR) imaging experimental study, and the third (3rd) animal survived all experimental studies. For orthotopic prostate tumors (n = 3) in Group 2, no solid tumors were observed by US imaging ($P < 0.001$) even though a change in *in vivo* BLI signal intensity was seen. Consequently, *in vivo* BLI signal intensity change over time showed that there was a significant difference between US tumor volume measurements in orthotopic PC3-luc prostate tumors (PC3-luc-ORTHO) implanted in adult male nude rats. The Group 2 PC3-luc-ORTHO animals remained alive and later used for training technical staff before sacrifice.

I have observed the growth of orthotopic tumors in adult male nude rats with US imaging, MR imaging, or by palpable examinations. Oddly, Group 1 showed no *in vivo* BLI signal. After the extraction of an excised-fragmented orthotopic prostate tumor, *ex vivo* BLI images of this orthotopic prostate tumor were acquired at different exposure times (Figure 3.4) illustrating no *ex vivo* BLI signal.
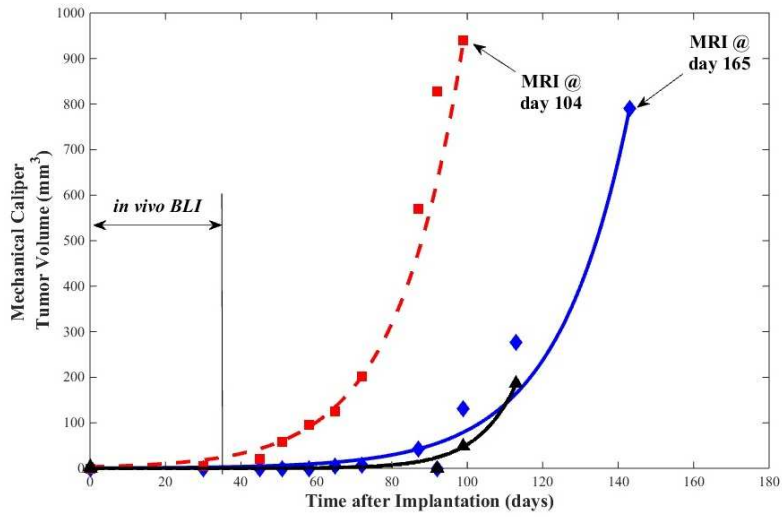
(a)
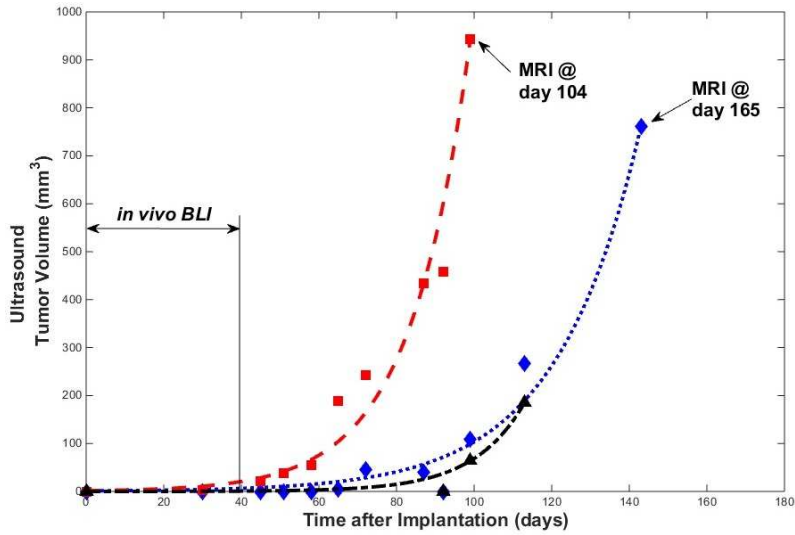
(b)

Figure 3.3   Subcutaneous prostate tumor measurements after tumor implantation. Observations of monoexponential growth of subcutaneous prostate tumors (n = 3) based on the results of (a) caliper (P < 0.00004) or (b) US (P = 0.00149) tumor volume measurements compared to the results of the change in the *in vivo* BLI signal intensity, respectively

56

However, US images (Figure 3.5a) acquired previous to the *ex vivo* BLI clearly showed the presence of a solid tumor mass. Figure 3.5b is another US image of a different adult male nude rat with an orthotopic tumor but no *in vivo* BLI signal.

Figure 3.4 Excision of the orthotopic prostate tumor and images after injection of *D*-Luciferin. Results show no BLI signal even after tumor excision.
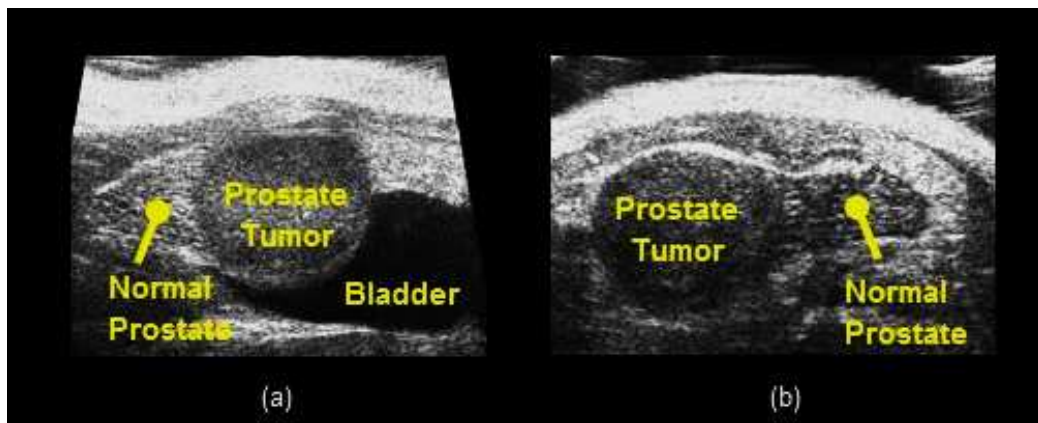
Figure 3.5 Ultrasound (B-mode, 17.5 MHz probe) images of representative adult male nude rats with (a) tumor applying compression on the bladder (results before excision) and (b) tumor growing within normal prostate tissue.

Correlation of BLI with US and Mechanical Caliper Measurements

Approximate estimates of tumor volumes were possible in animals bearing prostate tumors using US imaging or a mechanical caliper. The subcutaneous (n = 3) experimental prostate tumor model in Group 2 showed similar behavior (R^2 > 0.93) based on scattered plot of US or MR and mechanical caliper tumor volume measurements shown in Figure 3.6. However, the change in BLI signal intensity over time after tumor implantation did not correlate with mechanical caliper (P > 0.50) or US imaging (P > 0.50) tumor volume measurements based on a Spearman rank correlation analysis for subcutaneous or orthotopic prostate tumors, respectively.
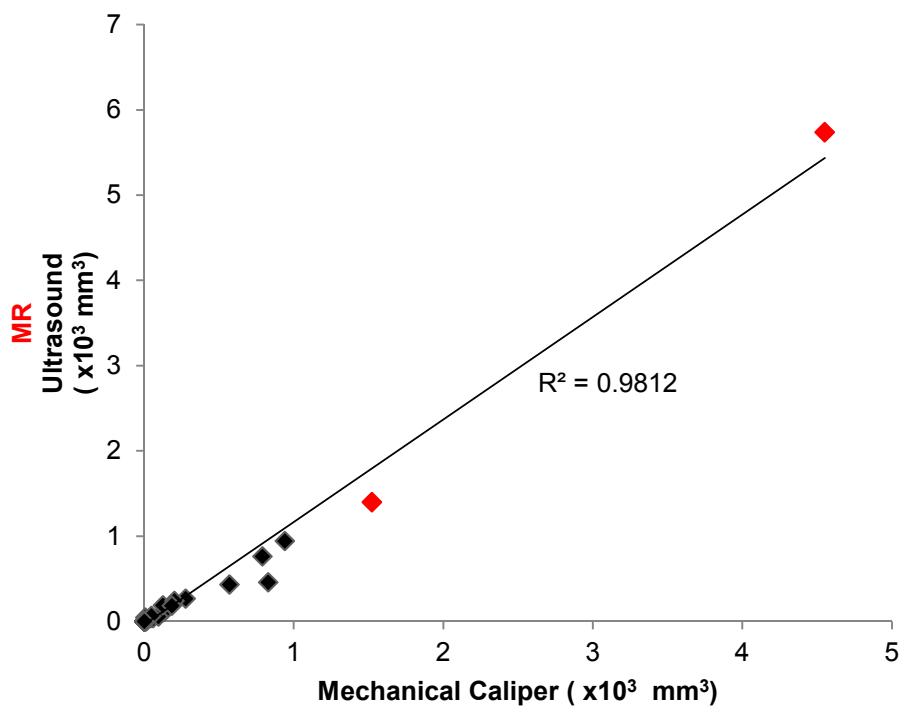
Figure 3.6 Correlation of caliper measurements with MR (♦) and ultrasound (♦) imaging measurements from all PC3-luc-SQ prostate tumors

Discussion

Pre-clinical cancer studies with or without intervention have suggested that *in vivo* bioluminescence imaging (BLI) used to monitor the growth of different tumor models expressing luciferase demonstrated a correlation of the growth of proliferating cancer cells with the increase in the *in vivo* BLI signal intensity [114]. Notably, the correlation between *in vivo* BLI and tumor volume based on mechanical caliper, ultrasound (US) imaging, or magnetic resonance (MR) imaging measurements have been reported [114,120,128,129] in mice. Sub-palpable metabolic activity of cancer cells can be screened over time and the quantification of their photon emission magnitude can be tracked which makes *in vivo* BLI a simple yet sophisticated technique for pre-clinical cancer studies. Others have shown effective *in vivo* BLI in PC3-luc cancer cells growing in nude or SCID mice with tight correlations with ultrasound in the subcutaneous location [114]. Moreover, strong correlations were reported between *in vivo* BLI and power Doppler ultrasound imaging in response to vascular disrupting agents [114]. Consequently, I proposed to use *in vivo* BLI in screening experimental tumor models for pre-clinical cancer studies.

I recognized that monitoring the growth of orthotopic prostate tumors in adult male nude rats using *in vivo* BLI is feasible. However, not all orthotopic prostate tumors in my nude rats experienced the evolution of an *in vivo* BLI signal or growth of a solid tumor (take-rate - 3 out of 9 animals). Strangely, the first attempt (Group 1) in all adult male nude rats implanted with orthotopic PC3-luc prostate tumors (PC3-luc-ORTHO) showed no *in vivo* BLI signal, yet ultimately ultrasound (US) or magnetic resonance (MR) imaging (Figure 3.5 and 3.7) both revealed orthotopic tumors (take-rate - 6 out of 6 animals). Notably, these experimental tumor models represented the first observations of human tumor orthotopic PC3-luc xenografts in rats imaged by US or MR imaging in Dr.

59

Mason's lab. It is also important to note that Dr. Mason's lab has successfully observed orthotopic A549-luc and H460-luc lung tumors in nude rats. The notable success can be contributed based on the fact that these lung cancer cells were transfected with a lentivirus vector which typically exhibit reliable and stable gene expression [130].
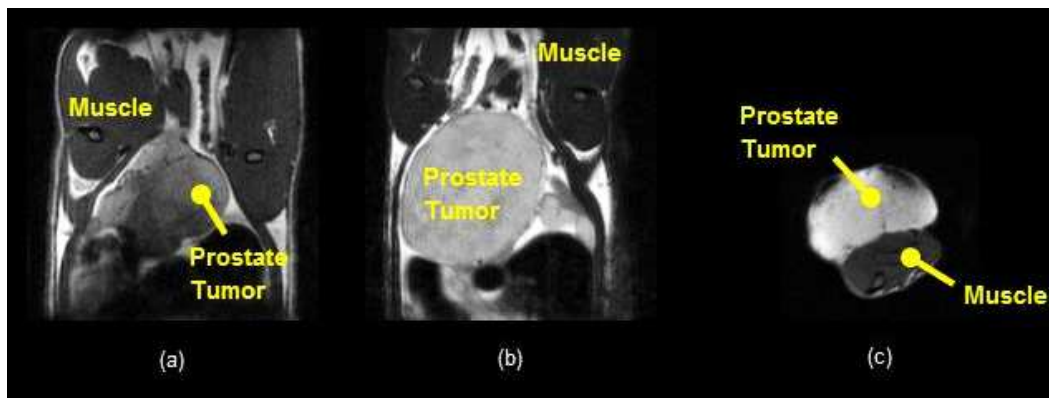
Figure 3.7   Anatomical (T2-weighted) images obtained from representative adult male nude rats with prostate tumors. (a) - (b) Detection of PC3-luc-ORTHO prostate tumors (coronal). Non-invasive MR images acquired after no BLI signal detected in Group 1. (c) Detection of a PC3-luc-SQ prostate tumor (sagittal).

In regards to Group 2, during the sub-palpable growth of proliferating cancer cells in their early stage, *in vivo* BLI signals (take-rate - 6 out of 6 animals) were observed, opposed to Group 1 *in vivo* BLI results, where at the same time US imaging was not able to reveal the growth of a solid tumor. Approximately a month later, only half of the animals (take-rate - 3 out of 6 animals) in Group 2, subcutaneous PC3-luc prostate tumors (PC3-luc-SQ), showed positive signs of solid tumor growth as illustrated by US or MR images (Figure 3.7) yet their *in vivo* BLI signal intensities started to decline a month before. However, it is important to note that although *in vivo* BLI has advantages for

screening the proliferation of cancer cells in their early stages, in regards to my longitudinal prostate cancer studies in groups of rats, it can be very costly ($30 per rat). For example, the amount of luciferin injections required for each rat with an average body weight of 250-300 grams and monitoring the growth of suspected proliferating cancer cells weekly for 10 weeks prior to US or MR imaging until the evolution of a solid tumor nearly cost $4,000 ($30 per rat x 12 rats per week x 10 weeks). However, based on my volume growth measurements of PC3-luc-SQ (take-rate - 3 out of 3 animals) prostate tumors and PC3-luc-ORTHO (take-rate - 6 out of 9 animals) prostate tumors implanted in adult male nude rats using a mechanical caliper or US imaging revealed that MR imaging should be implemented approximately a month after tumor implantation (Figure 3.3). Interestingly, the tumor take-rates for PC3-luc-SQ and PC3-luc-ORTHO are comparable with what Andresen *et al.* have seen in 22RV1 (human prostate cancer) implanted orthotopically in Charles River or Taconic nude rats which have marked differences in appearance with respect to hair coat and pattern [131]. When using mice for experimental tumor models, the cost can be less when imaging five (5) mice at a time versus imaging one (1) rat at a time.

For my studies, it was uncertain whether no *in vivo* BLI signal (Group 1) or a decline in *in vivo* BLI signal (Group 2) was associated with the condition of the adult male nude rat immune system at the time of implantation. Typically the nude rats exhibit deficient T-cell activity as a result of T-lymphocyte depletion in regions of lymph nodes [131]. Andresen *et al.* illustrated that the choice of vendor as the source of purchasing immunodeficient rats for pre-clinical cancer studies may be of great importance [131]. Furthermore, the investigators reported that as the nude rats age they develop cells that resemble T-cell activity [131] which suggest that these species have evolved to counteract the tendency of mutant cells to proliferate. However, my pre-clinical cancer

studies have demonstrated obvious growth of solid PC3-luc prostate tumors in nude rats. Nevertheless, whole body radiation (approximately 2Gy) before tumor implantation of PC3-luc human cancer cells may alleviate issues with no or decreasing *in vivo* BLI signals during the growth of the proliferating cancer cells but this have not been tested..

Even after the extraction of an orthotopic prostate tumor I did not observe any *ex vivo* BLI signals after the injection of *D*-luciferin. Consequently, the status of clonal selection or possible gene silencing in the *luc*-gene may explain the inconsistency in the *in vivo* BLI signals.

Previous investigators [110] have suggested that the presence of luciferase in high levels may decrease the growth of *in vivo* tumors. However, this hypothesis was contradicted by others [130] illustrated by their green fluorescent protein (GFP) linked to firefly luciferase *in vitro* and *in vivo* studies in mice. Interestingly, some investigators dispute the fact that tumor hypoxia can potentially influence significant variability of BLI signals as the tumors grows [109,110,130,132]. Khalil *et al.* advocate (through firefly luciferase *in vitro* and *in vivo* cancer studies in mice) that the changes in tumor phenotypes, such as hypoxia or pH, correlate with the changes in the *in vivo* BLI signals and that the actual size of tumors monitored over time can be underestimated which can especially be important when measuring the volume of orthotopic prostate tumors [109]. Interestingly, this reasoning agrees with the analysis of my data considering that my experimental tumor models (PC3-luc-SQ or PC3-luc-ORTHO tumors) illustrated no or decreasing *in vivo* BLI signals but experienced the evolution and growth of tumors. However, according to Dr. Mason's Lab Manager (Jeni Gerberich) the PC3-*luc* cells had no BLI signal after one passage of cells to a well plate.

Conclusion

        While *in vivo* BLI is particularly simple, it is a sophisticated method of observing the growth of tumors; notably even sub-palpable volumes should be detected. My human xenograft studies have determined that the application of *in vivo* BLI for small animal cancer studies has significant uncertainty when monitoring the growth of PC3-luc prostate tumors in adult male nude rats. Indeed, additional investigation regarding the choice of small animal vendor source, immune status, gene expression of the *luc*-gene in adult male nude rats, or tumor physiological changes must be taken into consideration before pursuing *in vivo* BLI for high-throughput [106,112,123,133] pre-clinical cancer studies.

Chapter 4

Oxygen-Enhanced MRI for Non-Invasive Assessments of Rat and Human Orthotopic

Prostate Tumor Models

Abstract

Purpose

To assess the changes of the potential non-invasive prognostic biomarkers (blood-oxygen level dependent (BOLD %ΔSI), tissue-oxygen level dependent (TOLD %ΔSI), intrinsic longitudinal relaxation rate (ΔR_1), and apparent transverse relaxation rate (ΔR_2^*)) in rat and human orthotopic prostate tumors using Oxygen-Enhanced Magnetic Resonance Imaging (OE-MRI).

Methods

Dunning R3327-AT1 syngeneic rat prostate tumors were implanted subcutaneously (Group 1, *n = 5* and Group 2, *n = 6*) or orthotopically (Group 3, *n = 6*) in Copenhagen rats and PC3-luc prostate cancer cells were implanted in adult male nude rats orthotopically (Group 4, *n = 5*). Tumors were allowed to grow to intermediate or large volumes (1.3 – 20 cm^3). OE-MRI biomarkers were measured using a Varian 4.7T small animal MR scanner.

Results

OE-MRI biomarkers exhibited various responses to inhaling oxygen. Histology and immunohistochemistry studies confirmed OE-MRI results. Overall (*n* = 21), strong correlations were determined between BOLD %ΔSI and TOLD %ΔSI (*R* = 0.92, *P* < 0.0001) or ΔR_2^* (*R* = -0.93, *P* < 0.0001) and between TOLD %ΔSI and ΔR_2^* (*R* = -0.91, *P* < 0.0001).

Conclusion

OE-MRI confirms the response of tumors to breathing oxygen. Human prostate tumors appear to be less hypoxic compared to rat prostate tumors and may benefit when inhaling oxygen during irradiation. If tumor oxygenation does correlate with OE-MRI parameters as suggested by others, then patients may benefit when using specific oxygen-sensitive data in radiation treatment plans.

Introduction

Hypoxic regions exist in human prostate carcinoma [27,29]. Tumor response to radiotherapy [25,37,73] is affected by the status of tumor oxygenation or tumor hypoxia, since hypoxic cells resist radiation damage (nearly 3 times more dose) compared to oxygenated cells [20]. Normal tissue physiology is different from that of tumors. Solid tumor vasculature tends to be irregular in shape, where the basic internal surface elements such as an endothelial layer lacks contact with circulating blood [66]. Solid tumor microcirculation is much leakier compared to normal tissue resulting in sluggish flow of blood limiting delivery of blood and oxygen resulting in tumor hypoxia [67]. In addition, tumor hypoxic stress appears to influence the progression of malignancy and metastasis of cancer cells [67]. Consequently, investigating tumor radiobiology non-invasively has clinical relevance. Tumor hypoxia in regards to radiation response has been a topic of investigation since the early 1900's [20], which sparked several imaging methods for evaluating oxygenation of tumors subsequently [48,67]. OE-MRI parameters (BOLD %ΔSI, TOLD %ΔSI, ΔR_1, or $\Delta R_2{}^*$) used for assessing tumor oxygenation non-invasively appear to be gaining momentum among the many imaging methods that have been used to investigate tumor oxygenation [33,34,37,49,51,134-138]. Thus, non-invasive assessment regarding the oxygenation status (enhanced by hyperoxic gas

challenge) of solid tumors can be measured or for investigating interventions regarding cancer, notably, the response to radiation therapy.

Oxygenation in tumor tissue has been shown to influence the magnetic resonance (MR) physical parameters such as the intrinsic longitudinal relaxation rate (R_1). Investigations regarding R_1 revealed that molecular oxygen when inhaled and dissolved in tissue fluid or blood plasma may alter the R_1 values because molecular oxygen has paramagnetic characteristics [51,135]. Similarly, alteration of R_2^* values can be observed in the blood due to the magnetic susceptibility difference between oxy- and deoxyhemoglobin [37,51,138,139] because deoxyhemoglobin also has paramagnetic characteristics. Molecular oxygen and deoxyhemoglobin are paramagnetic because they have unpaired electrons. These unpaired electrons or magnetic dipole moments are subjected to a magnetic torque when placed in a magnetic field which accounts for paramagnetism. This local magnetic field is perturbed, modulating the available MR signal due to the energy exchange between the unpaired electrons and water protons at the time of imaging. Consequently, investigations have led to the assessments of tumor oxygenation using BOLD %ΔSI or TOLD %ΔSI responses as an imaging technique [37].

The previously mentioned responses are collectively referred to as OE-MRI parameters and are non-invasively acquired by using a hyperoxic gas challenge (e.g. 100% oxygen) during the acquisition of MR images. Prior to irradiation of solid tumors, OE-MRI responses appeared to provide potential prognostic biomarkers and predict the response to radiation [37], though the predictive value may also depend on the tumor type or size [22,23,25,26,37]. Many of these previous investigations regarding the dynamics of tumor oxygenation were assessed non-invasively in rat prostate tumors [37,134], rat pituitary tumors [138], rat breast tumors [136] or human prostate tumors [138] implanted subcutaneously in mice. However, little is known about such responses

in orthotopic prostate tumors which are important for comparison with similar investigations (oxygen electrode) previously implemented by Movsas *et al*. [28] and others [98,140,141]. Thus, given that OE-MRI prognostic biomarkers can be assessed non-invasively and there is a lack of response data available regarding orthotopic prostate tumors, the purpose of this study was to assess the OE-MRI measurements under hyperoxic gas challenge in rat and human prostate tumor models.

Methods and Materials

Ethical Statement

Refer to Chapter 3 for ethical statement.

Animals and Experimental Tumor Models

Pre-clinical subjects were 22 adult male rats. Seventeen (17) Copenhagen rats (strain code: 286, weighing approximately 270-330 g and 8 weeks old) were obtained from Charles River and housed no more than three rats per cage. Five (5) nude rats (strain model CR: NIH-RNU weighing approximately 287-320 g and six (6) weeks old) were obtained from the National Cancer Institute (NCI, Frederick, MD) and housed in a specific pathogen free facility with 3 rats per cage. Animals were classified into four groups. Group 1 (intermediate AT1 subcutaneous tumors, *n = 5*), Group 2 (large AT1 subcutaneous tumors, *n = 6*), Group 3 (large AT1 orthotopic tumors, *n = 6*), and Group 4 (large PC3-luc orthotopic tumors, *n = 5*). Group 1 and Group 2 tumors were surgically implanted subcutaneously in the right flank as described previously [37] and Group 3 tumors were surgically implanted orthotopically into the actual prostate with fresh fragments of syngeneic Dunning R3327-AT1 prostate tumors. The AT1 is a well-characterized anaplastic prostate tumor that doubles in volume every 5.2 days, thus well-suited for radiobiological studies as previously described by others [142]. Group 4

67

consisted of surgically implanting approximately 2.5 x 10^6 PC3-luc human prostate cancer cells [114,123] into the prostate to generate tumors as previously described [124]. Tumor volumes were calculated using magnetic resonance imaging or mechanical caliper as V = $(\frac{\pi}{6}) \times l \times w \times d$ where l, w, and d are orthogonal diameters. Subcutaneous tumor models were allowed to grow and ready for MR imaging when they reached greater than 3 cm^3 in volume, typically around 25-30 days after implantation. However, orthotopic tumors were allowed to grow to large volume or until physical examination in the vicinity of the prostate or bladder indicated the evolution of a solid mass.

Oxygen-Enhanced Magnetic Resonance Imaging

Hyperoxic Gas Challenge

All animals were anesthetized with 2.0-3.0% isoflurane with air and maintained under anesthesia with 1.5-2.0% of isoflurane with air (1 L/min). Oxygen (1 L/min) was used as a breathing challenge while the animals were under anesthesia to acquire OE-MRI measurements.

Magnetic Resonance Imaging

During the MR imaging experiments using a Varian 4.7T small animal MR scanner, the anesthetized (typical) animals were provided with a circulating warming pad to maintain body temperature at approximately 37°C. Physiological parameters (temperature, respiration rate, and % O_2 saturation) were monitored and recorded during MR imaging (MR-compatible Model 1025 Monitoring & Gating System, SA Instruments, Inc., Stony Brook, NY, USA). Rat's rectal temperatures was measured using a thermistor-type rectal probe with a temperature range from 10 to 70°C ± 0.2°C. Respiration rates were measured near the rat's abdomen using a pneumatic pillow

sensor having a recording range from 15 to 300 bpm and accuracy of one count. Fiber optic sensors with collars were placed in clips to measure the $\%O_2$ blood saturation on the rat's foot, hand, or arm. To achieve a MR signal at optimum conditions, the radiofrequency (RF) volume coil was tuned to proton (^1H) resonance frequency (approximately 200 MHz) and matched to the characteristic impedance of the coil to approximately 50 Ohm. The magnetic field in the MR scanner underwent a shimming process to improve the homogeneity of the magnetic field in the region of interest. This maximized the MR signal during the MR imaging experiment. After shimming the magnetic field, scout images (axial, coronal, and sagittal images) were acquired by using a gradient echo sequence. These images were used to plan for acquiring anatomical images. The anatomical images or T_2-weighted images were acquired using a fast spin echo sequence as previously described [37,49] but with slight modifications (FOV = 60 x 60, 2 mm slice thickness) to sequence imaging slice plane. In addition, quantitative R_1 (R_1 = 1 / T_1) measurements were acquired as previously described [37,49] using a sequential variable repetition time (TR) 2-D multi-slice spin-echo sequence. Quantitative R_1 measurements were obtained while the animals inhaled air and oxygen. An interleaved dynamic blood-oxygen level dependent (BOLD or T_2*) and tissue-oxygen level dependent (TOLD or T_1) or simply an IBT data acquisition [37] was used in between acquiring quantitative R_1 measurements by using a baseline of air for up to 10 minutes and an oxygen breathing challenge for up to 10 minutes. In general, the BOLD sequence was a 2-D multi-slice spoiled gradient-echo with multi-echo sequence and the TOLD sequence was a 2-D multi-slice spoiled gradient-echo sequence as previously described [37] and presented in Chapter 2. OE-MRI imaging protocol is described below and as shown in Table 4.1.

➤ Anatomical or T_2-weighted images acquired using a fast spin echo (FSEMS) sequence (TR/TEeff = 2000/48 ms, ETL = 8, NEX = 8, Matrix = 128 x 128, FOV =

69

60-70 mm x 60-70 mm, Slices = 20, Slice Thickness = 2 mm, Scan Time = 4 min 16 s);

➢ Sequential variable repetition time (TR) 2-D multi-slice spin-echo (SEMS) sequence (TR = 100/ 200/ 300/ 500/ 700/ 900/ 1500/ 2500/ 3500 ms, TE = 20 ms, NEX = 1, Slice plan = T_2-weighted images, Slices = 3, Total scan time ~ 22 minutes) for baseline R_1.

➢ Interleaved BOLD and TOLD data acquisition or (**IBT**).
  - BOLD or T_2* used a 2-D multi-slice spoiled gradient-echo with multi-echo (MGEMS) sequence (TR/TE = 150/6-69 ms, Echo Spacing = 7 ms, Flip Angle = 20°, NEX = 3, Slices = 2, Scan Time = 57.6 s).
  - TOLD or T_1 used a 2-D multi-slice spoiled gradient-echo (GEMS) sequence (TR/TE = 30/5 ms, Flip Angle = 45°, NEX = 1, Slices = 1, Scan Time = 7.8 s).

➢ SEMS sequence for oxygen challenge R_1.

Table 4.1 Imaging protocol for OE-MRI measurements under hyperoxic gas challenge.

AIR			OXYGEN	
~4 min	~22 min	5-10 min	5-10 min	~22 min
		Dynamic IBT		
Anatomical Imaging	R_1	R_2*	R_2*	R_1

Histology

Assessments regarding tumor necrosis were performed on a large orthotopic PC3 (n = 1) and on a large AT1 tumor (n = 1) after the rats were killed to collect the tumor tissue. H&E staining was performed on these tumor tissues after OE-MRI and the percent (%) tumor necrosis was determined using Matlab (MathWorks, Natick, MA, USA) as described previously [26]. In addition, tumor necrosis was assessed on intermediate AT1 (n = 2) tumors.

Immunohistochemistry

Tumor hypoxia was assessed for the same large tumors using tumor hypoxia marker pimonidazole HCl (Hydroprobe™-1, Hypoxyprobe, Inc., Burlington, MA, USA. 60

mg/kg body weight) dissolved in saline immediately after OE-MRI, while inhaling oxygen. Positively stained pimonidazole relative to total tissue was determined (the % hypoxic marker [26]) using Matlab (MathWorks, Natick, MA, USA). In addition, tumor hypoxia was assessed on intermediate AT1 (n = 2) tumors to compare with their OE-MRI measurements.

OE-MRI Data Analysis

All image post-processing of OE-MRI data was performed using in-house algorithms developed in Matlab (MathWorks, Natick, MA, USA). Voxel-by-voxel %ΔSI in BOLD and TOLD responses with respect to inhaling 100% oxygen were calculated from the whole tumor region-of-interest (ROI) from dynamic BOLD and TOLD images, respectively, as previously described [37] using the equation:

$$\%\Delta SI = \frac{SI_{OXYGEN} - SI_{AIR}}{SI_{AIR}} \times 100 \qquad (4.1)$$

where SI_{AIR} is the average ROI baseline signal intensity when inhaling air and SI_{OXYGEN} is the average ROI oxygen signal intensity when inhaling approximately 100% oxygen. In regard to BOLD images, a single echo time (TE = 20 ms) was selected for data analysis.

Voxel-by-voxel R_2* maps (R_2* = 1 / T_2*) were generated from BOLD images by fitting the multi-echo data to the echo time (TE) using a nonlinear least squares equation similar to that previously described [37]. Quantitative ΔR_2* values were calculated as ΔR_2* = [(R_2*)$_{OXYGEN}$ − (R_2*)$_{AIR}$]. ΔR_1 values were calculated as ΔR_1 = [(R_1)$_{OXYGEN}$ − (R_1)$_{AIR}$], where the quantitative R_1 maps used a nonlinear saturation recovery (SR) equation based on:

$$M_Z(t) = M_O(1 - e^{-R_1 \times tau}) \tag{4.2}$$

where $M_Z(t)$ is the time-dependent longitudinal magnetization based on the recovery back to equilibrium after an excitation pulse, M_O is the equilibrium nuclear magnetization, and tau is the repetition times used as previously described [37]. Only voxels that provided reliable fitting with a coefficient of determination $R^2 \geq 0.95$ throughout the processing of the digital images of the quantitative ΔR_1 and ΔR_2^* maps were used in statistical analysis.

Statistical Analysis

To implement an assessment of predictive OE-MRI biomarkers, a Pearson correlation matrix of response variables was assessed which provided the coefficient of simple correlation (*R*-value) between the OE-MRI variables in a scattered plot matrix. In addition, a between group comparison of the mean OE-MRI response changes was assessed using a general linear model (GLM). Tumor size at the time of OE-MRI measurements was used as an independent variable or covariate to help reduce the error variance within the model where possible, notably, the analysis of covariance [143]. A *P*-value less than 0.05 was deemed significant. All statistical analysis was evaluated using SAS 9.4 for Windows. Data values are reported as mean ± standard deviations.

Results

Oxygen-Enhanced Magnetic Resonance Imaging

Missing data shown as a hyphen in Table 4.3 resulted from significant image noise on BOLD (T_2^*-weighted) images or data not acquired. Physiological parameters during MR imaging were found to be valuable (Table 4.2). Overall, the change in

respiration rate (ΔRR) and temperature (ΔTemp) remained nearly unchanged during oxygen challenge, whereas the change in arterial oxygen saturation (ΔSpO_2) increased approximately 6%. Individual tumor results also showed distinctive OE-MRI responses regardless of tumor volume (Table 4.3). The mean ± standard deviation tumor size across all subjects was 7.9 ± 7.2 cm^3. However, the mean sizes of the tumors from Group 1 (1.8 ± 0.4 cm^3) were much smaller in volume compared to Group 2 (3.9 ± 0.9 cm^3), Group 3 (12 ± 8 cm^3), and Group 4 (14 ± 7 cm^3). Considering the overall mean response values of the whole tumor ROI, the semi-quantitative BOLD %ΔSI and TOLD %ΔSI responses across all subjects were observed to be -0.8 ± 10% and 1.0 ± 2.4%, respectively. Similarly, the quantitative ΔR_1 and ΔR_2* response values were observed from whole tumor ROI to be 0.04 ± 0.05 s^{-1} and -0.29 ± 2.8 s^{-1}, respectively. Representative dynamic BOLD %ΔSI or TOLD %ΔSI responses from each group of prostate tumors are illustrated in Figure 4.1. As shown in Figure 4.1, the dynamic BOLD or TOLD signals variously showed positive or negative impulse responses to inhaling oxygen for at least 10 minutes. The AT1-SQ tumor shown in Figure 4.1a had a relatively stable BOLD and TOLD baseline before responding to inhaling oxygen. Whereas, the TOLD baselines for the AT1-ORTHO and PC3-ORTHO tumors shown in Figures 4.1b and 4.1c, respectively, were less stable or very chaotic but responded well to inhaling oxygen. The BOLD %ΔSI and TOLD %ΔSI response maps for the example AT1 orthotopic prostate tumor response signals shown in Figure 4.1b are illustrated in Figures 4.2b and 4.2c. Additionally, the quantitative ΔR_1 and ΔR_2* maps are illustrated in Figures 4.2d and 4.2e. All the OE-MRI response maps exhibited tumor heterogeneity. The BOLD %ΔSI or TOLD %ΔSI response maps showed extensive tumor heterogeneity where the greatest changes tend to be around the periphery of the tumor. The threshold ΔR_1, and ΔR_2* response maps showed similar heterogeneity and increased signals

73

around the periphery of the tumor. A dynamic regional comparison (Figure 4.3) of the BOLD %ΔSI or TOLD %ΔSI response of an example AT1 orthotopic prostate tumor (Figure 4.2) illustrates an difference between a large response and small or no response within the tumor, thus demonstrating tumor heterogeneity. The regional BOLD %ΔSI and TOLD %ΔSI responses for ROI #1 were determined to be 5.03 ± 0.23 % and 3.40 ± 0.92 %, respectively. Similarly, the regional BOLD %ΔSI and TOLD %ΔSI responses for ROI #2 were determined to be -0.0598 ± 0.85 % and 0.56 ± 0.58 %, respectively. Among all the subjects (Figure 4.4), a strong positive correlation was observed between the BOLD %ΔSI and TOLD %ΔSI responses (R = 0.92, P < 0.0001). Also, a strong negative correlation was observed between the BOLD %ΔSI and ΔR_2* responses (R = -0.93, P < 0.0001). Similarly, I observed a strong negative correlation with TOLD %ΔSI and ΔR_2* responses (R = -0.91, P < 0.0001). Group 2 (AT1-SQ, n = 5, R = 0.97, P = 0.0232), Group 3 (AT1-ORTHO, n = 6, R = 0.97, P = 0.001), and Group 4 (PC3-ORTHO, n = 5, R = 0.93, P = 0.021) demonstrated strong positive correlations between BOLD %ΔSI and TOLD %ΔSI responses that was deemed significant. Strong negative correlations were observed between ΔR_2* and BOLD %ΔSI (R = -0.98, P = 0.0005) or ΔR_2* and TOLD %ΔSI (R = -0.98, P = 0.0004) from Group 3. I also observed a strong positive correlation between ΔR_1 and TOLD %ΔSI (n = 3, R = 0.99, P = 0.0041) from Group 3. Group 4 demonstrated a strong negative correlation between ΔR_2* and BOLD %ΔSI (R = -0.95, P = 0.0146).

Table 4.2 Physiological Parameters Results

Subject	Tumor Size (cm^3)	Baseline Respiration Rate (Breathe/min)	Δ Respiration Rate (Breath/min)	Baseline Temperature (°C)	ΔTemperature (°C)	Baseline SpO_2 (%O2 Saturation)	ΔSpO_2 (%O2 Saturation)	Tumor Type
Group 1								
1	2.1	41±3	-6.0±5	37±0.1	0.08±0.1	88±2	4.5±3	AT1-SQ
2	1.3	35±3	7±7	35±0	0.03±0.04	56±19	5.9±26	AT1-SQ
3	1.8	30±3	11±5	36±0.3	0.4±0.3	91±2	2.2±2	AT1-SQ
4	2.1	25±3	-1±4	37±0	0±0	73±1	4.5±2	AT1-SQ
5	1.6	35±0.8	0.02±2	32±0.01	-0.2±0.03	-	-	AT1-SQ
Group 1 Mean ± S.D	1.8±0.3	33±7	2.1±6.6	35.4±1	0.07±0.24	77±16	4.3±1.5	AT1-SQ
Group 2								
11	3.6	30±4	4.0±4	34±3	0.80±3	93±3	4.4±3	AT1-SQ
Group 2 Mean ± S.D	3.6	30	4.0	34	0.80	93	4.4	AT1-SQ
Group 3								
15	1.5	31±5	-3.6±7	22±0.03	-0.17±0.6	89±1	5±2	AT1-ORTHO
16	9.0	-	-	29±0.3	-0.31±0.3	81±3	14±4	AT1-ORTHO
Group 3 Mean ± S.D	5.3±5.3	31	-3.6	25.5±4.9	-0.24±0.09	85±5.7	8.1±5.5	AT1-ORTHO
Overall Mean ± S.D	3.6±1.8	32.5±4.7	0.83±3.96	33.6±4.9	0.21±0.53	81±13	5.6±2.2	

All values are mean ± standard deviation

Table 4.3 OE-MRI Response of Prostate Tumors

Subject	Tumor Size (cm^3)	BOLD %ΔSI	TOLD %ΔSI	ΔR$_1$ (s^{-1})	ΔR$_2$* (s^{-1})	Tumor Type
Group 1 – Intermediate AT1-SQ						
1	2.1	4.5±0.5	1.8±0.4	-	-1.5±29.6	AT1-SQ
2	1.3	-	4.0±0.6	-	-	AT1-SQ
3	1.8	1.2±0.6	1.5±0.5	-0.06±0.082	1.2±27.8	AT1-SQ
4	1.6	4.2±1.1	1.7±0.4	0.07±0.065	-3.1±24.4	AT1-SQ
5	2.1	0.7±0.1	0.9±0.6	0.03±0.954	-1.2±31.1	AT1-SQ
Group 1 Mean ± S.D	1.8±0.3	2.7±2.0	2.0 ±1.2	0.02± 0.06	-1.2±1.8	AT1-SQ
Group 2 – Large AT1-SQ						
6	3.5	-1.8±1.1	-0.5±2.6	0.01±0.113	0.4±8.5	AT1-SQ
7	3.6	0.4±0.4	1.0±1.4	0.04±0.093	-1.4±22.3	AT1-SQ
8	3.0	0.9±0.8	1.8±0.7	0.06±0.148	-0.8±51.1	AT1-SQ
9	5.5	3.0±0.4	1.8±0.8	0.14±0.106	-0.5±50.6	AT1-SQ
10	4.4	4.0±0.5	2.3±1.2	0.02±0.399	-1.1±47.1	AT1-SQ
11	3.6	-	0.7±0.6	0.05±0.147	-	AT1-SQ
Group 2 Mean ± S.D	3.9±0.9	1.3±2.3	1.2±1.0	0.05±0.05	-0.68±0.7	AT1-SQ
Group 3 – Large AT1-ORTHO						
12	15.8	-40.4±16	-7.4±2.2	-	10±13.5	AT1-ORTHO
13	19.9	-0.4±0.5	-0.2±0.4	-	-0.3±17.6	AT1-ORTHO
14	20.3	-11.6±10	-0.4±1.5	-	1.2±28.5	AT1-ORTHO
15	1.5	3.6±1.4	2.1±1.9	0.04±0.116	-1.1±13.2	AT1-ORTHO
16	9.0	1.3±0.5	0.4±0.2	0.01±0.043	0.1±11.2	AT1-ORTHO
17	4.5	1.7±0.8	1.0±0.3	0.02±0.055	0.2±12.3	AT1-ORTHO
Group 3 Mean ± S.D	12±8	-7.7±17	-0.8±3.4	0.024±0.01	1.7±4.1	AT1-ORTHO
Group 4 – Large PC3-ORTHO						
18	3.5	5.7±1.5	2.6±5.8	-	-4.1±11.6	PC3-ORTHO
19	12.7	8.1±2.8	5.6±5.6	-	-4.0±17.9	PC3-ORTHO
20	14.4	1.1±1.2	2.4±6.0	-	-0.3±16.1	PC3-ORTHO
21	20.3	-1.3±0.9	-0.1±0.3	-	1.0±26.2	PC3-ORTHO
22	20.1	-0.9±0.5	-0.5±0.3	-	-0.5±20.5	PC3-ORTHO
Group 4 Mean ± S.D	14±7	2.6±4.2	2.0±2.5	-	-1.6±2.3	PC3-ORTHO
Overall Mean ± S.D	7.9±7.2	-0.8±10	1.0±2.4	0.04±0.05	-0.29±2.8	
P-value[a]		0.1232	0.0479	0.7100	0.1040	

All values are mean ± standard deviation

a – *P*-values for group comparisons (general linear analysis) in differences in BOLD: blood-oxygenation level dependent ; TOLD: tissue-oxygenation level dependent; ΔR$_1$: intrinsic longitudinal relaxation rate; and ΔR$_2$*: apparent transverse relaxation rate

(a)

(b)

(c)
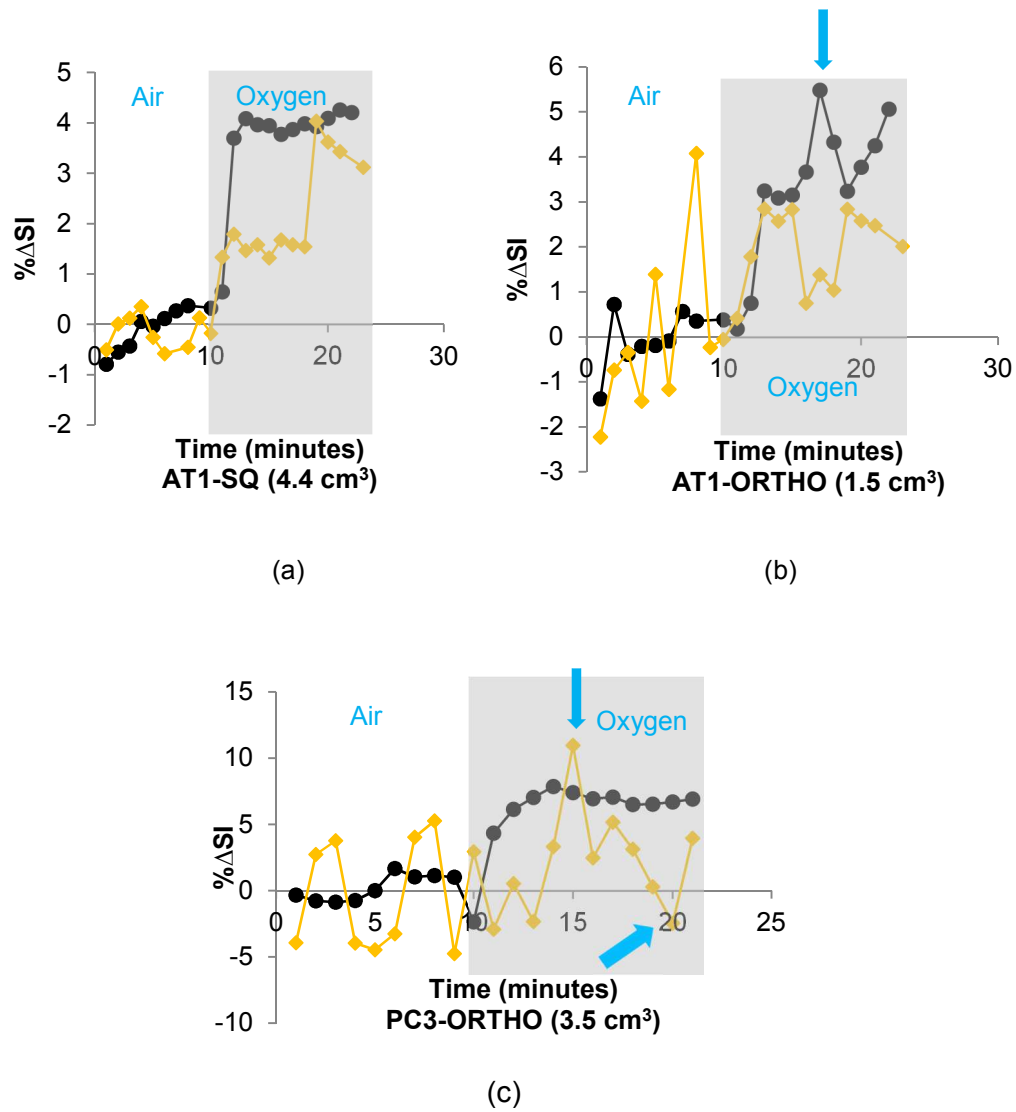
Figure 4.1   Representative dynamic **BOLD** and **TOLD** signal responses to inhaling oxygen for approximately 10 minutes with respect to inhaling baseline air.   Mean whole tumor ROI **BOLD** %ΔSI (•) and **TOLD** %ΔSI (♦) of (a) AT1-SQ (4.4 cm^3), (b) AT1-ORTHO (1.5 cm^3), and PC3-ORTHO (3.5 cm^3).   Arrows illustrates positive or negative impulse responses to inhaling oxygen.
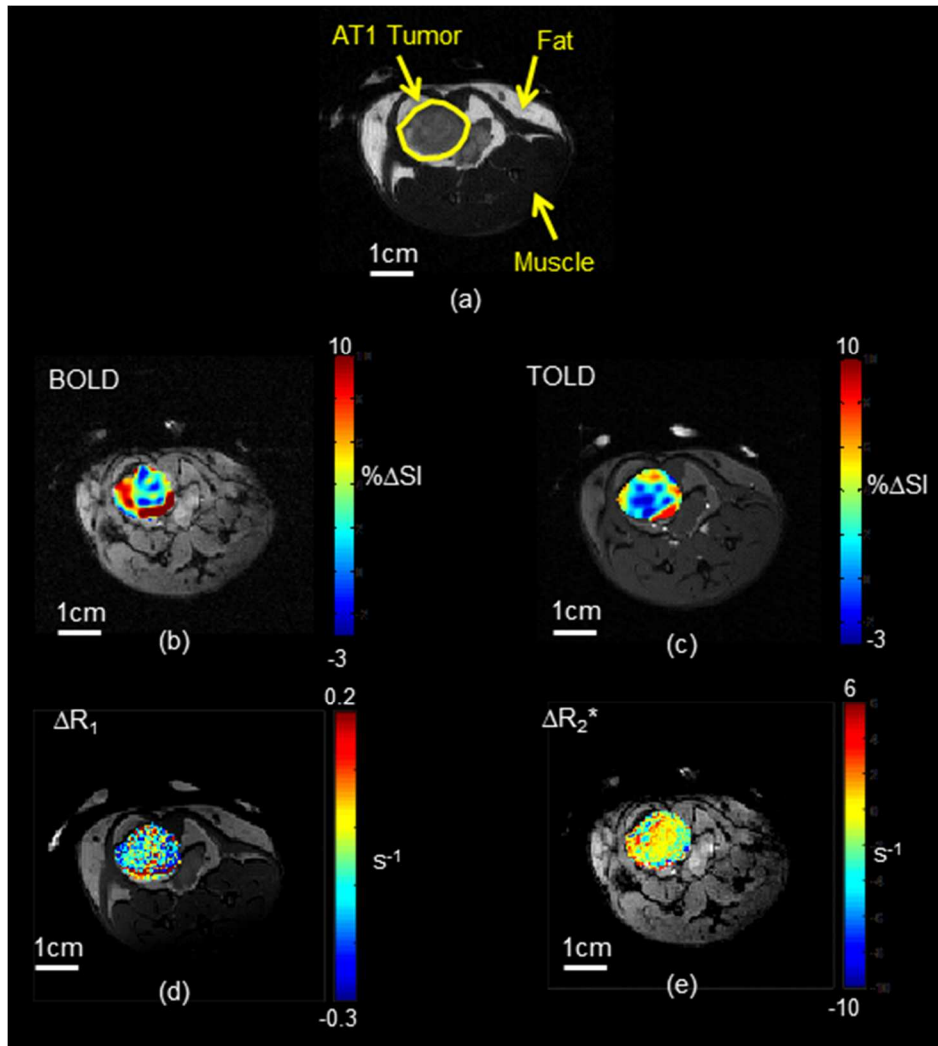
Figure 4.2 Oxygen-Enhanced MRI. Whole tumor ROI (a) BOLD %ΔSI, TOLD %ΔSI, ΔR_1, and ΔR_2* response maps for a representative orthotopic Dunning prostate R3327-AT1 prostate tumor (Group 2 – Tumor # 4, 1.5 cc). The BOLD %ΔSI and TOLD %ΔSI response maps are shown on high-resolution T_2*-weighted and T_1-weighted images with respect to inhaling (b, c) oxygen at 16 and 13 minutes, respectively, during the experiment (see Figure 2(b) for reference). The ΔR_1 (on high-resolution PD-weighted image) and ΔR_2* (on high-resolution T_2*-weighted image) response maps are the differences between the mean baseline air and oxygen (d, e).
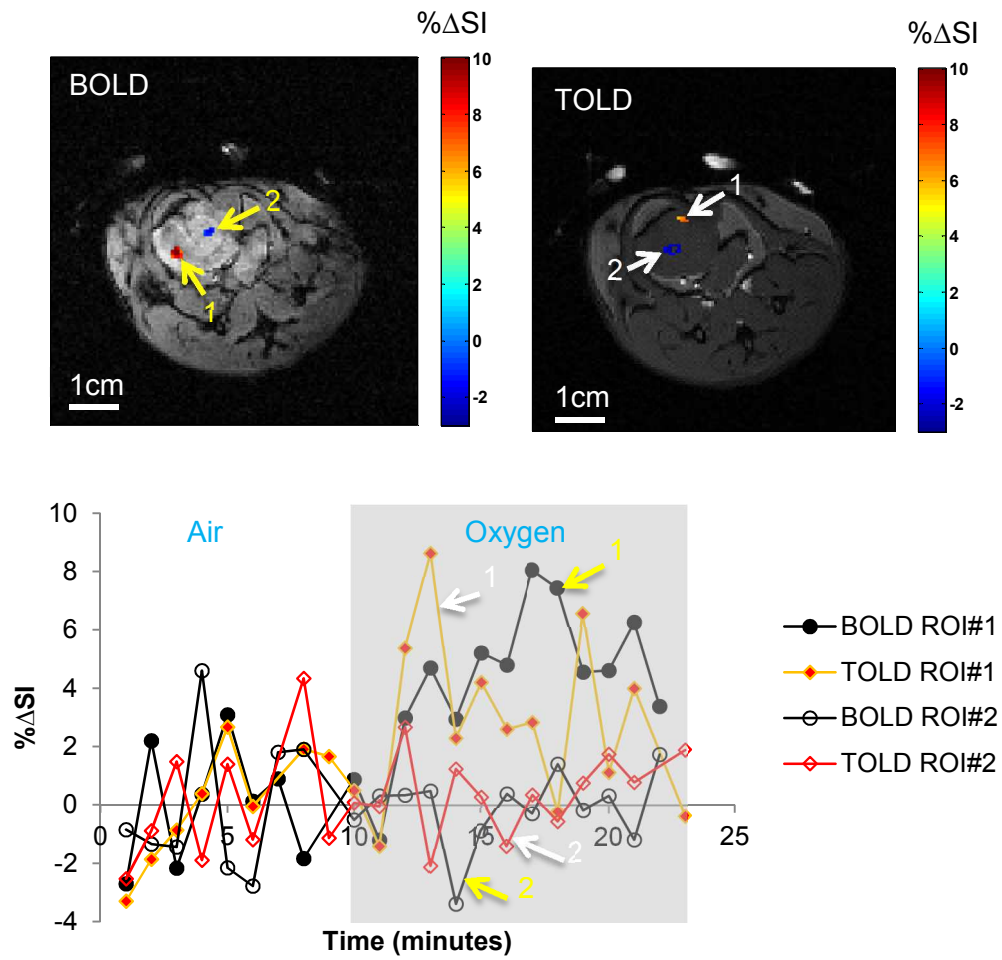
Figure 4.3   Mean regional observations of BOLD %ΔSI and TOLD %ΔSI responses in Dunning prostate R3327-AT1 orthotopic (AT1-ORTHO) prostate tumor (Group 2 – Tumor # 4, 1.5 cc).
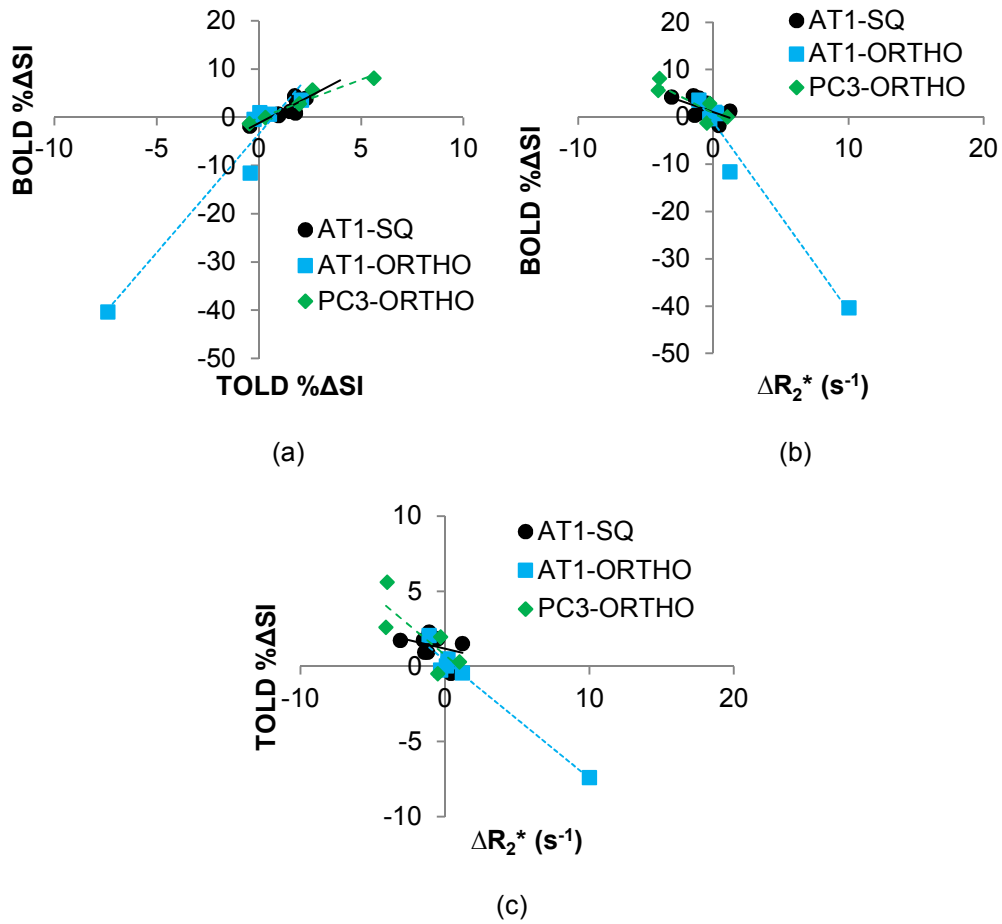
Figure 4.4 Observed correlations between OE-MRI values across all subjects (n = 22). BOLD %ΔSI and TOLD %ΔSI (a) or ΔR_2* (b) or TOLD %ΔSI and ΔR_2* (c) response values derived from respective maps. Line of best fit for Dunning prostate R3327-AT1 subcutaneous (AT1-SQ, solid ●) or orthotopic (AT1-ORTHO, dashed ■) prostate tumors. PC3-luc orthotopic (PC3-ORTHO, dashed ◆) prostate tumors are also illustrated with best line fit.
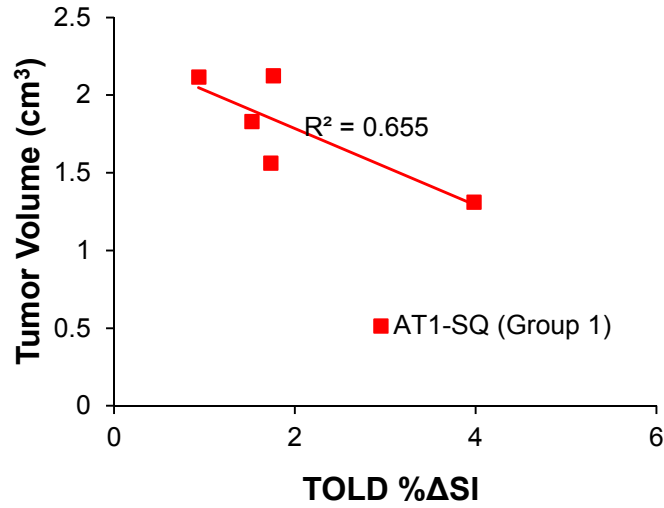
(a)
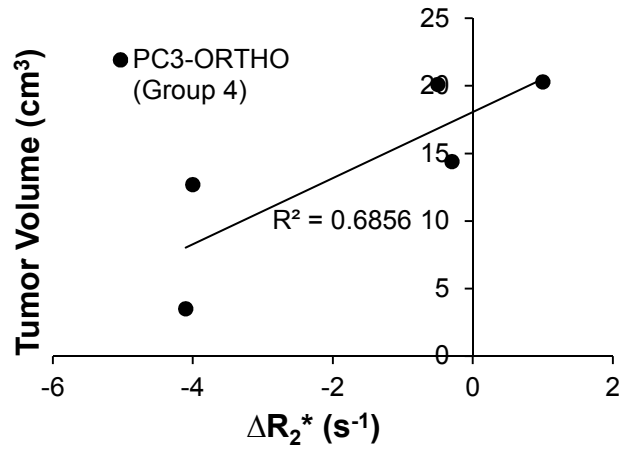
(b)

Figure 4.5 Tumor size correlated with (a) TOLD %ΔSI in Group 1 AT1-SQ tumors (mean volume = 1.8±0.3 cm^3) and (b) ΔR_2^* in Group 4 PC3-ORTHO tumors (mean volume = 14±7 cm^3). Line of best fit for Dunning prostate R3327-AT1 subcutaneous (AT1-SQ, solid ■) and PC3-luc orthotopic (PC3-ORTHO, solid ●). No correlation existed between tumor size and Group 2 or Group 3.

A weak correlation was determined between tumor volume and BOLD %ΔSI (R = -0.41, P = 0.074) or TOLD %ΔSI (R = -0.41, P = 0.0586) across all subjects. On the other hand, a strong correlation was determined between tumor volume and TOLD %ΔSI with-in Group 1 (Figure 4.5a, AT1-SQ, n = 5, R = -0.83, P = 0.0784) or ΔR_2* with-in Group 4 (Figure 4.5b, PC3-ORTHO, n = 5, R = 0.83, P = 0.0834). A between group comparison of the least-squares mean OE-MRI response was assessed. Groups 1 (AT1-SQ, n = 5) and 2 (AT1-SQ, n = 6) did not demonstrate a significant difference from the other groups. However, the TOLD %ΔSI response demonstrated a significant difference in Group 4 (PC3-ORTHO, n = 5) compared to Group 3 (AT1- ORTHO, n = 5, P = 0.0184) when the tumor sizes were considered as an uncontrolled variable or covariate in my model (Equation 4.3, R^2 = 0.41, P = 0.0479). Similarly, the BOLD %ΔSI response demonstrated a significant difference in Group 4 (PC3-ORTHO, n = 5) compared to Group 3 (AT1-ORTHO, n = 6, p = 0.0475) when the tumor sizes were considered as an uncontrolled variable or covariate in our model (Equation 4.4, R^2 = 0.37, P = 0.1232). Furthermore, the ΔR_2* response demonstrated a significant difference in Group 4 (PC3-ORTHO, n = 5) compared to Group 3 (AT1-ORTHO, n = 6, p = 0.0279) when the tumor sizes were considered as an independent variable or covariate in our model (Equation 4.5, R^2 = 0.34, P = 0.1040). Equations 4.3, 4.4, and 4.5 are predictive models for estimating the TOLD %ΔSI, BOLD %ΔSI, and ΔR_2* responses, respectively, based on the size and type of tumor.

$$\text{TOLD \%}\Delta\text{SI} = \begin{cases} (1.613) - 0.201(\text{Tumor Volume}), \text{if Tumor Type} = \text{AT1} - \text{SQ} \\ (1.596) - 0.201(\text{Tumor Volume}), \text{if Tumor Type} = \text{AT1} - \text{ORTHO} \\ (4.86) - 0.201(\text{Tumor Volume}), \text{if Tumor Type} = \text{PC3} - \text{ORTHO} \end{cases} \qquad (4.3)$$

$$\text{BOLD \%}\Delta\text{SI} = \begin{cases} (4.12) - 0.768(\text{Tumor Volume}), \text{if Tumor Type} = \text{AT1} - \text{SQ} \\ (2.05) - 0.768(\text{Tumor Volume}), \text{if Tumor Type} = \text{AT1} - \text{ORTHO} \\ (13.46) - 0.768(\text{Tumor Volume}), \text{if Tumor Type} = \text{PC3} - \text{ORTHO} \end{cases} \quad (4.4)$$

$$\Delta R_2^*(s^{-1}) = \begin{cases} (-1.56) + 0.214(\text{Tumor Volume}), \text{if Tumor Type} = \text{AT1} - \text{SQ} \\ (-0.86) + 0.214(\text{Tumor Volume}), \text{if Tumor Type} = \text{AT1} - \text{ORTHO} \\ (4.63) + 0.214(\text{Tumor Volume}), \text{if Tumor Type} = \text{PC3} - \text{ORTHO} \end{cases} \quad (4.5)$$

Histology and Immunohistochemistry

Histological studies from two (2) representative intermediate subcutaneous tumors in Group 1 (AT1-SQ tumor #4 and tumor #5) supported BOLD %ΔSI and TOLD %ΔSI responses, as shown in Figure 4.6. Pimonidazole immunohistochemistry staining for Group 1 tumor #4 and tumor #5 compared well with BOLD %ΔSI and TOLD %ΔSI maps illustrating high and low BOLD and TOLD responses, respectively. In addition as shown in Table 4.4, the tumor hypoxic fraction using pimonidazole (HF_{pimo}) matched well with the results of the OE-MRI parameters having a small response or large response at the time of inhaling oxygen. Similarly, histological studies from representative large orthotopic prostate tumors observed from Groups 3 (AT1-ORTHO tumor #12) and 4 (PC3-ORTHO tumor #18), respectively, match well with their corresponding anatomical images (Figure 4.7). The histological findings support the responses from the BOLD %ΔSI and TOLD %ΔSI maps shown in Figure 4.8. The % necrosis and % hypoxic marker pimonidazole for representative orthotopic tumors are shown in Table 4.5.

Table 4.4 Two intermediate AT1-SQ tumors demonstrate distinct responses to inhaling oxygen. Tumor hypoxia marker (pimonidazole) confirm with a small OE-MRI measurement response vs. a large OE-MRI measurement response.

Tumor Volume	Whole Tumor (HF_{pimo})	BOLD (%ΔSI)	TOLD (%ΔSI)	ΔR_1 (s^{-1})	$\Delta R_2{}^*$ (s^{-1})
1.6	21%	4.2	1.7	0.0722	-3.1
2.1	42%	0.73	0.94	0.0289	-1.2
% Difference	68	141	60	86	88

$$\% \text{ Difference} = \frac{|a - b|}{\text{mean}(a, b)}$$
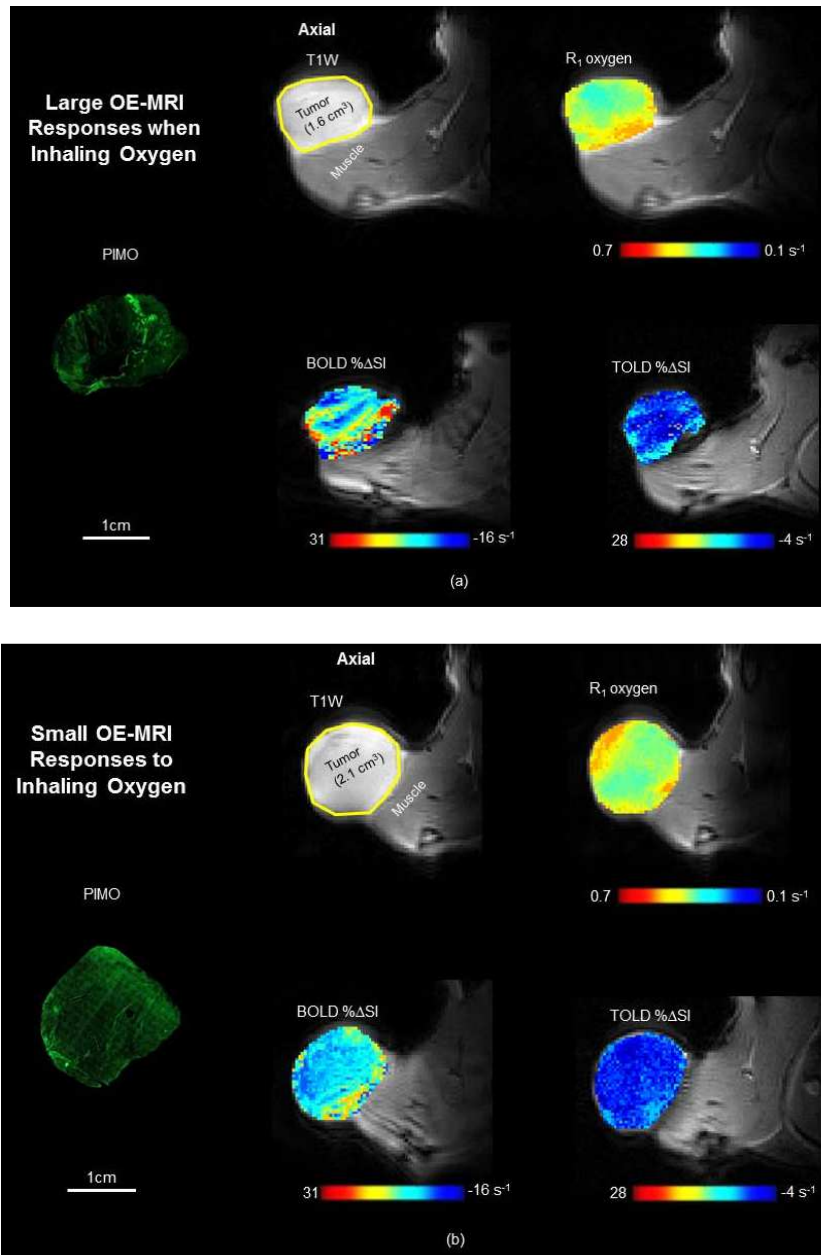
Figure 4.6 Comparison between (a) small OE-MRI measurement response (tumor #4) vs. (b) large OE-MRI measurement response (tumor #5) with Tumor Hypoxia Maker Pimonidazole for two intermediate AT1-SQ tumors (Group 1). Refer to Table 4.4.
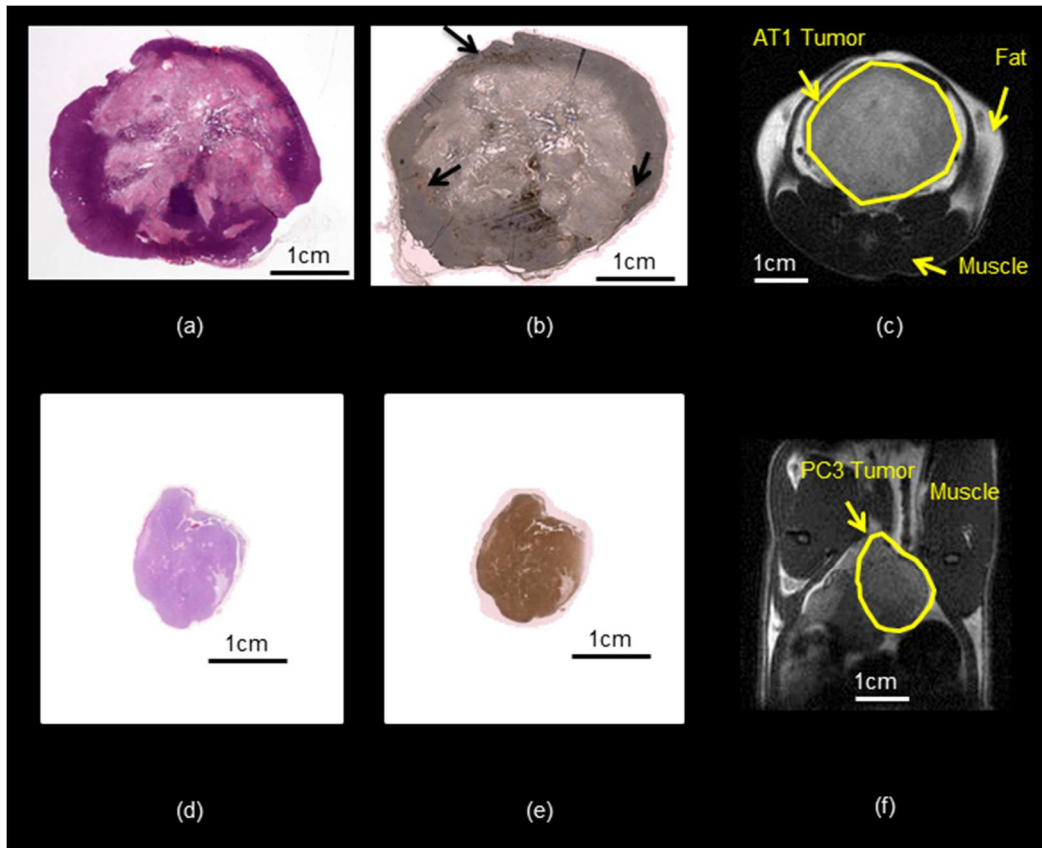
Figure 4.7 Histological observations of representative large rat AT1 and human prostate tumors. (a-c) From top left to right consist of H&E staining, pimonidazole, and high-resolution T_2-weighted image (axial view) of a large orthotopic AT1 prostate tumor (Group 2 – Tumor # 12, 15.8 cm^3) showing considerable necrosis concentrated mainly in the center of tumor and hypoxia (arrows) along the periphery of the tumor (arrows). (d-f) From bottom left to right consist of H&E staining, pimonidazole, and high-resolution T_2-weighted image (coronal view) of a large orthotopic PC3-*luc* prostate tumor (Group 3 – Tumor # 18, 3.5 cm^3) showing a moderate uniform distribution of hypoxia but with no signs of center necrosis.
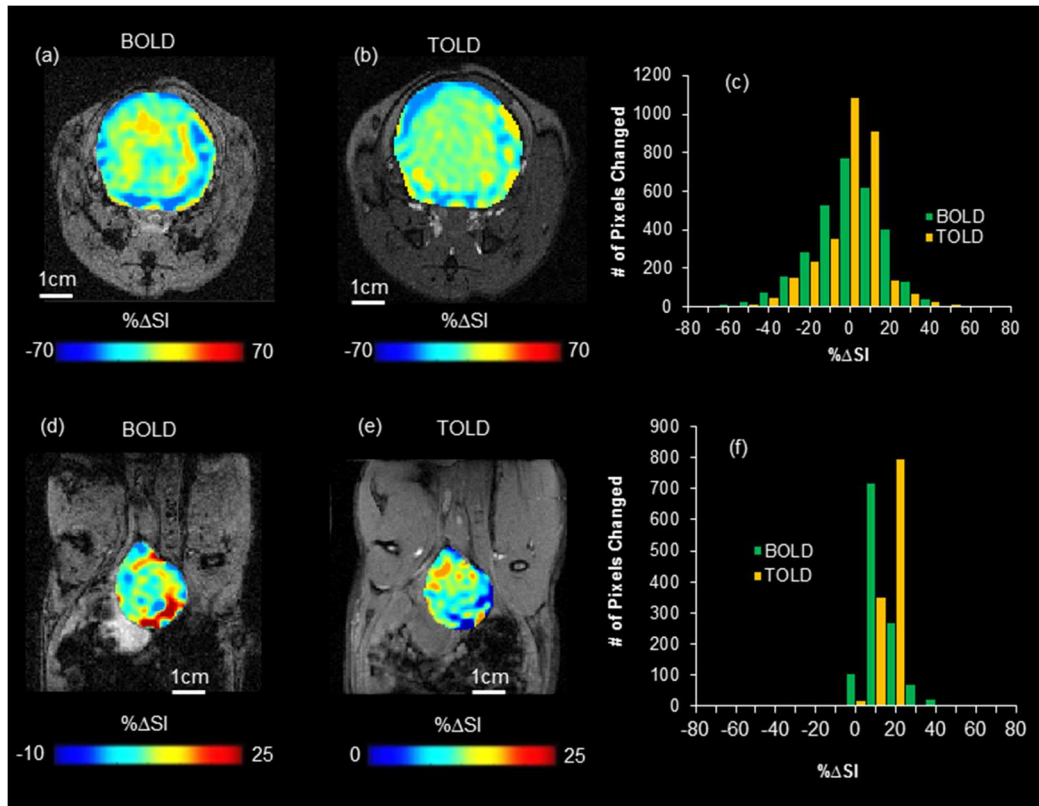
Figure 4.8 BOLD %ΔSI and TOLD %ΔSI response maps. Whole tumor ROI (a, b) BOLD %ΔSI and TOLD %ΔSI response maps for a representative orthotopic Dunning prostate R3327-AT1 prostate tumor (Group 2 – Tumor # 12, 15.8 cc). (d, e) BOLD %ΔSI and TOLD %ΔSI response maps for a representative orthotopic PC3-luc prostate tumor (Group 3 – Tumor # 18, 3.5 cc).   The BOLD %ΔSI and TOLD %ΔSI response maps are shown on high-resolution T_2*-weighted and T_1-weighted images with respect to inhaling (d, e) oxygen at 14 and 15 minutes, respectively, during the experiment (see Figure 2(c) for reference). (c, f) Corresponding histograms (bin range in 10 %ΔSI) of the number of pixels that changed with respect to inhaling oxygen.

Table 4.5 Histological Values of Representative Large Orthotopic Prostate Tumors

Tumor Model	Tumor Size (cc)	Necrosis (%)	Hypoxia Marker Pimonidazole (%)
Large AT1 (*n* = 1)	15.8	49	18
Large PC3 (*n* = 1)	3.5	6.9	4.3

Discussion

The status of tumor oxygenation before radiation damage is an important consideration for predicting the response to radiation non-invasively. Better oxygenated tumors are expected to respond to radiation than poorly oxygenated tumors. In this study, I found that Dunning R3327-AT1 and PC3-luc orthotopic prostate tumors were different in their OE-MRI responses at large tumor volumes. The intermediate volume tumors in Group 1 (AT1-SQ, *n* = 5) had comparable OE-MRI measurements overall with Group 4 (PC3-ORTHO, *n* = 5) large volume PC3-luc prostate tumors. Immunohistochemistry and calculations of tumor hypoxic fraction from Group 1 confirmed the differences I have observed between large or small OE-MRI measurements when animals are inhaling oxygen. These observed measurements can be particularly important for stratification and predicting the response to radiation. According to my histological studies of the orthotopic prostate tumors, the large AT1 tumor was severely necrotic with peripheral pockets of hypoxia consistent with previous reports of AT1 tumor oxygen status as the AT1 tumor growth [144]. The hypoxia of the large PC3 tumor seemed uniform in regard to the distribution of pimonidazole intensity. The large AT1 was severely necrotic in the center of the tumor with pockets of hypoxia along the

periphery of the tumor. To my knowledge no one has attempted to capture data regarding the oxygen dynamics of orthotopic AT1 or PC3-luc prostate tumors in rats. All prostate tumors shown in this study exhibited significant tumor heterogeneity which may affect the response to radiation damage. Based on the correlations, the OE-MRI prognostic biomarkers measured in tumors responded to inhaling oxygen of both subcutaneous and orthotopic prostate tumors non-invasively and may provide insight to the prognosis on the response to radiation damage.

In a previous study, Bourke et $al.$ [145] observed a group of well oxygenated large volume subcutaneous AT1 prostate tumors with a mean partial pressure of oxygen (pO_2) greater than 10 mm Hg that responded well to irradiation. They also noticed that poorly oxygenated tumors responded to irradiation very differently depending on the pO_2 status of the tumors. In addition, strong correlations were found between the tumor pO_2 and the tumor volume doubling time (VDT) following irradiation. The observations of Bourke et $al.$ were significant. However, entirely non-invasive measurements of oxygenation status would be preferable [146]. So-called DOCENT (Dynamic Oxygen Challenge Evaluated by NMR T_1 and T_2^* of Tumors) was used to assess the feasibility of stratifying tumors that appear to be hypoxic [146,147]. This non-invasive dynamic measurement technique used the advantage of BOLD by measuring the magnetic susceptibility changes between oxy- and deoxyhemoglobin and TOLD by measuring the shorting of tissue water T_1 due to oxygen paramagnetic characteristics.

The non-invasive measurements of tumor oxygenation in large subcutaneous Dunning R3327-AT1 prostate tumors using a 4.7T small animal magnet showed little response to inhaling oxygen during OE-MRI corresponding to previous reports [146,147]. However, the BOLD %ΔSI (n = 6, 1.3 ± 2.3%) and TOLD %ΔSI (n = 5, 1.2 ± 1.0%) responses of Group 2 (AT1-SQ) were higher compared to that previously observed (n =

3, -0.3 ± 2.0% and -0.9 ± 4.1%, respectively) [37]. This could be due to the smaller sample size and tumor volume range previously used. Hallac *et al.* [37] found positive correlations between the change in partial pressure of oxygen (ΔpO_2) and BOLD %ΔSI or TOLD %ΔSI parameters in 9 subcutaneous AT1 prostate tumors where 3 out of 9 tumors were large in volume. Importantly, I observed strong positive correlations between non-invasive measurements of BOLD %ΔSI and TOLD %ΔSI for all groups of prostate tumor models. Quantitative ΔR_1 and ΔR_2^* measurements were also used to assess the oxygenation status of the group of prostate tumors non-invasively. I found strong positive correlations between ΔR_1 and TOLD %ΔSI but the sample size (*n* = 3) was small and may not be representative of the tumor population. A moderate negative correlation was observed across the group of tumors between ΔR_2^* and BOLD %ΔSI or TOLD %ΔSI where it was previously found that the ΔR_2^* correlated well inversely with ΔpO_2 [37,98,99]. In this study, ΔR_2^* measurements (-1.6 ± 2.3 s^{-1}, *n* = 5) in orthotopic PC3 tumors were induced by inhaling oxygen as a breathing challenge. In other studies reported, ΔR_2^* measurements (-0.5 ± 1 s^{-1}, *n* = 6) were induced by the subjects inhaling carbogen with human PC3 tumors [138] implanted subcutaneously in nude mice.

The quantitative ΔR_2^* measurements suffer from local magnetic field inhomogeneity that the nuclei of the biological tissue sees typically referred to as off-resonance or phase effects that result in the loss of phase coherence of the nuclei spins. This leads to image distortion and artifacts found in the MR signals which can explain the very modest change in ΔR_2^* to inhaling oxygen. Likewise, the semi-quantitative TOLD %ΔSI suffers from magnetic field inhomogeneity in addition to lower SNR, but it has less dependency on T_2^* effects because the sequence utilizes spoiling by destroying the steady-state transverse magnetizations. Nevertheless, both imaging techniques maybe useful measurements for the orthotopic human PC3-luc tumor model since this group of

tumors was observed to respond significantly different to inhaling oxygen compared to the other groups. Consequently, given the lack of non-invasive response data available regarding orthotopic human prostate tumors, I have demonstrated that OE-MRI measurements under hyperoxic gas challenge may provide useful measurements in these tumor models for investigating tumor radiobiology non-invasively.

Non-invasive SpO_2 measurements, commonly performed in emergency departments [148-151], were used as a global validation for verifying the increase in arterial oxygen saturation during inhaling oxygen. A representative recording of arterial oxygen saturation or SpO_2 measurements is shown in Figure 4.9 (Group 1 – Tumor #1, 2.1 cm^3). The mean change in arterial oxygen saturation recorded during oxygen challenge was 4.5% (ΔSpO_2 = 92.3-87.8). A closer look at this animal's SpO_2 measurements (Figure 4.10a) clearly demonstrates a response to inhaling oxygen. Furthermore, the BOLD %ΔSI and TOLD %ΔSI responses (Figure 4.10b) in addition to the quantitative ΔR_1 and ΔR_2^* measurements were consistent responses with SpO_2 measurements at the time of oxygen challenge. The mean ΔRR showed differences in ventilation (hypoventilation or hyperventilation) among individual rats, but this difference did not significantly affect an increase in arterial oxygen concentration. For example, the respiration rate decreased by 6.0 breaths per minute in Tumor#1 from Group 1. This may be due to hypoventilation in this particular animal. Hypoventilation can occur during increase inspired oxygen concentration to counter the increase in much carbon dioxide [63]. The small mean $\Delta Temp$ of the animals during MR imaging showed stability. Temperature variation is important to monitor during MR imaging since drift could bias the OE-MRI results. As shown in Figure 4.11, the temperature measurements using the physiological monitoring system suggested temperature stability over 2 hours, typically around 36.7±0.3 ºC.
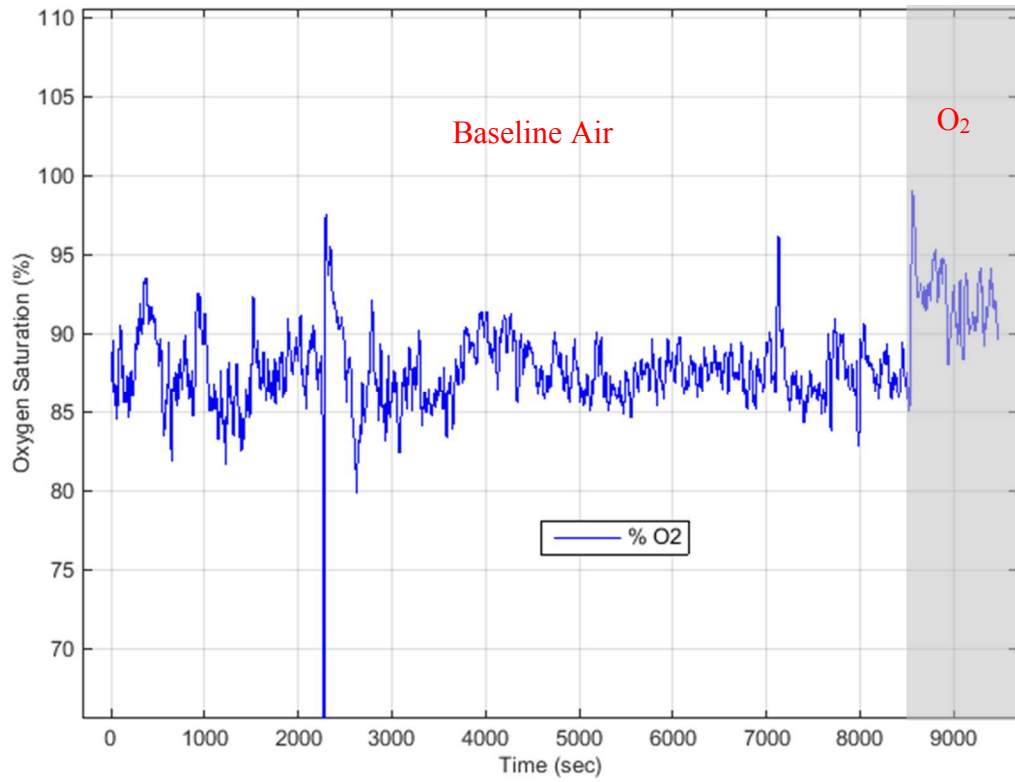
Figure 4.9 Arterial Oxygen Saturation (SpO$_2$) measurements of Tumor #1 from Group 1.

Over 2 hours SpO$_2$ was recorded while inhaling baseline air, demonstrating physiological

stability during OE-MRI. Baseline air = 87±3.3 and ΔSpO$_2$ = 5.6±-1.4.
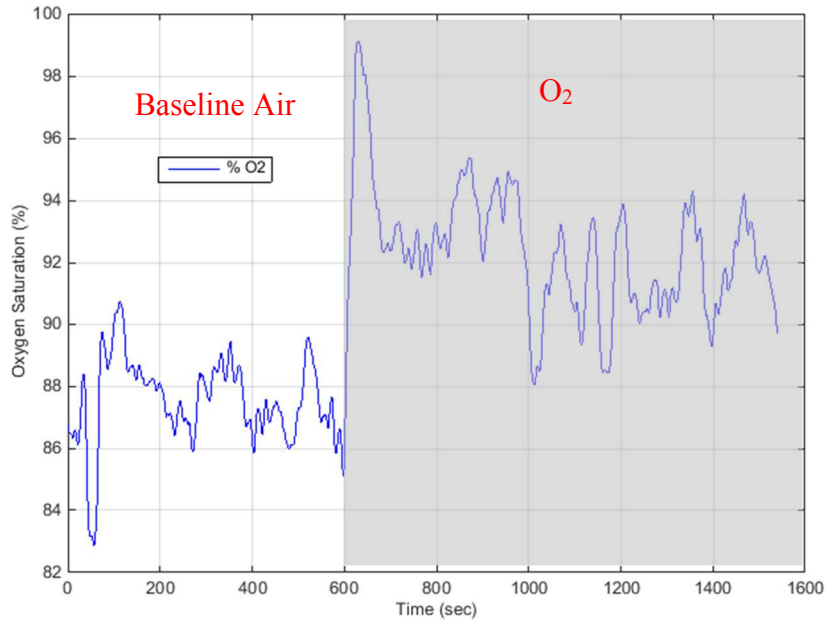
(a)
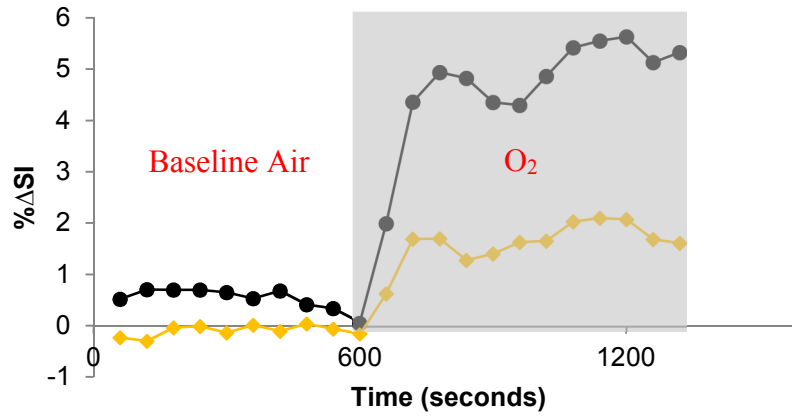
(b)

Figure 4.10 Illustration of (a) arterial oxygen saturation (SpO$_2$) measurements from Rat #1 of Group 1 and corresponding (b) dynamic BOLD %ΔSI (•) and TOLD %ΔSI (♦) signal responses to inhaling oxygen for approximately 10 minutes with respect to inhaling baseline air.
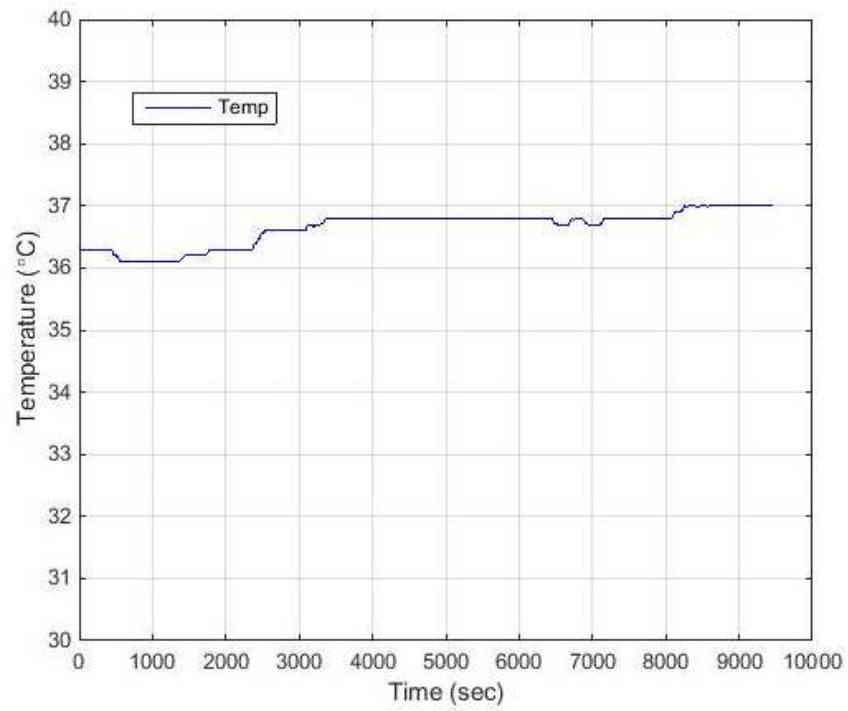
Figure 4.11 Temperature measurements of Subject #1 from Group 1. Over two (2) hours Rectal body temperature was recorded over two (2) hours while inhaling baseline air, demonstrating physiological stability during OE-MRI.

Conclusion

Inhaling oxygen influenced the MR physical parameters in AT1 and PC3 prostate tumors regardless of implantation site. In the next chapters, this influence can provide reliable results for predicting tumor growth delay. Human prostate tumors appeared to be less hypoxic compared to rat prostate tumors and may benefit when inhaling oxygen during irradiation. Potential MR prognostic biomarkers related to radiotherapy response of human prostate tumor models should be further investigated since Movsas *et al*. [27] reported that hypoxic regions do indeed exist in human prostate carcinoma. OE-MRI is a non-invasive imaging modality that can provide insight into the "apparent" oxygen status of both subcutaneous and orthotopic tumors.

Chapter 5

Evaluation of Oxygen-Enhanced Magnetic Resonance Imaging Non-Invasive Prognostic

Biomarkers for Predicting Radiation Response of Large Prostate Tumors

Abstract

Purpose

To predict the response to radiation therapy of large volume prostate tumors based on the changes of pre-irradiated Oxygen-Enhanced Magnetic Resonance Imaging (OE-MRI) non-invasive prognostic biomarkers blood-oxygen level dependent (BOLD %ΔSI), tissue-oxygen level dependent (TOLD %ΔSI), intrinsic longitudinal relaxation rate (ΔR_1), or apparent transverse relaxation rate (ΔR_2^*).

Methods

Dunning R3327-AT1 syngeneic rat prostate tumors (*n* = 8) were implanted subcutaneously in Copenhagen rats and allowed to grow ≥ 3 cm^3. OE-MRI biomarkers were measured by 4.7 T prior to radiation therapy. Subsequent to irradiation, tumor growth delay measurements were up to 2 times the irradiated tumor volume (VDT).

Results

OE-MRI biomarkers exhibited increases while inhaling oxygen. Radiation damage to gross tumor volume (GTV) was achieved. All tumors responded to treatment regardless of inhaling air or oxygen. Strong correlations were determined between BOLD %ΔSI and VDT (*R* = -0.75, *P* = 0.0315) or ΔR_1 and VDT (*R* = 0.76, *P* = 0.0274).

Conclusion

OE-MRI can confirm tumor response to inhaling oxygen. Large volume tumors received no extra growth delay benefit when inhaling oxygen during irradiation. However, OE-MRI biomarkers were used for assessing the "apparent" oxygen status in large volume

tumors. Neither OE-MRI biomarker demonstrated a significant difference to inhaling air and oxygen. This suggests that inhaling oxygen was incapable of modulating the AT1 tumor's microenvironment when the tumor size was greater than three (3) cm^3 as illustrated by the lack of tumor growth delay.

Introduction

Radiation response measurements associated with tumor hypoxia has been a topic of investigation since the early 1950's [20] which sparked several imaging methods for evaluating tumor oxygenation subsequently [48,67]. Among the many imaging methods that have been used to investigate tumor oxygenation, the determination of BOLD %ΔSI, TOLD %ΔSI, ΔR_1, or ΔR_2* appears to be the OE-MRI parameters used for assessing tumor oxygenation non-invasively [33,34,37,49,51,134-138]. Thus, the oxygenation status of solid tumors can be revealed or enhanced by hyperoxic gas challenge and the interventions regarding cancer, notably, the response to radiation therapy can be investigated. Oxygenation in tumor tissue has been explained in Chapter 4 Introduction. Nevertheless, the purpose of this study was to investigate the usefulness of OE-MRI changes from hyperoxic gas challenge for predicting the response of large prostate tumors to radiation therapy.

Methods and Materials

Ethical Statement

Refer to Chapter 3 for ethical statement.

Animals and Experimental Tumor Models

Eight (8) adult male Copenhagen rats were used as pre-clinical subjects. They were surgically implanted subcutaneously in the right flank with fresh fragments of

syngeneic Dunning R3327-AT1 prostate tumors where the AT1 is a well-characterized anaplastic prostate tumor that doubles in volume every 5.2 days, thus well-suited for radiobiological studies as previously described by others [142]. All tumor volumes were calculated using a mechanical caliper as previously described [37]. The experimental tumor models (different tumors from Chapter 4) were ready for MR imaging when they reached greater than 3 cm^3 in volume, typically around 25-30 days after implantation.

Oxygen-Enhanced Magnetic Resonance Imaging

Hyperoxic Gas Challenge

Refer to Chapter 4 for explanation on hyperoxic gas challenge.

Magnetic Resonance Imaging

The acquisition OE-MRI data and imaging protocol (Table 4.1) were described previously in Chapter 4 Methods and Material.

Radiation Therapy

Approximately 24 hours subsequent to OE-MRI experiments, the animals underwent radiation therapy. Prior to and during radiation therapy, the animals inhaled either air (*n* = 4) or 100% oxygen (*n* = 4) for at least 15 minutes. Using image-guided radiotherapy (XRAD 225Cx small animal x-ray irradiator), the gross tumor volume (GTV) of the prostate tumors was localized using superficial x-rays with a 2 mm Al added filter (energy: 40 kV; current: 0.3 mA). Radiation treatment to the GTV used orthovoltage x-rays at 1F x 15 Gy AP/PA with a 0.3 mm Cu added filter (energy: 225 kV; current; 13mA). The dose rates varied with square field sizes (20-40 mm). Subsequently, tumor growth measurements were recorded weekly over time to assess the response to radiation

damage [152]. The tumor growth delay was determined by the time (days) the tumors reached 2 times the initial irradiated tumor volume.

OE-MRI Data Analysis

All image post-processing of OE-MRI data was performed as described in the previous chapters (Chapter 2 as shown in Figures 2.22, 2.23, and 2.24 and Chapter 4 Method and Materials).

Statistical Analysis

To determine the predictive value of OE-MRI biomarkers on radiation outcome, a Pearson correlation analysis was performed using the mean of each tumor's predictive and responsive results. In addition, a comparison of the mean of each predictive and responsive results in respect to inhaling air or oxygen during irradiation was assessed using Student's t-test. A *P*-value less than 0.05 were deemed significant. All statistical analysis was evaluated using SAS 9.4 for Windows.

Results

Oxygen-Enhanced Magnetic Resonance Imaging

Individual tumor predictive OE-MRI and irradiation response values are shown in Table 5.1. OE-MRI biomarkers exhibited increases while inhaling oxygen during MR imaging. When the overall mean response values of the whole tumor ROI were considered, the semi-quantitative BOLD %ΔSI and TOLD %ΔSI responses where observed to be 1.4 ± 1.3% and 0.99 ± 1.5%, respectively. Similarly, quantitative ΔR_1 and ΔR_2* response values were observed from whole tumor ROI to be 0.0389 ± 0.0628 s^{-1} and -1.6 ± 1.25 s^{-1}, respectively.

Table 5.1 Distinctive OE-MRI Predictive and Radiation Responsive Results of Large

Dunning Prostate R3327-AT1 Prostate Tumors

AT1 Tumor	Tumor Size (cm^3)	BOLD (%ΔSI)	TOLD (%ΔSI)	ΔR_1 (s^{-1})	ΔR_2* (s^{-1})	VDT (days)
23	3.2	1.84±3.12	1.67±1.03	0.0676±0.245	0.8±36	22
24	6.6	3.05±1.15	1.69±0.98	0.0313±0.199	-1.8±60.5	23
25	3.6	0.13	2.22	0.0984	-1.0	31
26	4.9	3.81	-0.52	-0.0659	-2.2	13
Inhaled Air Mean±SD	4.6±1.5	1.8±1.5	1.2±1.2	0.038±0.071	-0.9±1.2	22±7
27	3.3	2.13 ± 1.51	-0.47±1.29	0.1350±0.143	0.6±42.3	25
28	5.7	2.5	3.4	0.0176	-1.4	14
29	4.2	0.05	-0.89	0.00938	-3.5	18
30	4.8	0.73	1.12	0.127	-2.3	27
Inhaled Oxygen Mean±SD	4.5±1.0	1.05±1.0	0.77±2	0.045±0.063	-2.3±0.91	21±6
Overall Mean±SD	4.5±1.2	1.4±1.3	0.99±1.5	0.039±0.0.063	-1.6±1.3	22±6
P-value[a,b]	0.9375[b]	0.4719[a]	0.7104[a]	0.8079[a]	0.1244[a]	0.8019[b]

a – P-values for comparisons (two-sample t-tests) of each covariate for differences in inhaling air vs. oxygen.
b – P-values for comparisons (two-sample t-tests) in differences in inhaling air vs. oxygen initial or VDT volumes.
VDT: time the tumors reached 2 times the initial irradiated tumor volume;
BOLD: blood-oxygen level dependent; TOLD: tissue-oxygen level dependent; ΔR_1 : intrinsic longitudinal relaxation rate; ΔR_2*: apparent transverse relaxation rate

     Representative dynamic BOLD %ΔSI or TOLD %ΔSI responses of three large representative prostate tumors are illustrated in Figure 5.1. Two rats had similar tumor sizes and inhaled air (Figure 5.1a, AT1 tumor #23) or oxygen (Figure 5.1c, AT1 tumor #27) during irradiation. A rat with a larger tumor (Figure 5.1b, AT1 tumor #24) also inhaled air during irradiation. During OE-MRI, as shown in Figure 5.1, the dynamic BOLD or TOLD signals variously showed positive or negative impulse responses to inhaling oxygen for at least 10 minutes. The AT1 tumor shown in Figure 5.1a had a stable baseline before responding to inhaling oxygen. Whereas, the baseline for the AT1 tumor shown in Figure 5.1b was less stable but responded well to inhaling oxygen. On the

other hand, the baseline for AT1 tumor shown in Figure 5.1c was very chaotic and this tumor did not respond well to inhaling oxygen.
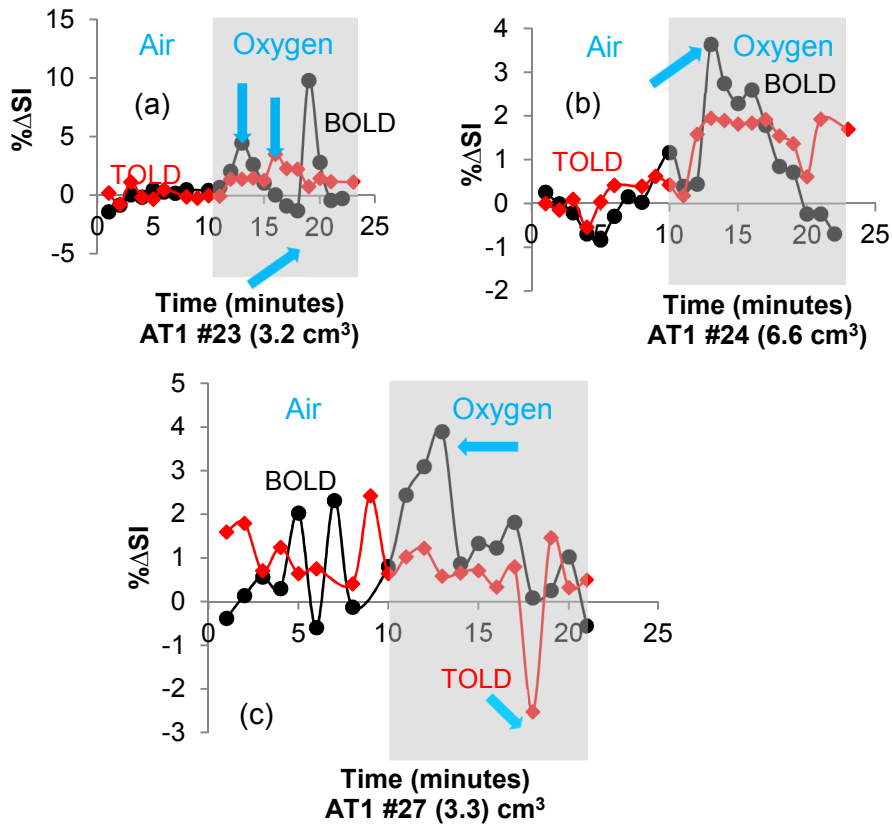
Figure 5.1   Representative OE-MRI of dynamic BOLD and TOLD signal responses to inhaling oxygen for approximately 10 minutes with respect to inhaling baseline air. Pre-irradiated mean whole tumor ROI BOLD %ΔSI (black •) and TOLD %ΔSI (red ♦) of tumors with approximately the same size at the time of inhaling (a,b) air or (c) oxygen during irradiation. Arrows illustrates positive or negative impulse responses to inhaling oxygen.

Raw images and example voxel fitting results of R_1 and $R_2{}^*$ values from Tumor #23 are shown in Figure 5.2 and Figure 5.3. The fitting results demonstrated good quality based on the determination of coefficient ($R^2 > 0.95$). OE-MRI response maps are illustrated in Figure 5.4. All the OE-MRI response maps demonstrated distinct tumor heterogeneity. The BOLD %ΔSI or TOLD %ΔSI response maps showed extensive of tumor heterogeneity where the greatest amount of signals tend to be around the periphery of the tumor. The threshold ΔR_1, and $\Delta R_2{}^*$ response maps showed similar heterogeneity. However, the best curve fit for calculating the ΔR_1 values seem to concentrate mainly toward the tumor area adjacent to the thigh muscle of the animal. A visual comparison regarding $\Delta R_2{}^*$ with the ΔR_1 shows greater variation throughout the whole tumor but the best curve fit $\Delta R_2{}^*$ values seem to concentrate mainly toward the front tip of the tumor.

Comparing the mean of each tumor's predictive responses with respect to inhaling air or oxygen during irradiation was assessed. The size of the initial irradiated tumor volume ($P_{\text{Tumor Size}} = 0.9375$) or the pre-irradiated OE-MRI predictive responses ($P_{\text{BOLD \%}\Delta\text{SI}} = 0.4719$, $P_{\text{TOLD \%}\Delta\text{SI}} = 0.7104$, $P_{\Delta R1} = 0.8079$, or $P_{\Delta R2^*} = 0.1244$) for those inhaling air or oxygen during irradiation were not significantly different. After OE-MRI experiments or on the day of irradiation, the overall mean initial irradiated tumor volume was observed to be approximately 4.54 ± 1.20 cm^3 for the large prostate tumors.
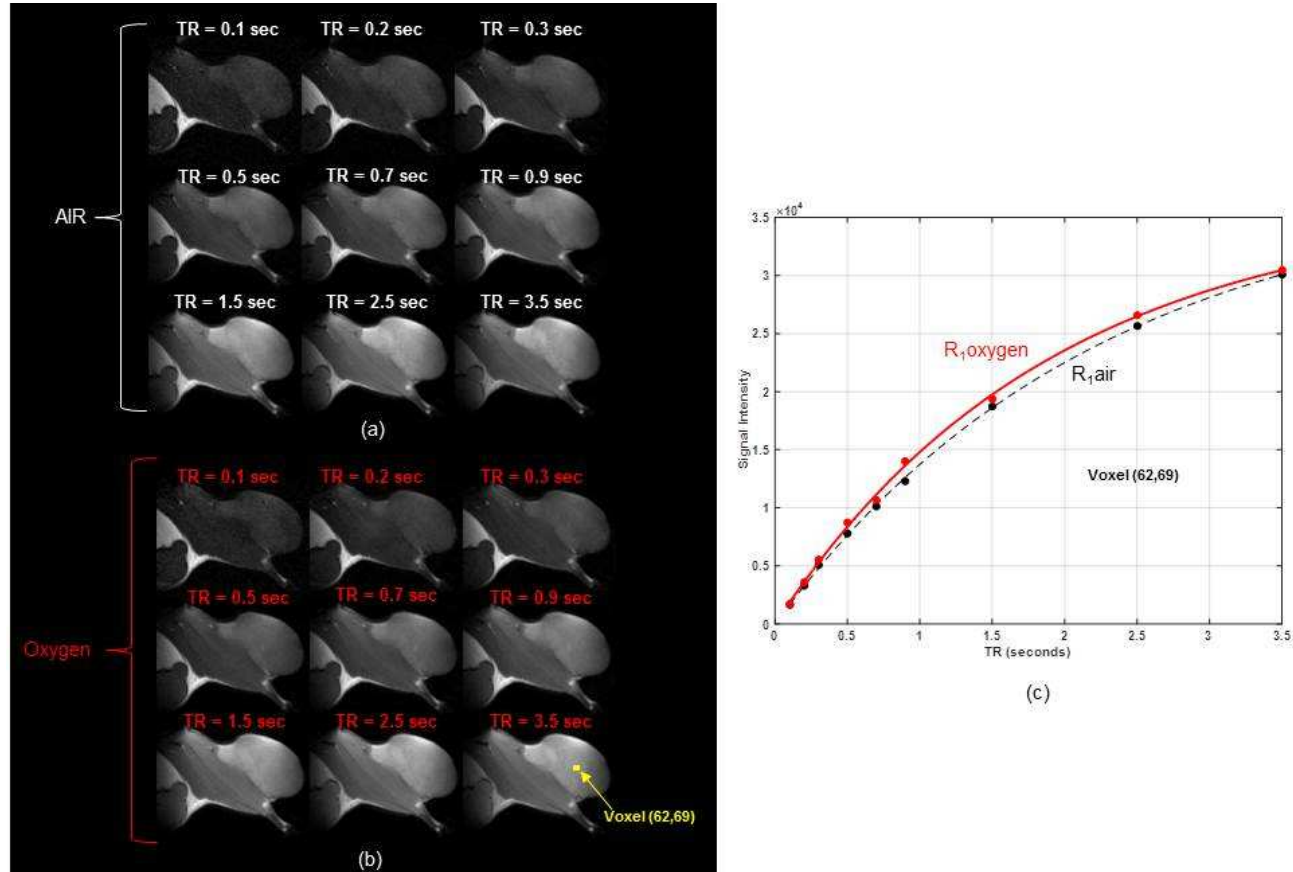
Figure 5.2 Raw T_1 and PD weighted images and quality of R_1 fitting. Images acquired from Tumor #23 while the rat was inhaling (a) air and (b) oxygen. (c) Relaxation rate curve fittings of tumor voxel (62, 69) as a function of repetition time while the rat inhaled air and oxygen ($R^2 > 0.99$).
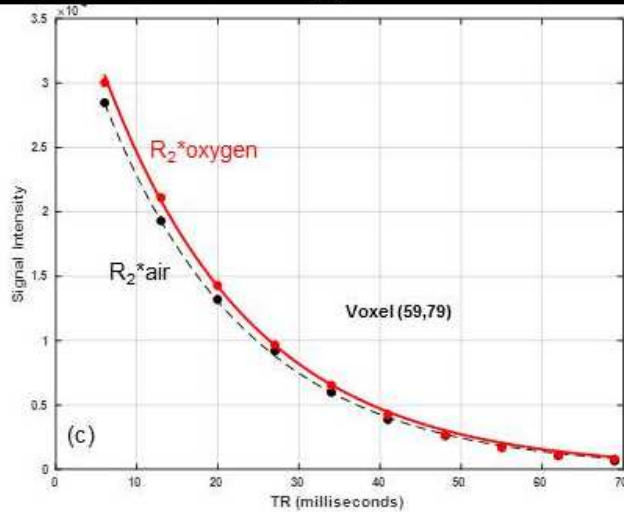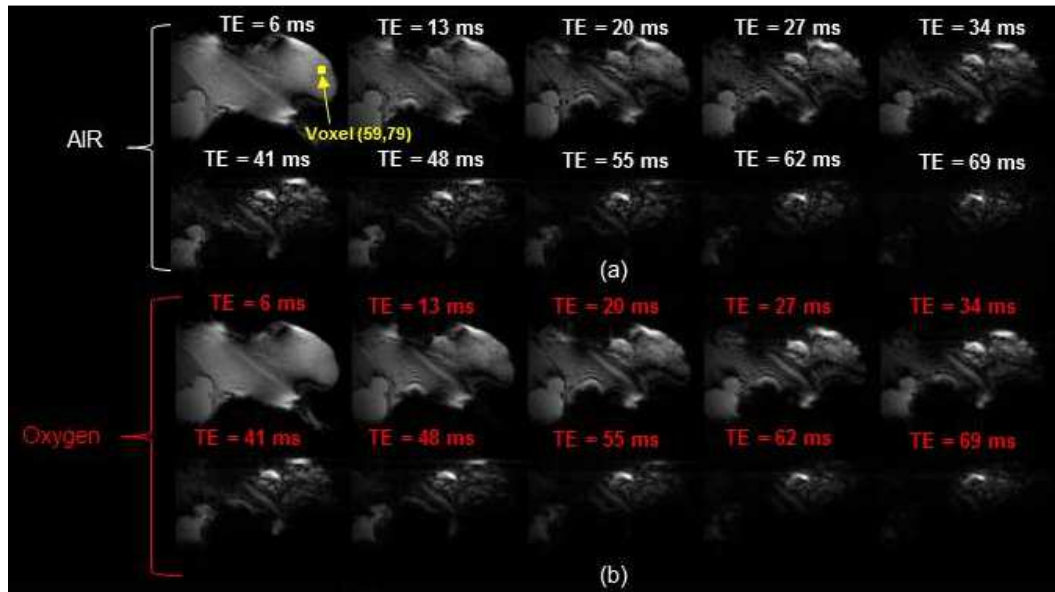
Figure 5.3 Raw T_2^* weighted images and quality of R_2^* fitting. Images from BOLD acquisition (same Tumor #23 from Figure 5.2) while the rat was inhaling (a) air and (b) oxygen. (c) Relaxation rate curve fittings of tumor voxel (59, 79) as a function of repetition time while the rat inhaled air and oxygen ($R^2 > 0.99$).

104
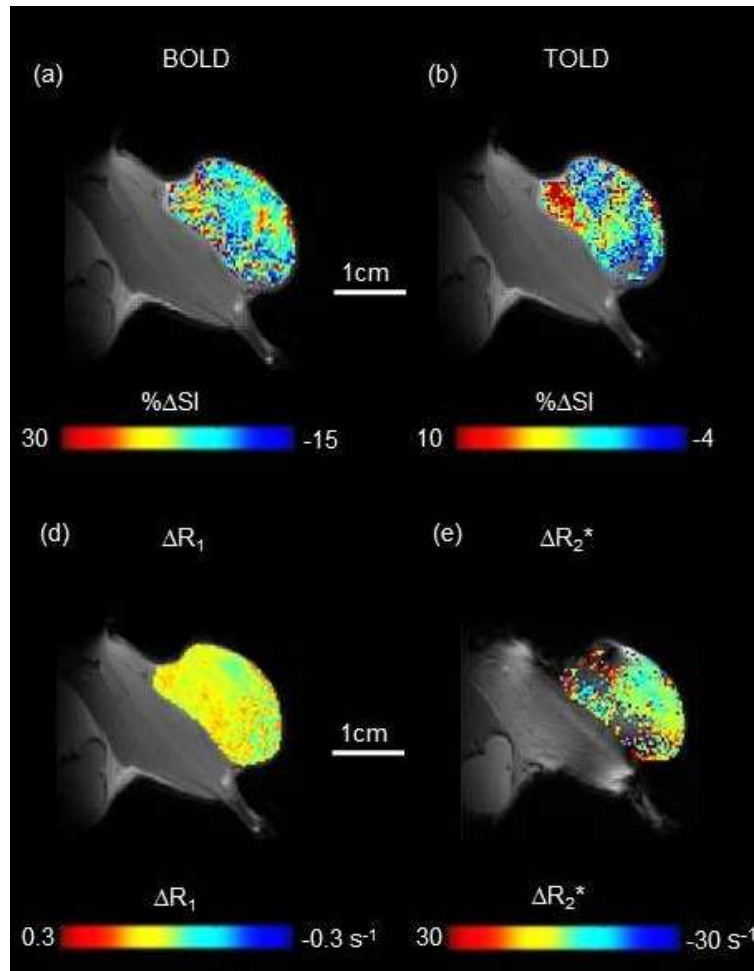
Figure 5.4 Oxygen-Enhanced MRI. BOLD %ΔSI, TOLD %ΔSI, ΔR_1, and ΔR_2* response maps for a large Dunning prostate R3327-AT1 prostate tumor (# 23, 3.2 cc). The BOLD %ΔSI and TOLD %ΔSI response maps are shown on high-resolution PD-weighted image with respect to inhaling (a,b) oxygen at 13 and 16 minutes, respectively, during the experiment (see Figure 5.1(a) for reference). The ΔR_1 (on high-resolution T_1-weighted image) and ΔR_2* (on high-resolution T_2*-weighted image) response maps are the differences between the mean baseline air and oxygen (c,d).

105

Radiation Therapy

In general, all tumors responded to irradiation regardless of inhaling air or oxygen. Following irradiation, tumor volume was measured until the tumors reached 2 times the irradiated tumor volume (VDT). As shown in Figure 5.5, there was significant tumor growth delay for the large prostate tumors (21.6 ± 6.3 days) compared to control (8.8 ± 1.5 days). Radiation response (P_{VDT} = 0.8019) showed no significant difference between tumors in rats breathing air or oxygen. However, moderate significant (or approaching significant) correlations were observed between pre-irradiated BOLD %ΔSI and VDT (R = -0.74, P = 0.0355) or pre-irradiated ΔR_1 and VDT (R = 0.70, P = 0.0532) overall for the eight animals inhaling either air or oxygen during irradiation (Figure 5.6). Counterintuitively, prostate AT1 tumors #26 and #28 were found to have relatively higher pre-irradiated BOLD %ΔSI responses, but lower ΔR_1 responses compared to other tumors. Despite their higher pre-irradiated BOLD %ΔSI responses, these large prostate tumors were found to grow relatively faster after irradiation although the rat (tumor #26) inhaled air and the rat (tumor #28) inhaled oxygen during irradiation. No significant correlation was observed between the other pre-irradiated OE-MRI biomarkers (TOLD %ΔSI or ΔR_2*) and VDT.
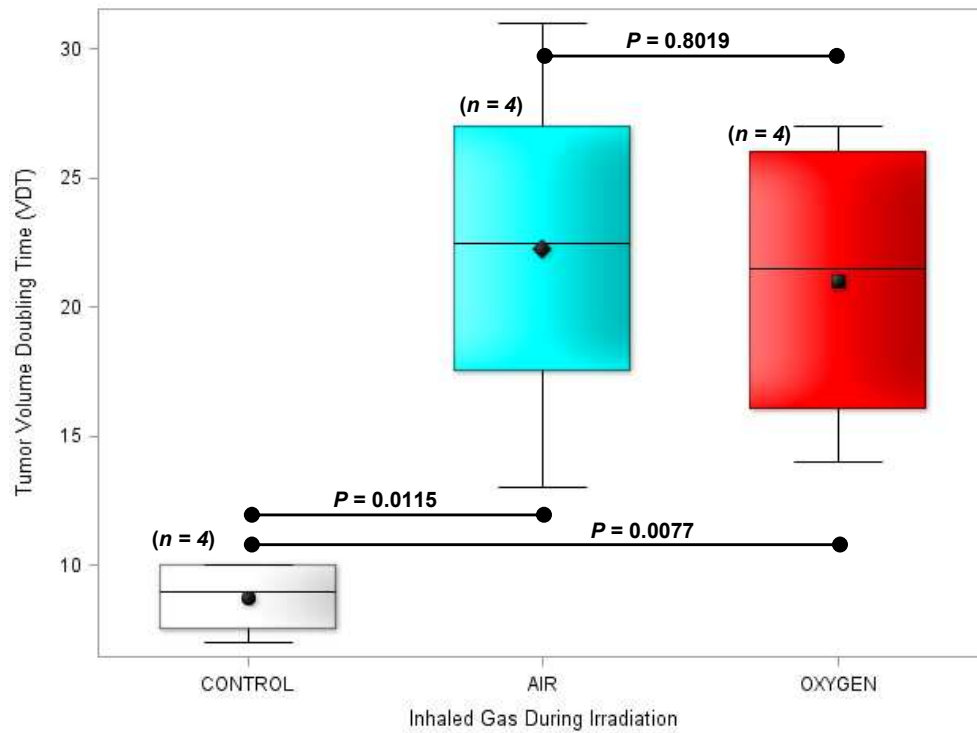
Figure 5.5 An array of response on Dunning R3327-AT1 large prostate tumors to a dose of 30 Gy. Mean tumor growth measurements (VDT in days) for animals inhaling air (n = 4, black ♦), where the predictive pre-irradiated response values seem to be slightly higher compared to the animals inhaling oxygen (n = 4, black ■) during irradiation and no benefit to inhaling oxygen during irradiation was observed similar to previously observed [145].
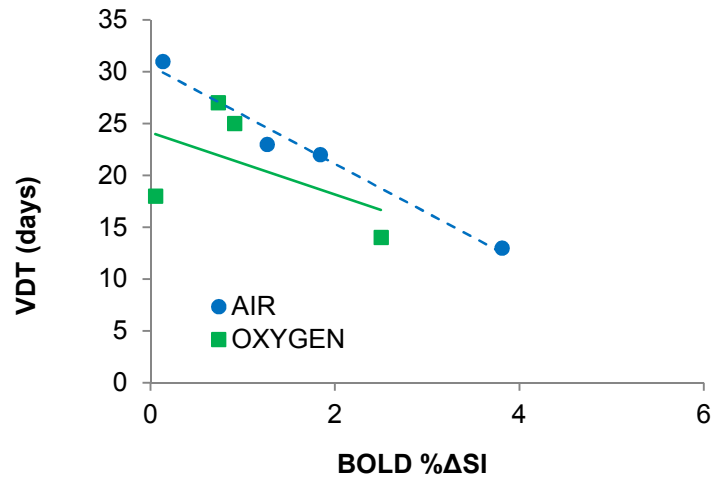
(a)
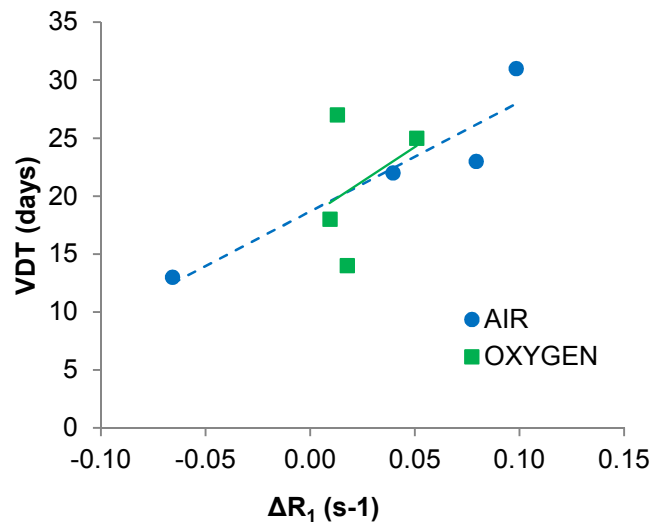
(b)

Figure 5.6 Correlation between pre-irradiated OE-MRI values and tumor growth delay or the effect of inhaling air (n = 4, blue circles) or oxygen (n = 4, green squares) on tumor radiation response observed as 2 times the initial irradiated tumor volume (VDT).

Discussion

The assessment of tumor oxygenation status before irradiation is an important consideration for predicting tumor response non-invasively. It is assumed that better oxygenated tumors would respond to radiation and help delay tumor regrowth. If determined that tumor hypoxic cells can become oxygenated before irradiation, an effective prognosis can be customized. All large prostate tumors exhibited significant tumor heterogeneity which may have affected the response to radiation damage. When inhaling air or oxygen during irradiation, there was no difference in radiation response to a single dose of 30 Gy in these large volume tumors at the time of irradiation. Consequently, no benefit in tumor growth delay was observed despite breathing air or oxygen.

In a previous investigation [145], the overall mean size of the tumor volume (n = 10, 3.85 ± 0.65 cm^3) used to predict tumor growth delay in response to a single dose of 30 Gy was approximately 15% smaller than the mean tumor size (n = 8, 4.54 ± 1.20 cm^3) used in this study. The response to radiation of small and large subcutaneous Dunning R3327-AT1 prostate tumors was assessed [145] using an *in vivo* minimally invasive quantitative dynamic sample technique called FREDOM [46] which was used to assess the oxygenation status of tumors. Bourke *et al*. [145] observed in their group of large volume prostate tumors a mixture of well oxygenated with a mean partial pressure of oxygen (pO_2) greater than 10 mm Hg and poorly oxygenated tumors that responded to irradiation very differently depending on the pO_2 status of the tumors. In addition, strong correlations were found between the tumor pO_2 and the tumor volume doubling time (VDT). It was also observed that the VDT of the large prostate tumors reached approximately 12 days after irradiation where in this study the VDT reached approximately 22 days. Additionally, the benefit to inhaling air or oxygen during

irradiation for the group of large AT1 tumors was not distinguished similar to what we have observed. The so-called DOCENT (Dynamic Oxygen Challenge Evaluated by NMR T_1 and T_2^* of Tumors) were evaluated to assess the utility of stratifying tumors that appear to be hypoxic [146,147]. This non-invasive dynamic measurement technique used the advantage of BOLD by measuring the magnetic susceptibility changes between oxy- and deoxyhemoglobin and TOLD by measuring the shorting of tissue water T_1 due to oxygen paramagnetic characteristics. Implementing these measurements has the potential for rapid clinical implementation.

The non-invasive measurements of tumor oxygenation in large Dunning R3327-AT1 prostate tumors using a 4.7T small animal magnet showed little response to inhaling oxygen during OE-MRI corresponding to previous reports [146,147]. However, the overall semi-quantitative pre-irradiated BOLD $\%\Delta SI$ (n = 8, 1.34 ± 1.26%) and TOLD $\%\Delta SI$ (n = 8, 0.939 ± 1.50%) responses were higher compared to that previously reported (n = 3, -0.3 ± 2.0% and -0.9 ± 4.1%, respectively) [37]. Hallac et al. [37] found correlations between the change in partial pressure of oxygen (ΔpO_2) and BOLD or TOLD parameters in 9 subcutaneous AT1 prostate tumors where 3 out of 9 tumors were large in volume. In addition, this previous non-invasive investigation reported that the pre-irradiated BOLD $\%\Delta SI$ response was not found to correlate with radiation response (time for tumor to quadruple in size or VQT) where the TOLD $\%\Delta SI$ response was more significant for stratification. On the other hand, I found the opposite case for these large prostate tumors in regard to VDT and stratification by illustrating the importance of combining non-invasive measurements of BOLD and TOLD for identifying the status of a tumor's vascular extent and hypoxia, respectively [37].

Quantitative ΔR_1 and ΔR_2^* measurements were also used as pre-irradiated OE-MRI biomarkers to assess the oxygenation status and radiation response of the large

110

prostate tumors non-invasively. A strong linear trend was observed between ΔR_1 and VDT suggesting a promising stratification regardless of inhaling air or oxygen during irradiation (Figure 5.4b) in line with that previous reported [145] using minimally invasive tumor pO_2 as a pre-irradiated predictor. Additionally, Hallac *et al*. [37] non-invasively found a direct linear relationship between ΔR_1 and VQT for those tumors irradiated while inhaling 100% oxygen (n = 6). As reported previously, no correlation was observed between $\Delta R_2{}^*$ and VDT. Quantitative $\Delta R_2{}^*$ measurements suffers from local magnetic field inhomogeneity that the nuclei of the biological tissue sees typically referred to as off-resonance or phase effects that results to the loss of phase coherence of the nuclei spins. This leads to image distortion and artifacts found in the MR signals which can explain the very modest change in $\Delta R_2{}^*$ to inhaling oxygen. Chapter 4 large AT1-SQ tumors (n = 6, 3.9 ± 0.9 cm^3) were nearly the same size as the tumors in this chapter (n = 8, 4.5 ± 1.2 cm^3) but correlations of OE-MRI were not observed in both chapters.

Conclusion

Indeed, the oxygenation status in tumors has been shown to influence MR physical parameters and shown to provide reliable results for predicting tumor growth delay in a vast amount of radiobiological studies. OE-MRI is a non-invasive imaging modality that can provide insight to the "apparent" oxygen status of tumors where multi-parametric measurements must be considered when stratifying patient in the clinic. However, the large AT1 prostate tumors investigated received no extra benefit when the rats inhaled oxygen during irradiation compared to the rats inhaling air which may suggest that inhaling oxygen was incapable of modulating the AT1 tumor's microenvironment when the tumor size is greater than 3 cm^3 as illustrated by the lack of tumor growth delay.

Chapter 6

Prostate Tumor Prognostic Factors in Split-Dose Irradiation: Predicting the Outcome

Non-invasively using Oxygen-Enhanced Magnetic Resonance Imaging

Abstract

Purpose

To investigate the usefulness of Oxygen-Enhanced Magnetic Resonance Imaging (OE-MRI) non-invasive predictive measurements blood-oxygen level dependent (BOLD %ΔSI), tissue-oxygen level dependent (TOLD %ΔSI), intrinsic longitudinal relaxation rate (ΔR_1), or apparent transverse relaxation rate (ΔR_2^*) for a prognostic determination to inhaling oxygen during hypofractionation.

Materials and Methods

Dunning R3327-AT1 syngeneic rat prostate tumors (*n = 30*) were implanted subcutaneously in adult male rats and allowed to grow (0.67-2.1 cm^3). OE-MRI parameters were measured by 4.7 T small animal magnet each time prior to irradiation with 2F x 7.5 Gy AP/PA to gross tumor volume (GTV). Radiation response was assessed by tumor growth delay measurements as measured up to 4 times the initial irradiated tumor volume (VQT in days) while inhaling air or oxygen. Survival estimates from VQT were assessed using Kaplan-Meier. The outcome of split-dose irradiation in 18 tumors was used to identify individual OE-MRI parameters, and combinations thereof, associated with VQT by using multivariate linear regression analysis. Six (6) equations from results of the multivariate regression were validated from another eight (8) tumors and the mean square error (MSE), the mean absolute percentage error prediction (MAPE), and the mean squared prediction error (MSPE) were used to evaluate the predictive accuracy.

Results

OE-MRI parameters exhibited responses to inhaling oxygen. Immunohistochemistry confirmed tumor response to inhaling oxygen and tumor reoxygenation as demonstrated by OE-MRI. Inhaling oxygen during hypofractionation significantly improved response to treatment based on survival probability estimates ($P < 0.0001$, log-rank test). The OE-MRI parameters determined to have the highest predictive accuracy (MAPE = 9%) for those rats inhaling air was $d\Delta R_1$. For rats inhaling oxygen, the OE-MRI parameters with the highest predictive accuracy (MAPE = 19%) were mean TOLD, pre2F O_2 challenge R_1, and mean ΔR_1.

Conclusion

Inhaling oxygen during irradiation was a prognostic factor. Increased tumor oxygenation after the first fraction of dose suggested reoxygenation which is a prognostic factor. OE-MRI parameters formed the basis for predicting tumor response to hypofractionation, suggesting potential patient stratification and personalized radiotherapy treatment planning.

Statement of Translation Relevance

This investigation demonstrates the usefulness of Oxygen-Enhanced Magnetic Resonance Imaging (OE-MRI) for prognostic determination of prostate tumor response to radiotherapy. OE-MRI utilizes molecular oxygen as an endogenous contrast agent for non-invasive imaging measurements of tumor response to inhaling oxygen. The response to inhaling oxygen has the potential of modifying tumor hypoxia and consequently the response to radiation as opposed to inhaling air during irradiation. When observing the OE-MRI responses of tumor oxygenation before each radiation

fraction, I was able to predict the outcome of tumor growth delay using a Kaplan-Meier survival analysis. This investigation provides a rationale for considering tumor oxygenation in future personalized radiotherapy treatment planning.

Introduction

Unfortunately, many patients still present advanced local disease and require aggressive radiotherapy. One reason is tumor hypoxia which plays a fundamental role in resistance [30] mainly because tumors are spatially and temporally heterogeneous which limits the efficacy of radiation damage to the tumor. Thus, uniform tumor radiation dosage may simply be less effective compared to non-uniform intensity dose distributions. Intensity-modulated radiation therapy (IMRT) is capable of delivering different dose distributions spatially to multiple targets with high intensity dose gradients; thus, customizing the treatment by conforming to the target's conditions. However, pertinent biological imaging information such as tumor hypoxia is needed to guide this type of "dose paintings" and, hitherto, there has been no satisfactory approach to assessing hypoxia non-invasively to allow more effective treatment planning [153].

Oxygen-Enhanced MRI (OE-MRI) encompassing blood-oxygen level dependent (BOLD), tissue-oxygen level dependent (TOLD), and quantitative relaxation (R_1 and R_2^*) methods is expected to provide insights into tumor hypoxia and could serve as a non-invasive prognostic biomarker for predicting radiation response. A comparison against change in partial pressure of oxygen (ΔpO_2) measurements obtained from the Fluorocarbon Relaxometry using Echo planar imaging for Dynamic Oxygen Mapping (FREDOM) was tested against these parameters and found to correlate [37].

Significant effort to correlate the ΔpO_2 measurements (or other indirect imaging biomarker associated with the ΔpO_2) to a response to treatment with tumor growth delay

as a surrogate end point have been notable. However, the prognostic determination of tumor oxygenation after definitive radiotherapy remains unclear. Measurements of increased tumor growth after single-dose irradiation [25,37,145,154] while inhaling air has been associated with decreased tumor radiosensitivity. Lower tumor pO_2 compared to the response of tumors with higher tumor pO_2 and stratification based on tumor types, sizes, and hypoxia have been reported [25,37,145,154]. Measuring tumor pO_2 and stratifying based on tumor sizes and hypoxia during the course of split-dose irradiation were accomplished by O'Hara *et al.* [155] but there still remains a need to identify practical significant prognostic factors.

In this investigation, I non-invasively measured and assessed pre-irradiated and between fraction tumor ΔpO_2 indirectly using OE-MRI parameters. I evaluated tumor growth as a surrogate end point from split-dose hypofractionation to identify the prognostic factors that may influence the response to radiotherapy in a well-characterized prostate tumor model. It is important to note that the effect of tumor ΔpO_2 on the outcome may be continuous and not change in a stepwise fashion; thus, identification of an ideal outcome cut-off value of a response or no response may be difficult. Consequently, the experimental data from this investigation was used in the development and validation of a multivariate regression model in predicting outcome from split-dose hypofractionation.

Methods and Materials

Ethical Statement

Refer to Chapter 3 for ethical statement.

Animals and Experimental Tumor Models

Thirty (30) adult male Copenhagen rats were used as pre-clinical subjects. They were surgically implanted subcutaneously in the right flank with fresh fragments of syngeneic Dunning R3327-AT1 prostate tumors where the AT1 is a well-characterized anaplastic prostate tumor that doubles in volume every 5.2 days, thus well-suited for radiobiological studies as previously described by others [142,156,157] with a Gleason score in the range of 8-10 [158]. All tumor volumes were calculated using a mechanical caliper as previously described [37]. The experimental tumor models were ready for OE-MRI when they reached greater than 0.5 cm^3 in volume, typically around 19 days after implantation. Animals where divided into a unirradated control group (Group1, *n = 4*), irradiated while inhaling air (Group 2, *n = 13*), irradiated while inhaling oxygen (Group 3, *n = 13*, and histology & immunohistochemistry (Group 4, *n = 3*).

Oxygen-Enhanced Magnetic Resonance Imaging

Hyperoxic Gas Challenge

The acquisition OE-MRI data and imaging protocol (Table 4.1) were described previously in Chapter 4 Methods and Material.

Magnetic Resonance Imaging

OE-MRI data and imaging protocol (Table 4.1) were described previously in Chapter 4 Methods and Material. However, I repeated OE-MRI 7 days later.

Radiation Therapy

Approximately 24 hours subsequent to OE-MRI experiments as described previously in Chapter 5 Methods and Material with slight modifications. Briefly, prior to and during radiotherapy, rats inhaled either air (*n* = 13) or oxygen (*n* = 13) for at least 15

minutes. Unirradated tumors (n = 4) were used as controls. Radiation treatment to the GTV used orthovoltage x-rays at 2F x 7.5 Gy AP/PA with a 0.3 mm Cu added filter (energy: 225 kV; current; 13mA). The dose rates varied with square field sizes (20-40 mm). Using data points from tumor growth curves of each animal, the tumor growth delay was determined by the time (days) the tumors reached 4 times the initial irradiated tumor volume (VQT in days) as illustrated by the following simple linear interpolation equation:

$$\frac{(T_A - T_B)}{(V_A - V_B)} = \frac{(T_A - VQT)}{(V_A - 4V_0)} \qquad (6.1)$$

where V_0, T_A, V_A, and V_B represent the measured initial irradiated tumor volume (cm^3), resulting time (days) above 4 x V_0, the volume (cm^3) measured above 4 x V_0, and the volume (cm^3) measured below 4 x V_0, respectively, as determined from the tumor growth curves. Simplifying gives VQT as:

$$VQT = T_A - \frac{(T_A - T_B)}{(V_A - V_B)}(V_A - 4V_0) \qquad (6.2)$$

Three additional tumors (n = 3) were added to this investigation to assess reoxygenation after the first fraction of dose (1F x 7.5 Gy AP/PA) only.

Histology and Immunohistochemistry

A double hypoxia marker approach [159-161] was used to verify tumor reoxygenation. Immediately after OE-MRI, three (3) tumors were injected intravenously with a baseline tumor hypoxia maker pimonidazole HCl (Hydroprobe™-1, Hypoxyprobe,

Inc., Burlington, MA, USA. 60 mg/kg body weight) dissolved in saline while breathing oxygen. Approximately 24 hours subsequent to OE-MRI, two (2) tumors were irradiated with 1F x 7.5 Gy AP/PA while inhaling oxygen where one (1) tumor remained as a control. Approximately 72 hours later, subsequent to measurements of OE-MRI, the second tumor hypoxic marker CCI-103F (Hydroprobe™-F6, Hypoxyprobe, Inc., Burlington, MA, USA. 60 mg/kg body weight) dissolved in 90% peanut oil and 10% dimethyl sulfoxide was injected intraperitoneally. Approximately ninety (90) minutes later, the tumor blood perfusion marker Hoechst 33342 dye (Invitrogen, Eugene, Oregon, USA, 10 mg/kg) dissolved in saline was injected intravenously, respectively. Within one (1) minute, the rats were sacrificed and tumor tissue specimens were harvested directly in liquid nitrogen and formalin until processed for visualizing immunohistochemical (IHC) and hematoxylin & eosin (H&E) staining. All three (3) rats were inhaling oxygen throughout H&E and IHC.

OE-MRI Data Processing and Analysis

OE-MRI data processing and analysis was performed as described in the previous chapters (Chapter 2 as shown in Figures 2.22, 2.23, and 2.24 and Chapter 4 Method and Materials). Voxel-by-voxel correlation coefficients of BOLD or TOLD responses in prostate tumor's ROI were determined against a BOLD or TOLD average time response vector with each voxel to identify changes in signal intensity. The BOLD average 3rd echo from slices was used for image analysis. Normalized correlation coefficient maps [162,163] were threshold by making inferences on the correlation coefficient values to identify the locations of strong correlations distributed within the voxels. The threshold of the normalized values of the correlation coefficients provided

confidence of the spatial distribution of oxygen within the tumor ROI at the time of the MR scanning. Appendix B provides addition explanation of correlation coefficient mapping.

Statistical Analysis

All pre-irradiated OE-MRI values before the first and second fraction of dose (pre1F and pre2F) from the split-dose group were distributed normally as demonstrated by univariate analysis. A two-way unbalanced general linear model (GLM) was used to evaluate differences in mean OE-MRI values for inhaling air or oxygen. In addition, a comparison of the mean of each tumor's predictive and responsive results was assessed using two-sample t-test. In the analysis of radiation response, observed posttherapy tumor growth events in response to inhaling air or oxygen compared to the control group were assessed by log-rank test Kaplan-Meier analysis [164]. To initiate an assessment of the predictive value of OE-MRI parameters (Table 6.1) on radiation outcome, a Pearson correlation matrix of response variables was assessed which provided the coefficient of simple correlation (*R*-value) between VQT and the pre1F and pre2F (or combinations, thereof) OE-MRI variables in a scattered plot matrix. The experimental data was split into two parts with an approximate ratio size of two-thirds (2/3) and one-third (1/3) based on the date of OE-MRI scan. Earlier dated scans provided the top 2/3. The 2/3 part (model development data) was used for developing a multivariate linear regression model and fitted to estimate the tumor response as a function of the prognostic factors. The prognostic factors were retained on the basis a stepwise selection procedure [165,166] by adding and removing variables from the model one-by-one to determine an optimal subset of OE-MRI parameters and parameter estimates. An OE-MRI parameter was added if the *F* statistic when added was significant at *P* = 0.25. After adding a variable, the stepwise selection procedure, however, removed

variables already in the model if the *F* statistic was not significant at *P* = 0.05. The 1/3 part (validation data) was used for validating the model and the mean square error (MSE), the mean absolute percentage error prediction (MAPE), and the mean squared prediction error (MSPE) were used to evaluate the predictive accuracy [165,167-169]. The MPE, MAPE, and MSPE were calculated as follows:

$$\text{MPE} = \frac{1}{n}\sum_{i=1}^{n}\left(\frac{\text{actual VQT(i)} - \text{predicted VQT(i)}}{\text{actual VQT(i)}} \times 100\right) \tag{6.3}$$

$$\text{MAPE} = \frac{1}{n}\sum_{i=1}^{n}\left|\frac{\text{actual VQT(i)} - \text{predicted VQT(i)}}{\text{actual VQT(i)}} \times 100\right| \tag{6.4}$$

$$\text{MSPE} = E\left[\sum_{i=1}^{n}(\text{actual VQT(i)} - \text{predicted VQT(i)})^{2}\right] \tag{6.5}$$

where n is the number of validation samples and *E* is the expected value. The MPE [167,168] measured the tendency of the model to underestimate (positive value) or overestimate (negative) VQT, the MAPE [167-170] measured the accuracy of the predictor, and the MSPE [165,167] measured the quality of the multivariate linear regression model compared to the model's error mean square (MSE). The criteria for evaluating and selecting [170] a validated model is shown in Table 6.2. The most accurate model will have a MAPE close to zero [170]. A *P*-value less than 0.05 was

deemed significant. All statistical analysis was evaluated using SAS 9.4 Windows version.

Table 6.1 OE-MRI Predictive Parameters

Parameter	Code Name	Description
1	V0_1F	Tumor volume before 1st dose fraction
2	V0_2F	Tumor volume before 2nd dose fraction
3	V30_1F	Tumor volume 30 days after 1st dose fraction
4	V30_2F	Tumor volume 30 days after 2nd dose fraction
5	SHRINKAGE	Tumor shrunk after 1st dose fraction No = 0, Yes = 1
6	REOXY	IBT signals increased after 1st dose fraction No = 0, Yes = 1
7	BOLD_1F	Percent change in BOLD signal intensity before 1st dose fraction
8	BOLD_2F	Percent change in BOLD signal intensity before 2nd dose fraction
9	BOLD_AVG	Average of 1st and 2nd BOLD signal intensities
10	TOLD_1F	Percent change in TOLD signal intensity before 1st dose fraction
11	TOLD_2F	Percent change in TOLD signal intensity before 2nd dose fraction
12	TOLD_AVG	Average of 1st and 2nd TOLD signal intensities
13	R1_BL1F	Baseline R_1 relaxation rate before 1st dose fraction
14	R1_OX1F	Oxygen R_1 relaxation rate before 1st dose fraction
15	CHANGE_R1_1F	Change in R_1 relaxation rate before 1st dose fraction
16	R1_BL2F	Baseline R_1 relaxation rate before 2nd dose fraction
17	R1_OX2F	Oxygen R_1 relaxation rate before 2nd dose fraction
18	CHANGE_R1_2F	Change in R_1 relaxation rate before 2nd dose fraction
19	CHANGE_R1_AVG	Average of 1st and 2nd change in R_1 relaxation rates
20	R2STAR_BL1F	Baseline R_2* relaxation rate before 1st dose fraction
21	R2STAR_OX1F	Oxygen R_2* relaxation rate before 1st dose fraction
22	CHANGE_R2STAR_1F	Change in R_2* relaxation rate before 1st dose fraction
23	R2STAR_BL2F	Baseline R_2* relaxation rate before 2nd dose fraction
24	R2STAR_OX2F	Oxygen R_2* relaxation rate before 2nd dose fraction
25	CHANGE_R2STAR_2F	Change in R_2* relaxation rate before 2nd dose fraction
26	CHANGE_R2STAR_AVG	Average of 1st and 2nd change in R_2* relaxation rates
27	dBOLD	Difference between 2nd and 1st BOLD signal intensities
28	dTOLD	Difference between 2nd and 1st TOLD signal intensities
29	dR1	Difference between 2nd and 1st change in R_1 relaxation rates
30	dR1BASELINE	Difference between 2nd and 1st baseline R_1 relaxation rates
31	dR1CHALLENGE	Difference between 2nd and 1st challenge R_1 relaxation rates
32	dR2STAR	Difference between 2nd and 1st change in R_2* relaxation rates
33	dR2STARBASELINE	Difference between 2nd and 1st baseline R_2* relaxation rates
34	dR2STARCHALLENGE	Difference between 2nd and 1st challenge R_2* relaxation rates

Table 6.2 Evaluation and Selection Criteria for Validated Model

using MAPE (Table adapted from Wei *et al*. [170])

MAPE (%)	Assessment
< 10	Highly accurate forecasting
10-20	Good forecasting
20-50	Reasonable forecasting
> 50	Inaccurate forecasting

Results

Oxygen-Enhanced Magnetic Resonance Imaging

The observed physiological parameters during air and oxygen breathing during MR imaging are shown in Table 6.3. After the first fraction of dose, the change in respiration rate (ΔRR) decreased when compared to the previous measurement a week earlier. Temperature (ΔTemp) remained nearly unchanged whereas there was a decrease in the response in arterial oxygen saturation (ΔSpO_2) after the first fraction of dose. As mentioned in Chapter 4, temperature variation is important to monitor during MR imaging because temperature drift can bias the OE-MRI results. Nevertheless, the number of tumor measurements, averages (means), and standard deviations of the OE-MRI and irradiated responses separated by inhaling air and oxygen are shown in Table 6.4 and Table 6.5, respectively. Twenty-six (26) animals underwent split-dose irradiation subsequent to OE-MRI measurements. The model data used for developing a multivariate regression model was from eighteen (18) animals from Table 6.4 and Table 6.5. I added eight (8) additional animals for validation only (Table 6.6). In general, the OE-MRI and irradiated response values showed distinctive results regardless of tumor volume. Overall, the OE-MRI values demonstrated increased responses after inhaling oxygen during MR imaging. These responses illustrated the potential for modifying hypoxia before irradiation. No significant responses were observed to oxygen breathing except for the pre2F quantitative ΔR_2* values from split-dose hypofractionation ($P_{\Delta R2\text{*-pre2F}}$ = 0.0271) which may indicate that this measurement parameter can detect changes in the tumor microenvironment in regards to oxygen concentration after the first fraction of dose. Representative voxel-by-voxel quantitative ΔR_2* response maps of pre1F (field-of-view (FOV) = 40 x 40) and pre2F (FOV = 60 x 60) for an AT1 prostate tumor (Figure 6.1d, AT1 tumor #43) inhaling oxygen during irradiation showed an slight increase in R_2*

at the tumor ROI. Nevertheless, pre-irradiated TOLD %ΔSI (P = 0.1144) appeared to be approaching significance also in addition to the quantitative ΔR_2^* response. Figure 6.1 shows significant tumor heterogeneity in all OE-MRI responses.

Table 6.3 Physiological Parameters Results

AT1 Tumor	Tumor Size (cc)		Δ Respiration Rate (Breath/min)		ΔTemperature (°C)		ΔSpO$_2$ (%O2 Saturation)	
	pre1F	pre2F	pre1F	pre2F	pre1F	pre2F	pre1F	pre2F
31	1.02	2.65	-	-	-	-	-	-
32	0.94	1.59	-3.38	-6.70	-0.56	-1.46	-	-
33	0.92	1.21	-	-	-	-	-	-
34	1.22	2.26	-	-1.05	-	-0.20	-	6.09
35	1.22	2.48	-4.51	-2.37	0.34	-0.13	-	-
36	1.41	2.20	-	-	-	-0.55	-	-
37	2.07	3.07	-	-2.58	0	-0.31	-	7.62
38	0.88	0.99	-7.74	-20.1	-0.14	-0.21	-	4.64
39	1.21	1.96	0.62	-1.22	0	-0.39	13.3	5.2
49	1.33	2.21	-8.69	-2.62	-0.05	0.08	-	-
50	0.98	2.02	-5.83	-0.08	-0.08	-0.16	-	16.2
51	0.87	1.71	-	-	-0.23	-	0.98	-
52	2.09	4.48	-4.92	-	-0.003	-	-	-
Inhaled Air Mean±SD	1.2± 0.41	2.2± 0.88	-3.9± 4.1	-3.3± 7.3	-0.04± 0.26	-0.29± 0.49	7.1± 8.7	6.8± 5.0
40	1.48	1.72	-3.95	-	-0.38	-	-	-
41	1.08	1.66	-	-	-	-	-	-
42	0.67	1.06	-	-	-	-	-	-
43	0.93	0.87	-	-	-	-	-	-
44	1.15	2.52	-	-	-	-	-	-
45	1.14	0.94	-	-	-	-	-	-
46	1.64	2.73	-2.26	-2.54	-1.95	-0.11	7.73	4.48
47	1.74	2.58	-4.18	-5.60	0.14	-0.12	5.80	3.62
48	1.67	3.06	-2.46	-4.88	-0.39	-0.25	9.73	7.31
53	1.04	2.25	-0.44	-12.1	0.00	0.00	-	-
54	1.14	2.72	-3.19	-2.64	0.00	0.00	-	-
55	0.85	1.91	-1.81	-16.7	-0.33	-0.23	-	-
56	1.15	2.36	-0.44	-	0.08	-	-	-
Inhaled Oxygen Mean±SD	1.2± 0.33	2.0± 0.73	-2.0± 1.7	-6.1± 6.2	-0.21± 0.76	-0.09± 0.12	6.3± 3.3	4.3± 2.3
Overall Mean±SD	1.2± 0.4	2.1± 0.8	-2.9± 3	-4.5± 7	-0.12± 0.6	-0.21± 0.4	6.59± 5	5.8± 5

Table 6.4 Dunning R3327-AT1 Prostate Tumor Characteristics and Split-Dose Hypofractionation Results (Air Group)

AT1 Tumor	Tumor Size[a] (cc)		BOLD (%ΔSI)		TOLD (%ΔSI)		ΔR_1 (s^{-1})		ΔR_2^* (s^{-1})		VDT[a] (days)	VQT[a] (days)
	pre1F	pre2F	pre1F	pre2F	pre1F	pre2F	pre1F	pre2F	pre1F	pre2F		
31	1.02	2.65	-2.10± 1.80	2.36± 1.70	-0.40± 0.70	2.25± 1.30	0.0539± 0.0973	-	5.1± 57.8	1.3± 32.5	19	25
32	0.94	1.59	3.62± 0.95	2.59± 0.75	2.13± 0.80	1.65± 0.45	0.0475± 0.1491	-	0.3± 44.4	-1.7± 30.8	18	28
33	0.92	1.21	-0.60± 1.56	5.18± 1.31	-0.19± 0.51	1.34± 1.94	0.0928± 0.1097	0.0567± 0.1135	-3.5± 49.4	2.6± 40.6	21	26
34	1.22	2.26	4.09± 3.79	-0.33± 0.81	2.51± 0.58	-0.46± 0.22	0.0374± 0.0845	0.0313± 0.0810	-0.8± 50.5	0.9± 35.1	17	33
35	1.22	2.48	2.43± 1.37	1.86± 0.82	0.79± 0.11	1.00± 0.41	0.0149± 0.00716	0.0142± 0.1573	9.1± 40.3	-0.1± 22.2	7	28
36	1.41	2.20	4.01± 0.86	3.01± 1.12	1.05± 0.79	1.53± 0.36	0.0099± 0.1644	0.0139± 0.1618	-0.3± 30.7	-0.1± 47.4	23	39
37	2.07	3.07	-0.44± 0.64	0.73± 0.42	0.59± 0.28	0.98± 0.42	-0.006± 0.00980	0.0326± 0.1617	-0.4± 23.8	-0.3± 18.2	31	49
38	0.88	0.99	3.76± 1.55	3.86± 2.13	2.11± 0.73	2.24± 0.77	0.0365± 0.0986	0.0252± 0.0643	0.6± 51.8	0.6± 37.2	13	26
39	1.21	1.96	3.29± 1.14	2.28± 0.67	0.72± 1.39	1.59± 0.99	0.0472± 0.1673	0.0070± 0.1074	-0.6± 25.4	0.3± 22.1	10	25
Inhaled Air Mean±SD	1.1± 0.4	2.1± 0.7	2.0± 2.4	2.4± 1.6	1.0± 1.0	1.3± 0.8	0.037± 0.029	0.026± 0.017	1.1± 4	0.4± 1	18± 7	32± 8

Data values reported as mean ± standard deviation (SD) from voxels averaged over two slices for BOLD, TOLD, and R_2^* and three slices for R_1.
a – P-values for comparisons (general linear analysis) in differences of initial, VDT, or VQT tumor volumes vs. control tumor volumes (not shown in table).
VDT: time the tumors reached 2 times the initial irradiated tumor volume; VQT: time the tumors reached 4 times the initial irradiated tumor volume
BOLD: blood-oxygenation level dependent ; TOLD: tissue-oxygenation level dependent; ΔR_1 : intrinsic longitudinal relaxation rate; ΔR_2^*: apparent transverse relaxation rate

Table 6.5 Dunning R3327-AT1 Prostate Tumor Characteristics and Split-Dose Hypofractionation Results (Oxygen Group)

AT1 Tumor	Tumor Size[a] (cc)		BOLD (%ΔSI)		TOLD (%ΔSI)		ΔR_1 (s^{-1})		ΔR_2^* (s^{-1})		VDT[a] (days)	VQT[a] (days)
	pre1F	pre2F	pre1F	pre2F	pre1F	pre2F	pre1F	pre2F	pre1F	pre2F		
40	1.48	1.72	-0.93± 1.83	2.52± 1.32	0.32± 0.51	1.62± 0.66	0.0460± 0.1326	-	-1± 47.2	-3.2± 29.4	28	39
41	1.08	1.66	-3.26± 2.06	3.29± 1.39	1.07± 0.43	1.63± 0.42	0.1213± 0.1260	0.0070± 0.1351	2.1± 33.3	-0.3± 32.1	24	30
42	0.67	1.06	1.43± 0.67	0.61± 0.91	0.76± 0.38	1.19± 0.38	0.0393± 0.1032	0.0460± 0.1495	1.7± 43.4	1± 36.5	23	32
43	0.93	0.87	4.52± 2.33	4.77± 1.56	1.97± 0.46	1.72± 0.60	0.0677± 0.2091	0.0015± 0.2230	-1± 33.9	0.3± 51.2	31	43
44	1.15	2.52	3.55± 3.78	3.24± 1.10	0.77± 0.70	2.53± 0.55	0.0520± 0.2036	0.0601± 0.2314	-1.5± 42.6	-0.3± 32.5	25	40
45	1.14	0.94	7.94± 1.97	2.22± 1.15	1.40± 0.81	1.68± 0.49	0.0308± 0.2587	0.0730± 0.1397	-3.3± 38.6	-2.4± 29.4	28	36
46	1.64	2.73	1.64± 0.67	2.50± 1.07	1.25± 0.37	1.57± 0.37	0.0310± 0.0717	0.0136± 0.1338	-0.8± 29.3	-2.3± 21.3	30	42
47	1.74	2.58	2.60± 1.47	3.43± 1.39	1.03± 0.56	3.00± 1.37	0.0011± 0.1392	0.0085± 0.1234	5.4± 29.2	-3.3± 26.2	28	48
48	1.67	3.06	4.77± 1.58	3.47± 1.26	1.51± 0.34	2.13± 0.49	0.0069± 0.0660	0.0161± 0.0844	-1.2± 40.3	-0.5± 26.1	37	42
Inhaled Oxygen Mean±SD	1.3± 0.4	1.9± 0.8	2.5± 3.3	2.9± 1.1	1.1± 0.5	1.9± 0.6	0.044± 0.036	0.028± 0.027	0.04± 2.3	-1.2± 1.6	28± 4.2	39± 5.6
Overall Mean±SD	1.2± 0.4	2.0± 0.7	2.2± 2.8	2.6± 1.4	1.1± 0.8	1.6± 0.7	0.041± 0.032	0.027± 0.022	0.55± 3.2	-0.42± 1.6	20.± 9	32± 11
P-value[b]	0.7093	0.7160	0.7351	0.4576	0.8241	0.1144	0.6570	0.8449	0.5155	0.0271	0.0006	0.0356
P-value[c,a]	0.4235, 0.5799		0.9822		0.4242		0.7071		0.7353		<0.0001	<0.0001

Data values reported as mean ± standard deviation (SD) from voxels averaged over two slices for BOLD, TOLD, and R_2^* and three slices for R_1.
a – P-values for comparisons (general linear analysis) in differences of initial, VDT, or VQT tumor volumes vs. control tumor volumes (not shown in table).
b – P-values for comparisons (two-sample t-tests) of each covariate for differences in inhaling air vs. oxygen.
c – P-values for comparisons (two-sample t-tests) of each covariate for differences in pre1F- vs. pre2F controlled treatment groups (inhaling air vs. oxygen).
VDT: time the tumors reached 2 times the initial irradiated tumor volume; VQT: time the tumors reached 4 times the initial irradiated tumor volume
BOLD: blood-oxygenation level dependent ; TOLD: tissue-oxygenation level dependent; ΔR_1 : intrinsic longitudinal relaxation rate; ΔR_2^*: apparent transverse relaxation rate

Table 6.6 Dunning R3327-AT1 Prostate Tumor Characteristics and Split-Dose Hypofractionation Results (Validation Data)

AT1 Tumor	Tumor Size (cc)		BOLD (%ΔSI)		TOLD (%ΔSI)		ΔR_1 (s^{-1})		ΔR_2^* (s^{-1})		VDT (days)	VQT (days)
	pre1F	pre2F	pre1F	pre2F	pre1F	pre2F	pre1F	pre2F	pre1F	pre2F		
49	1.33	2.21	1.81± 0.48	1.28± 0.77	1.22± 0.29	3.36± 0.51	0.0118± 0.1187	0.0255± 0.1332	-0.7± 50.5	1.1± 68.7	13	37
50	0.98	2.02	0.07± 1.22	4.90± 2.49	1.99± 0.70	5.57± 2.10	0.0032± 0.0880	0.0212± 0.0944	-0.1± 35.2	5.2± 35.2	16	41
51	0.87	1.71	-	10.6± 2.67	-	6.40± 1.40	-0.0278± 0.1067	0.0496± 0.1396	-	-4.6± 35.9	7	80
52	2.09	4.48	2.75± 2.88	5.72± 1.30	1.85± 1.81	3.02± 0.95	0.0138± 0.1653	0.0273± 0.1005	-4.9± 54.7	4.3± 58.2	4	40
Inhaled Air Mean±SD	1.3± 0.6	2.6± 1.3	1.6± 1.4	5.6± 3.9	1.7± 0.4	4.6± 1.7	0.0003± 0.019	0.031± 0.013	-1.9± 3.0	1.5± 4.4	10± 6	50± 20
53	1.04	2.25	6.27± 1.71	4.49± 1.24	4.63± 0.52	2.53± 2.76	-0.0003± 0.1481	0.0384± 0.1010	-5.5± 47.4	-7.8± 31.6	6	50
54	1.14	2.72	5.29± 1.30	4.10± 1.33	2.69± 0.68	3.43± 0.98	0.0390± 0.1531	0.0581± 0.1531	-3.0± 50.2	-0.2± 41.8	5	46
55	0.85	1.91	2.59± 0.60	6.28± 4.92	2.08± 1.10	1.23± 3.30	0.0147± 0.1012	0.0314± 0.1404	-2.9± 46.7	-4.8± 30.6	4	56
56	1.15	2.36	2.70± 0.98	6.13± 1.36	1.31± 0.73	3.65± 0.59	0.0375± 0.1144	0.0135± 0.1134	-2.0± 46.7	-2.9± 26.2	7	33
Inhaled Oxygen Mean±SD	1.1± 0.14	2.3± 0.33	4.2± 1.9	5.3± 1.1	2.7± 1.4	2.7± 1.1	0.023± 0.019	0.035± 0.018	-3.4± 1.5	-3.9± 3.2	6± 1	46± 10
Overall Mean±SD	1.2± 0.4	2.5± 0.9	3.1± 2.1	5.4± 2.6	2.3± 1.2	3.7± 1.6	0.012± 0.021	0.033± 0.015	2.7± 2.0	-1.2± 4.6	8± 4	48± 15
P-value	0.3747	0.6683	0.0914	0.8546	0.3015	0.1078	0.1473	0.7049	0.3910	0.0943	0.1609	0.7834

Data values reported as mean ± standard deviation (SD) from voxels averaged over two slices for BOLD, TOLD, and R_2^* and three slices for R_1.

P-values for comparisons (two-sample t-tests) of each covariate for differences in inhaling air vs. oxygen.

VDT: time the tumors reached 2 times the initial irradiated tumor volume; VQT: time the tumors reached 4 times the initial irradiated tumor volume

BOLD: blood-oxygenation level dependent ; TOLD: tissue-oxygenation level dependent; ΔR_1 : intrinsic longitudinal relaxation rate; ΔR_2^*: apparent transverse relaxation rate
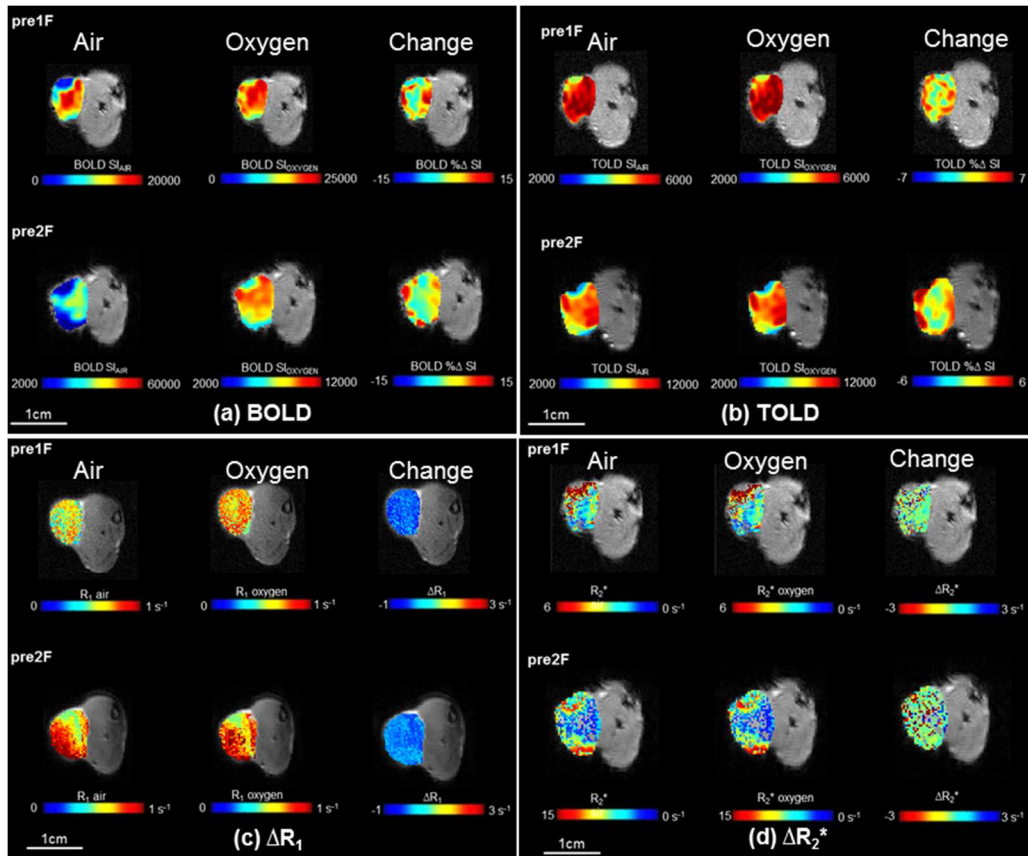
Figure 6.1 Oxygen-Enhanced MRI. Small AT1 prostate tumor (AT1 tumor #43, 0.93 cm^3) on rat inhaling oxygen during irradiation. Semi-quantitative (a) BOLD %ΔSI or (b) TOLD %ΔSI response maps at pre1F and pre2F. Quantitative (c) ΔR_1 and (d) ΔR_2* response maps at pre1F and pre2F. Significant tumor heterogeneity is shown.

Radiation Therapy

All tumors responded to radiation regardless of inhaling air or oxygen. The time for the initial irradiated tumor volume was determined by measurements until the tumors reached 4 times the irradiated tumor volume. The tumors from split-dose hypofractionation (model development data, *n = 18)* demonstrated significant differences between the VDT (*P* = 0.0006) and the VQT (*P* = 0.0356) among the irradiated gas breathing groups in addition to highly significant difference compared to the control group (*n = 4, P* < 0.0001). The tumor growth curve for the split-dose group is illustrated in Figure 6.2 and demonstrated the effect of tumors inhaling air and oxygen compared to the control tumors as assessed by the VQT (Figure 6.3). In regards to the observed radiation responses, the log rank test shown in Figure 6.4 (adjusting for five (1 air and 4 oxygen) censored [171] observations due to rats dying due to other causes) demonstrated that there were significant differences among the irradiation gas breathing event time distributions. I observed many significant correlations associated with the VQT. It was determined that those rats inhaling air or oxygen mostly had the same predictive factors that significantly correlated with VQT (Table 6.7). The group of independent covariates (*P* ≤ 0.25) [172] may or may not be included during model development and validation, but a fairly weak relationship may turn out to be significant depending on the sample size. For example, the animals inhaling oxygen demonstrated a weak correlation between the 1st ΔR_2* and VQT (*R* = -0.46, *P* = 0.2124) which seemed to be approaching significance and with additional samples investigated may turn out to be significant. Nevertheless, there was an interesting strong correlation (animals inhaling air) with the difference between the 2nd and 1st ΔR_1 measurements (dΔR_1) and VQT (*R* = 0.9395, *P* = 0.0017) indicating reoxygenation (Figure 6.5a) and a moderate correlation

between pre2F TOLD and VQT (R = 0.6949, P = 0.0378, Figure 6.5b) for those animals inhaling oxygen.

It is important to note that when the independent variables are highly correlated with one another it can produce severe errors in computations of the X'X matrix when inverted for estimating the regression coefficients called multicollinearity [165]. Considering a threshold R-value greater than 0.70 ($|R| \geq 0.70$), the independent variable among themselves may be associated with multicollinearity. Consequently, the results of stepwise multivariate linear regression (Table 6.7) retained the factors that were deemed significant to explain the outcome of tumor growth delay. The validation of the selected regression model was the final step in the model building process [165]. An independent test data set (Table 6.6) was used for checking the selected multivariate linear regression model. The selected model from Table 6.5 was re-estimated with the validation data and the mean squared prediction error (MSPE) of the validation case was compared with the error mean square (MSE) of the model development case as shown in Table 6.6. For Equations 6.6-6.11, the multivariate linear regression models for air and oxygen breathing groups are based on the results of a stepwise selection procedure since it was determined that these groups were significantly different (Figure 6.3). An evaluation of the air model, which seems to increase in predictive ability, showed that Equation 6.8 had the strongest ability to predict VQT since the MSE = 11.2 (n = 7) $\gg$ MSPE= 2.5 (n = 4). Based on the results of using SAS for the validation of the air model, the MPE and MAPE were 3.3% and 9.0%, respectively, and deemed to be the best model. The validating results of the oxygen multivariate linear regression model had much larger values so the best model would be Equation 6.9 but this model may not have predictive ability.

As shown in Table 6.4 and Table 6.5, the non-invasive OE-MRI measurements demonstrated either an increase in values or remained the same after the first fraction of

dose suggesting tumor reoxygenation and illustrated in Figures 6.6a-d. The IBT correlation coefficient maps and histogram (Figure 6.6b and 6.6d) illustrated increased tumor oxygenation after the first fraction of dose as demonstrated by the increased number of modulated voxels. Furthermore, tumors showed a greater TOLD signal response to oxygen breathing one week after the 1st radiation dose, which was significant for the tumors on rats breathing oxygen (P = 0.0061, Figure 6.7).

The radiotherapy community compares the quality of different fractionation regimens using the biologically effective dose (BED = $(nd)\left[1 + \dfrac{d}{\alpha/\beta}\right]$) [59], where n is the number of fractions, d (Gy) is the delivered dose, and the α/β (Gy) represents tumor radiosensitivity parameters for early- and late-responding tissues. I assumed the ratio of α/β = 6.8 Gy according to previous findings on R3327-AT1 rat prostate tumors [173]. I compared the VQT data from Hallac et al. [37] investigation using single-dose to my split-dose VQT (Figure 6.8).   I found a combined weak significant correlation between the BED and VQT (R = 0.3799, P = 0.0433) for those animals inhaling air and oxygen suggesting the higher the BED used for irradiating the AT1 tumor a longer tumor growth delay will result. Also, based on a t-test comparison there was a significant difference to inhaling air (n = 14) compared to inhaling oxygen (n = 15, P = 0.0457) during irradiation suggesting that inhaling oxygen during irradiation may provide an additional benefit regardless of the BED.

Histology and Immunohistochemistry

For proof-of-principal, immunohistochemistry (Figure 6.9 and Figure 6.10) confirmed tumor reoxygenation (n = 2) when irradiated with 1F x 7.5 Gy AP/PA compared to an unirradiated tumor (n = 1). Most of the hypoxic areas disappeared approximately

72 hours in the irradiated tumors (HF_{pimo} = 0.0968 ± 0.0150, $HF_{CCI-103F}$ = 0.0026 ± 0.0036) where the unirradiated tumor hypoxic areas remained nearly the same (HF_{pimo} = 0.2768, $HF_{CCI-103F}$ = 0.2757) with no irradiation.
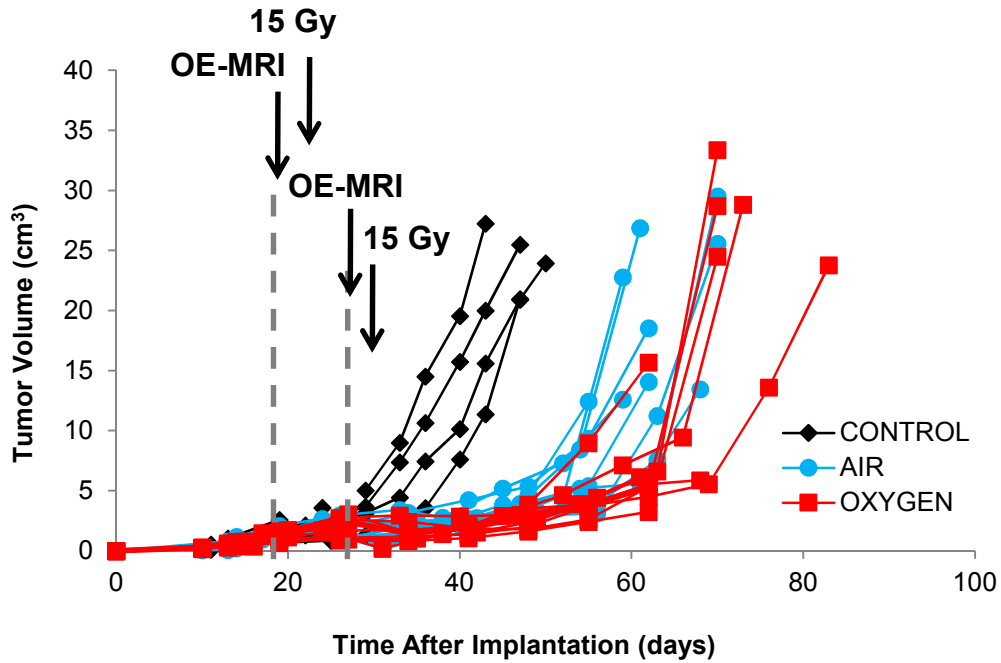
Figure 6.2 Tumor growth curves for 22 individual Dunning prostate R3327-AT1 tumors of unirradiated tumors (n = 4, black filled diamonds), irradiated inhaling air (n = 9, cyan filled circles), and irradiated inhaling oxygen (n = 9, red filled squares) demonstrating an array of responses to a split-dose schedule of 2F x 7.5 Gy AP/PA at seven (7) days apart.
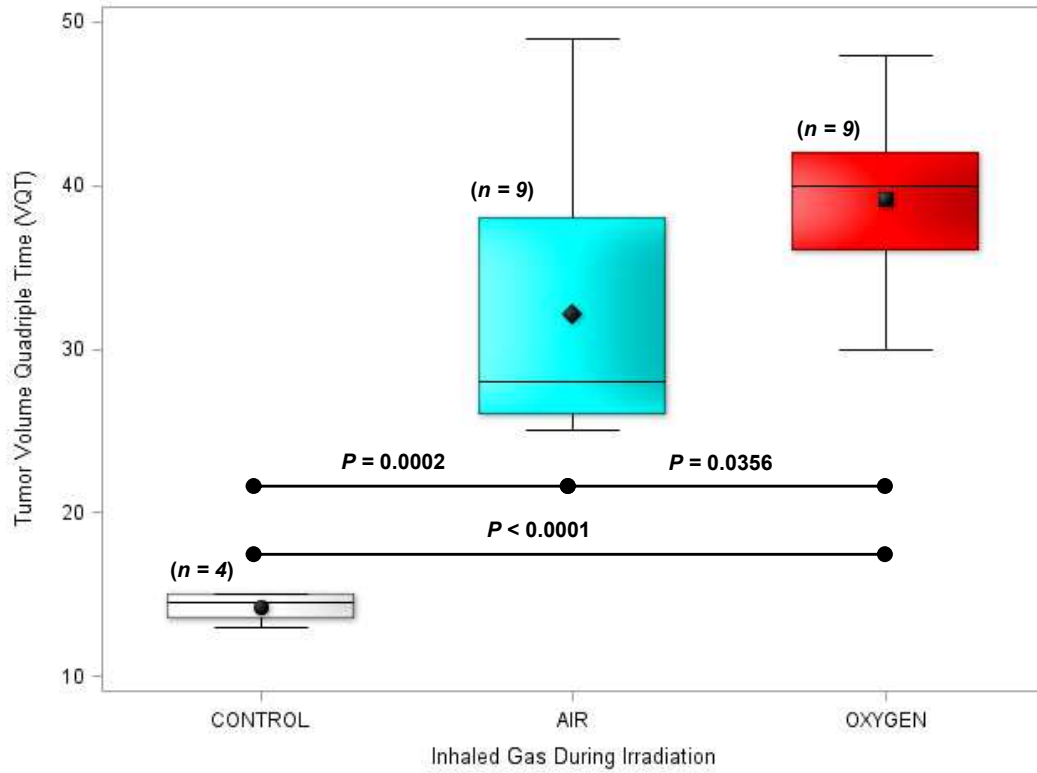
Figure 6.3 Box plots of mean tumor growth measurements (VQT in days) for animals with unirradiated tumors (n = 4, black ●), inhaling air (n = 9, black ♦), and inhaling oxygen (n = 9, black ■) during irradiation showed significant difference across irradiated breathing treatments suggesting stratification.
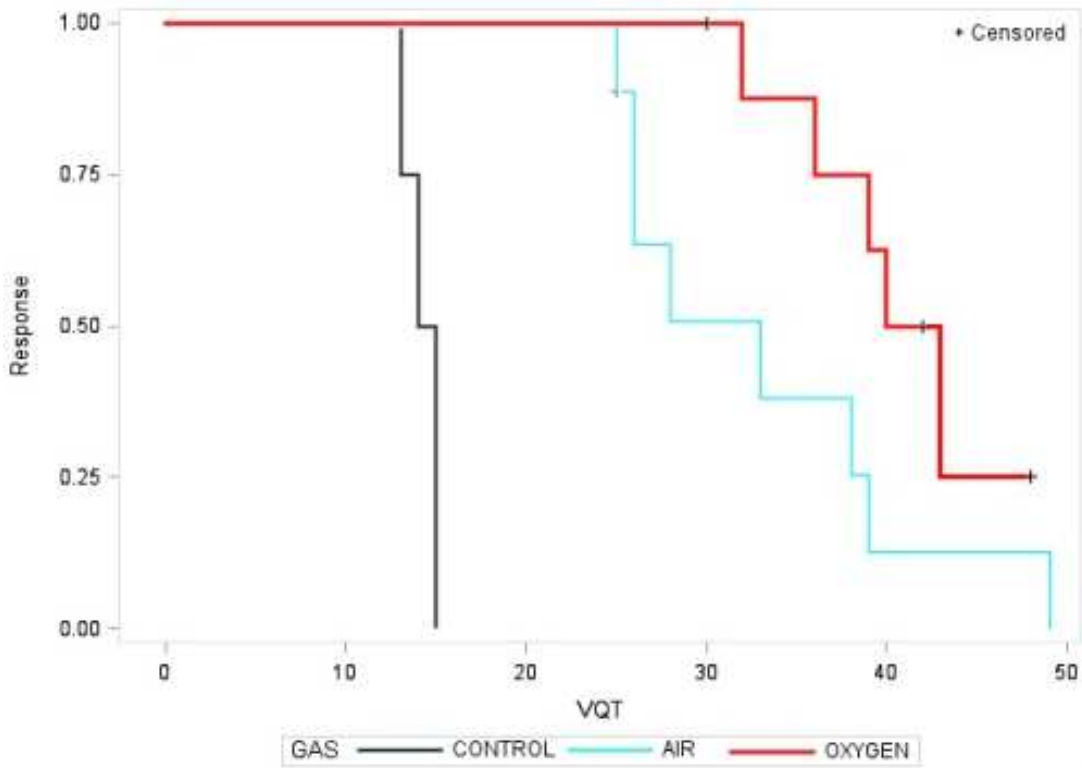
Figure 6.4   The outcome of tumor growth delay (VQT in days) using a Kaplan-Meier survival analysis illustrated the differences between responses.
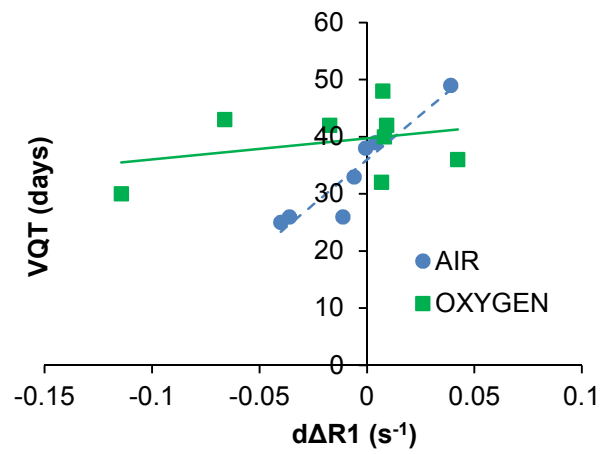
(a)
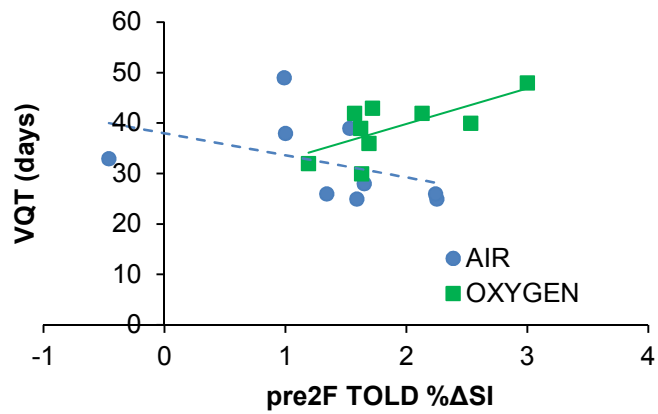
(b)

Figure 6.5 Correlation between non-invasive pre-irradiated OE-MRI measurements between and tumor growth delay for the effect of inhaling air (blue circles) or oxygen (green squares) on tumor radiation response observed as 4 times the initial irradiated tumor volume (VQT). Strong and moderate correlations were observed for (a) the difference between the second and first ΔR_1 measurements (dΔR_1) and VQT (R = 0.9395, P = 0.0017) for those animals inhaling air and (b) pre2F TOLD and VQT (R = 0.0.6949, P = 0.0378) for those animals inhaling oxygen, respectively.

Table 6.7 Correlations and Multivariate Regression Analysis of Pre- and Between-Therapy Factors Associated with Tumor Growth Delay for Split-Dose Irradiation.

Factors	No. of Subjects	Correlation R-value	Correlation P-value	Parameter Estimate	Multivariate P-value	Multivariate Statistics
pre1F Volume	9	0.9021	0.0009	NR	NR	
pre2F Volume	9	0.6772	0.0451	NR	NR	
pre1F 30 day Volume	9	-0.7633	0.0167	NR	NR	
pre2F 30 day Volume	9	-0.7788	0.0134	NR	NR	
mean TOLD	9	WC	NS	-6.1	0.0113	R^2 = 0.9898
pre2F baseline R_1	7	0.8545	0.0143	NR	NR	P =0.0017
pre2F O_2 challenge R_1	7	0.7650	0.0451	NR	NR	
pre1F ΔR_1	9	-0.8361	0.005	NR	NR	
pre2F ΔR_1	9	WC	NS	-95.2	0.0679	
dΔR_1	7	0.9395	0.0017	303.8	0.0006	
pre1F Volume	9	0.67663	0.0453	NR	NR	
pre2F TOLD	9	0.6949	0.0378	NR	NR	
mean TOLD	9	0.7022	0.035	7.14	0.1004	R^2 = 0.9276
pre2F O_2 challenge R_1	8	WC	NS	18.0	0.1427	P =0.0096
pre1F ΔR_1	9	-0.6558	0.0551	NR	NR	
mean ΔR_1	9	-0.7918	0.011	-177.9	0.0229	

mean TOLD are the voxels averaged over two slices
WC – weak correlation ($R < 0.50$)
NS – not significant ($P > 0.05$)
NR – factors not retained in the multivariate regression analysis

☐ Group inhaling air during irradiation
▢ Group inhaling oxygen during irradiation

Table 6.8 Validation Results of the Selected Multivariate Regression Models

Multivariate Regression Model	R^2		P-value		MSE	MSPE	MPE	MAPE
	Model Data	Test Data	Model Data	Test Data	Model Data	Test Data	Test Data	Test Data
6.6	0.9898	-	0.0017	-	1.62	-	34.2%	34.2%
6.7	0.9633	0.9960	0.0013	0.0632	4.37	4.99	27.4%	27.4%
6.8	0.8827	0.9960	0.0017	0.0020	11.2	2.50	3.30%	8.97%
6.9	0.9276	-	0.0096	-	4.61	-	-6.2%	19.1%
6.10	0.8676	0.0415	0.0064	0.9790	6.75	272.9	-16%	28.7%
6.11	0.6919	0.0287	0.0104	0.8306	13.1	138.3	-26%	40.1%

MSE – error mean square
MSPE – measures actual predictive capability compared to MSE
MPE –underestimates (+) or overestimates (-)
MAPE – measures accuracy of prediction (Table 6.2)

☐ Group inhaling air during irradiation
☐ Group inhaling oxygen during irradiation

$$VQT_{AIR} = 45.31 - 6.10(\text{mean TOLD}) - 95.16(\text{pre2F O2 challenge R}_1) + 303.83(d\Delta R_1)$$ (6.6)

$$VQT_{AIR} = 41.52 - 4.89(\text{mean TOLD}) + 308.79(d\Delta R_1)$$ (6.7)

$$VQT_{AIR} = 36.023 + 314.45(d\Delta R_1)$$ (6.8)

$$VQT_{OXYGEN} = 23.71 + 7.14(\text{mean TOLD}) + 17.95(\text{pre2F O2 challenge R}_1) - 177.86(\text{mean } \Delta R_1)$$ (6.9)

$$VQT_{OXYGEN} = 28.08 + 10.22(\text{mean TOLD}) - 139.91(\text{mean } \Delta R_1)$$ (6.10)

$$VQT_{OXYGEN} = 15.38 + 15.08(\text{mean TOLD})$$ (6.11)
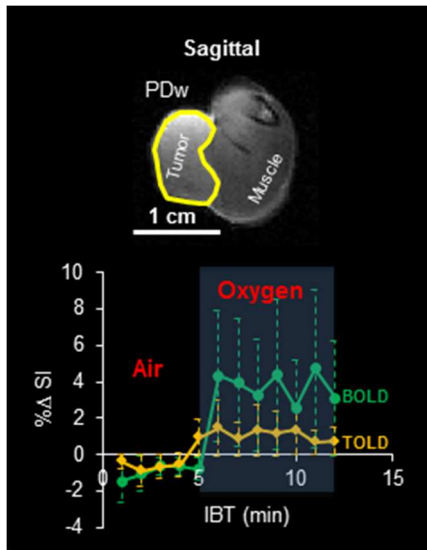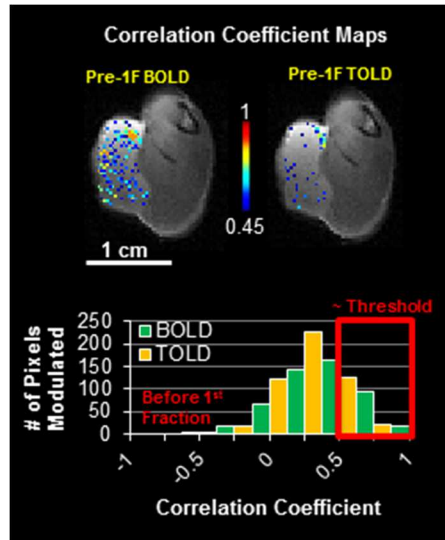
(a)   (b)
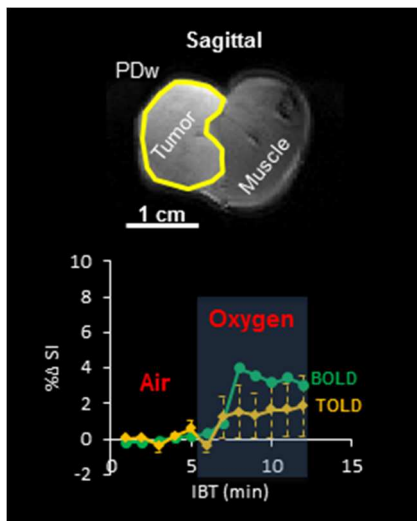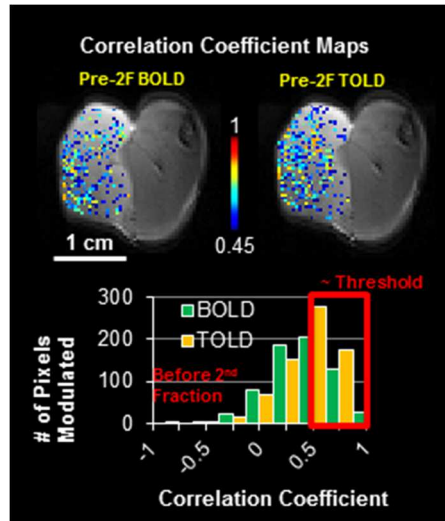
(c)   (d)

Figure 6.6 Illustration of dynamic interleaved BOLD and TOLD (IBT) %ΔSI measurements (a,c) and corresponding voxel-by-voxel correlation coefficient maps and histograms (b,d) before each fraction of dose. At a threshold (0.45), the histograms demonstrated increased IBT response after the first fraction of dose suggesting reoxygenation as verified from immunohistochemistry (Figure 6.9 and Figure 6.10).
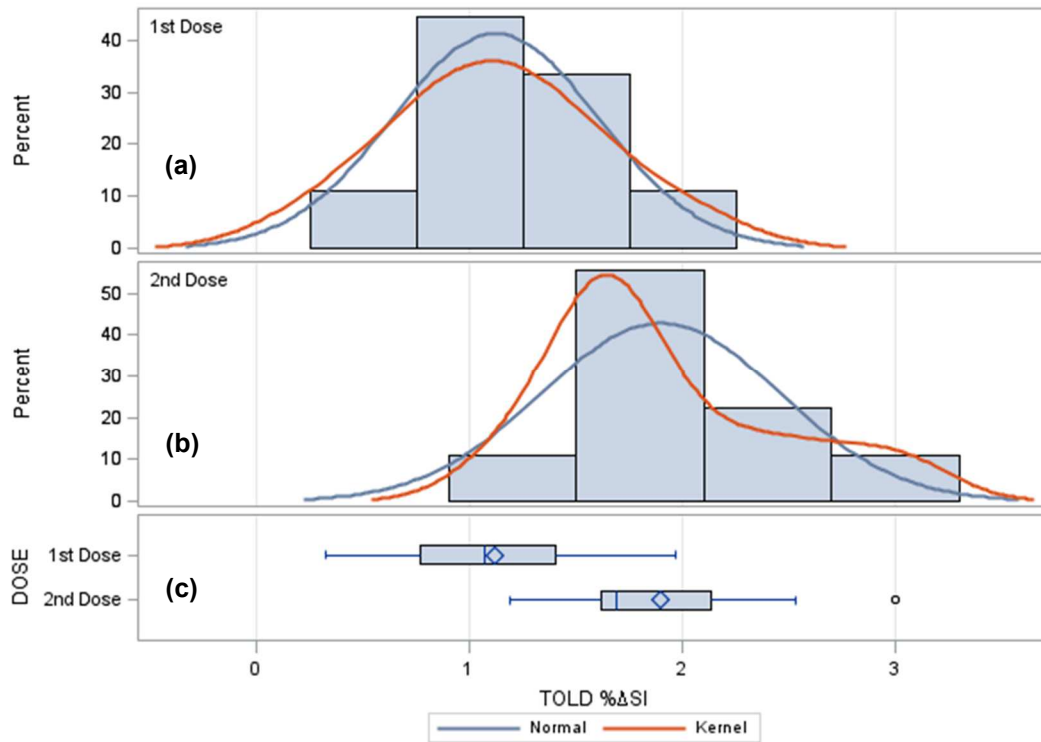
Figure 6.7 TOLD signal responses (%ΔSI) of tumors to oxygen breathing challenge for those tumors on rats breathing oxygen during irradiation. Histograms show relative frequencies of mean response in the tumor ROI before the (a) 1st dose; (b) 2nd dose of radiation. Normal and smoothing kernel distributions are overlaid (midpoints = 0 to 3, bin width = 1 %ΔSI). (c) Box plot reveals significant differences between the two mean TOLD measurements (P = 0.0061).

138
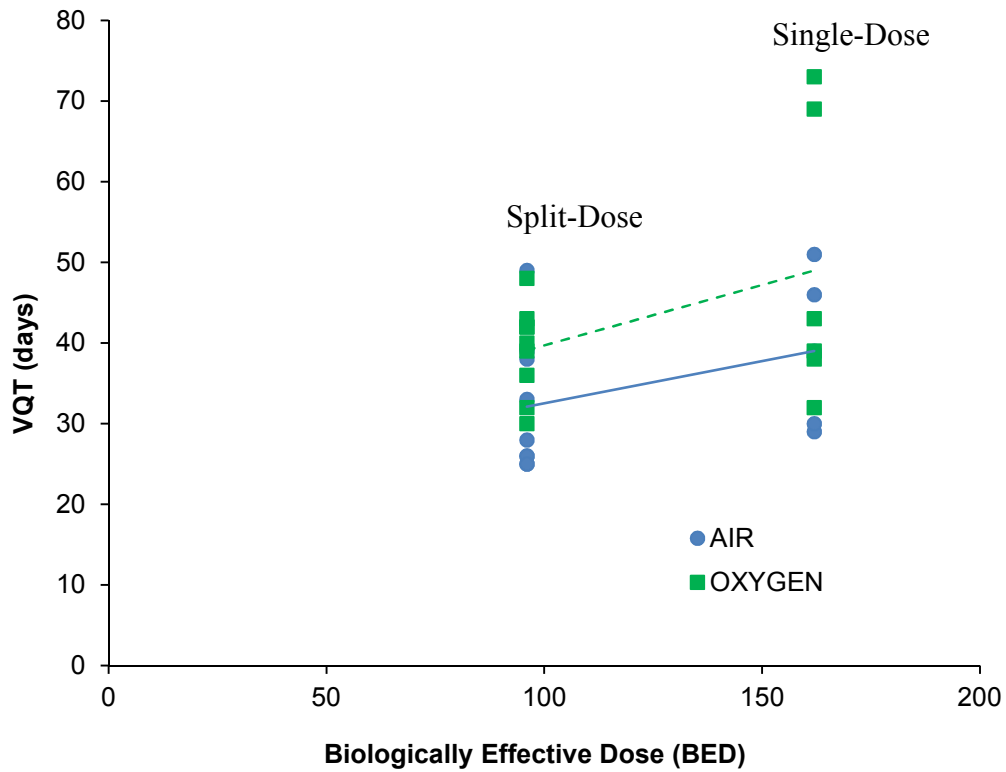
Figure 6.8   A comparison between the VQT data from Hallac et al. [37] single-dose investigation to split-dose fractionation VQT data using Dunning R3347-AT1 tumors based on the Biologically Effective Dose (BED = $(nd)\left[1 + \dfrac{d}{\alpha/\beta}\right]$) [59] as a method of comparing different dose fractionation regimens.
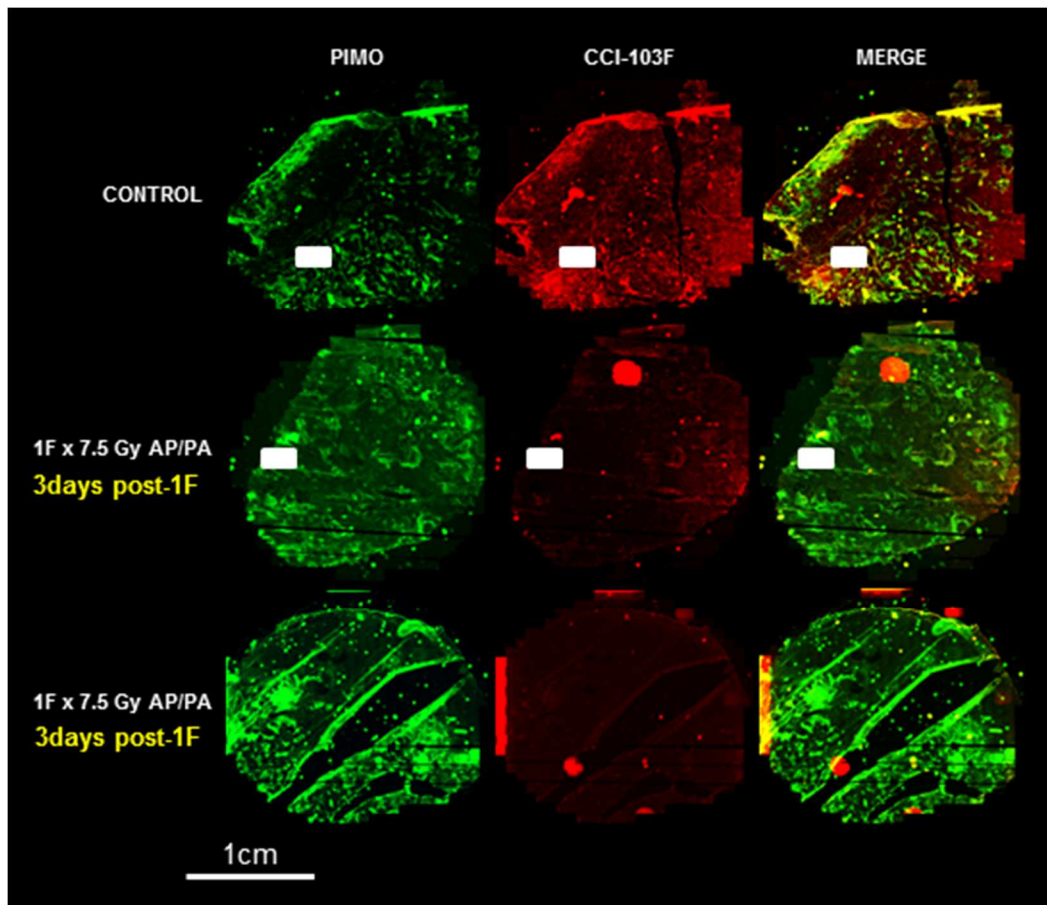
Figure 6.9 Immunohistochemistry images of an unirradiated (control, top row) and irradiated AT1 tumors (1F x 7.5 Gy AP/PA, bottom rows) while breathing oxygen. Illustration of the first (pimonidazole, green) and second (CCI-103F, red) hypoxic makers and when overlapping them gives yellow when merged (red and green). The unirradiated control tumor remained hypoxic in areas whereas the irradiated tumor became less hypoxic. Zoom in regions of tumor hypoxia staining (white rectangles) are shown in Figure 6.10.
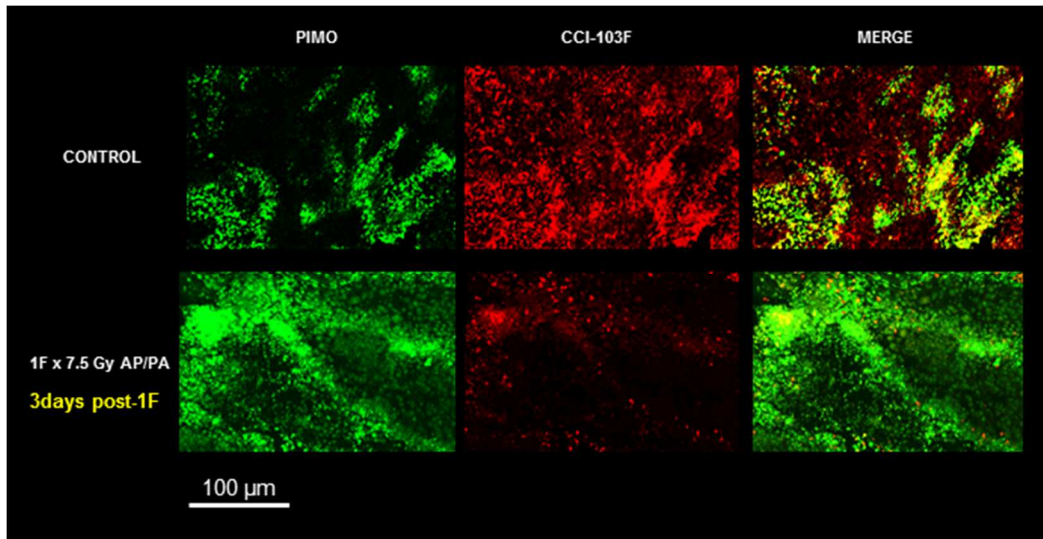
Figure 6.10   Zoom in region of immunohistochemistry images (Figure 6.9, Original magnification 20X) of an unirradiated (control, top row) and irradiated AT1 tumor (15 Gy, bottom row) while breathing oxygen. Pimonidazole, (green) and CCI-103F (red) hypoxia markers showed consistent extensive retained hypoxia in control tumor (overlap appears yellow). Meanwhile the irradiated tumor showed much less hypoxia three days after 15 Gy consistent with reoxygenation and the increase in the number of modulated BOLD and TOLD voxels.

Discussion and Conclusion

In this investigation, I found that intermediate volume Dunning R3327-AT1 prostate tumors had different OE-MRI responses before irradiation. All prostate tumors exhibited significant tumor heterogeneity which may have affected the response to radiation. The intermediate volume tumors observed during the split-dose fractionation illustrated that inhaling oxygen during irradiation provided an additional benefit in regards to delaying tumor growth. The OE-MRI measurements indicated that regardless of a smaller or larger tumor volume, better-oxygenated tumors exhibited increase tumor growth delay. Based on the correlation and multivariate regression analysis, the pre-irradiated OE-MRI measured the "apparent" oxygenation status of all prostate tumors non-invasively and provided insight to the prognosis on the response to radiation damage.

This portion of my radiobiological study provided additional support for the increased interest of hypofractionation in prostate cancer [174] by using MR imaging to non-invasively predict radiation response to a split-dose scheme. However, up to this point in my investigation the split-dose investigation did not obviously appear to have any enhanced VQT or significant efficiency beyond the VQT previously reported [37]. This may be due to the differences in the initial tumor volumes used for predicting the outcome of radiation response. In this previous report [37], initial tumor volumes responded well to radiation as they were small well-oxygenated volume tumors according to their OE-MRI measurements. Initially the intermediate volume size tumors had smaller OE-MRI values; thus, illustration of an unfavorable prognosis based on the first (1st) OE-MRI measurements. However, tumor oxygen measurements improved after the first fraction of dose. Consequently, tumor reoxygenation combined with inhaling oxygen between dose fractions may have played a significant role in delaying tumor growth in my split-

dose experiment suggesting increased radiosensitivity. Comparable to a clinical hypofractionation schedule [175,176], I used a split-dose schedule of 7 days apart with non-invasive measurements of OE-MRI covariates a day before. Thus, the timing of optimal reoxygenation was not investigated. Nevertheless, my assessment of tumor reoxygenation was confirmed by immunohistochemistry in AT1 tumors and I was able to stratify and predict non-invasively tumor reoxygenation for those animals inhaling air or oxygen during irradiation.

I also realize that there may be differences in the biologically effective dose (BED) between a single-dose (from Chapter 5 and from a previous investigation [37]) and split-dose treatment regimens. Based on the linear-quadratic (LQ) model [177], the single-dose group (BED = 162) may have experienced a 60% increase in biological effect (at high dose-rate) when irradiating tumors compared to a split-dose (BED = 96) fractionation schedule. The comparison between the VQT data from Hallac *et al*. [37] investigation using single-dose to my split-dose VQT shown in Figure 6.7 suggested that a higher BED used for irradiating the AT1 tumor will result to an increase in tumor growth delay and inhaling oxygen during irradiation may provide an additional benefit regardless of the BED. However, it is well documented that irradiation using a fractionation schedule spares normal tissue due to the time allowed between dose fractions for sublethal damage repair (SLD) and repopulation which is why hypofractionation is so attractive [174]. Yet, tumor cell survival will also increase with increase time allowed between fractions for SLD resulting in repopulation, which can occur up to eight hours after irradiation depending on the tumor type; thus, at a lower dose-rate, tumor cells become more resistant and less responsive. There is evidence that hypoxic cells totally inhibits SLD [178] but access to oxygen between dose fractions allows repair of sublethal damage to take place efficiently. Consequently, since my OE-MRI measurements from

the split-dose experiment indicated that the tumors were for the most part responsive to inhaling oxygen during gas challenge, these tumors were mildly aerated which supports SLD and repopulation resulting in increased tumor volumes by the time of the second dose fraction. Nevertheless, the AT1 tumors benefited from inhaling oxygen during split-dose irradiation and from tumor reoxygenation according to my observations. Whereas, greater efficacy may result when less time is allowed for the tumor to repopulate between dose fractions and using hyperthermia [179] to inhibit SLD with inhaling oxygen in split-dose irradiation. I suspect that less radiation dose would be expected to achieve the same therapeutic outcome under these increased radiosensitivity [142] conditions.

Previously, Hallac *et al*. demonstrated positive radiation response (VQT) correlations with non-invasive tumor oxygenation covariates (i.e. pre-irradiated TOLD $\%\Delta SI$ or ΔR_1) for animals with small tumors inhaling oxygen during irradiation. I have determined similar relationships with ΔR_1 from my single-dose group with large tumors from Chapter 5. To my knowledge, this is the first investigation to exploit OE-MRI to predict radiation response outcome using non-invasive tumor oxygenation measurements during the course of a split-dose regimen. O'Hara *et al*. [155], investigated VDT vs. tumor oxygenation to split-dose irradiation in murine tumors. However, it required an injection of paramagnetic material (India ink) directly into the tumors whereas no injection was required in my tumors. The primary goal of this investigation was to ascertain whether OE-MRI predictors were related to tumor growth delay and determine the importance of these covariates through statistical methods. I determined the merit of tumor growth delay in relation to prognostic factors influencing radiotherapy such as inhaling oxygen and tumor reoxygenation for split-dose hypofractionation regimen. My findings indicate an increased response outcome when inhaling oxygen during radiotherapy. For those inhaling air during irradiation, tumor reoxygenation ($d\Delta R_1$) as measured non-invasively

144

was a strong predictor of tumor growth delay as illustrated by the development and validation of a multivariate regression model.

Chapter 7

Contributions and Future Endeavors

In this dissertation I focused on utilizing non-invasive biomedical imaging modalities such as bioluminescence imaging (BLI), ultrasound (US) imaging, and magnetic resonance (MR) imaging to monitor the growth of prostate tumors or to assess interventions that inhibited the growth of prostate tumors. Several imaging acquisitions and imaging processing techniques were adopted or developed to evaluate the results of tumor oxygenation orthotopically or subcutaneously. The prostate tumors were found to be heterogeneous in signal intensity according to the digital magnetic resonance images. In most cases, depending on the size of the tumors, the tumor ROI was found to be modulated by inhaling oxygen based on the percent changes in BOLD or TOLD maps (Chapter 4 and 5) or correlation coefficient maps (Chapter 6). The oxygen-enhancement investigations implemented in this dissertation were very important because the "apparent" status of oxygen in the tumors or tumor oxygenation was indeed a significant prognostic factor at the time of split-dose irradiation according to Chapter 6 results. The degree of tumor oxygenation was also determined an important prognostic factor.

Orthotopic tumor xenografts are expected to better represent spontaneous human tumors. However, implantation and monitoring tumor growth are technically more challenging in deeper sites such as the prostate because straightforward palpation is not possible. Chapter 3 investigated the use of *in vivo* BLI in adult male nude rats since this non-invasive optical imaging technique has been reported reliable in mice. *In vivo* BLI was unsatisfactory for monitoring the growth of PC3-luc cancer cells in nude rats, although it is normally an excellent reliable tool in mice. I found that the change in *in vivo* BLI signals did not correlate well with the growth of the human prostate PC3 tumors

implanted in rats. These results indicated that *in vivo* BLI in rats must be used with caution. The reasons for the discrepancies are currently unknown but future attempts should consider the choice of small animal vendor source, immune status, gene expression of the *luc*-gene in adult male nude rats, or tumor physiological changes before pursuing *in vivo* BLI for high-throughput pre-clinical tumor radiobiology studies.

Despite the results of *in vivo* BLI, I achieved oxygen-enhanced MR imaging (OE-MRI) in orthotopic PC3 prostate tumors (Chapter 4). Oxygen was used as a paramagnetic contrast agent to enhance tumor ROI MR signal intensities. OE-MRI measurements exhibited various responses to inhaling oxygen. Immunohistochemistry confirmed OE-MRI results. Correlations were determined between BOLD %ΔSI and TOLD %ΔSI or ΔR_2^* and between TOLD %ΔSI and ΔR_2^*. The partial pressure of oxygen (pO$_2$) and arterial oxygen saturation (sO$_2$) of prostate tumors may be inferred non-invasively by R$_1$ mapping or TOLD %ΔSI and R$_2^*$ mapping or BOLD %ΔSI, respectively. I confirmed the timing in responses of BOLD %ΔSI and TOLD %ΔSI with the rat's pulse oximetry measurements from the ΔSpO$_2$. Immunohistochemistry and hypoxic fractions verified a tumor's large or small OE-MRI response. The OE-MRI responses in the PC3 tumors demonstrated higher signal intensities compared to the subcutaneous and orthotopic AT1 prostate tumors. The orthotopic tumors from both animal prostate models were allowed to grow to large volumes because *in vivo* BLI became problematic. However, since US imaging can be much cheaper and user-friendly compared to MR imaging, it is recommended that future work utilize the capabilities of the US's digital RF energy spectrum for detecting and calculating different tissue attenuations using power spectrum analysis to distinguish *in vivo* prostate tumor tissue from normal tumor tissue obtained from US images. Small animal or pre-clinical tumor radiobiology research studies begin with cancer cells implanted subcutaneously or orthotopically. Monitoring

the growth of orthotopic tumors implanted in the prostate of small animals can be a challenge to the operator when using MR as the initial step for implementing long-term studies. The cost of using US imaging compared to MR imaging to monitor tumor growth can provide significant cost savings. In addition, tracking the growth of small deep-seated tumors can be more efficient with an unbiased approach for extracting prostate pathology by using spectral analysis of US images.

OE-MRI is a non-invasive imaging modality that provided insight to the "apparent" oxygen status of the prostate tumors investigated. Correlation coefficient mapping was very efficient for examining modulated voxels due to inhaling oxygen and for assessing tumor reoxygenation between does fractions (Chapter 6). Also, observed increase percent changes in BOLD and TOLD signal intensities after the first fraction of dose suggested that the prostate tumors experienced reoxygenation as confirmed by immunohistochemistry double marker approach. The question that is appropriate to ask when using this imaging processing method for OE-MRI will be….."what is the tumor oxygen consumption rate and blood flow rate in this voxel?" The answer to this question is a future endeavor to be investigated. OE-MRI was used for predicting tumor response to a single- (Chapter 5) or split-dose (Chapter 6) hypofractionation regimen. Both prediction cases were useful. However, no benefit was determined for the single-dose case whereas the split-dose case revealed a benefit. Furthermore, in the split-dose case, the MSPE was much smaller than the MSE of the final air model selected (Equation 6.6). In addition, the MAPE was within 9% accuracy which may be in a tolerable range considering the scope of the project and the level of prediction. However, the final oxygen model selected requires further investigation since the validation analysis did not perform well. More samples may be required for a complete development and validation of an oxygen model for predicting tumor growth delay. I also recommend that these

models be compared to any previous empirical results, simulations, or theoretical expectations for predicting tumor growth delay.

Increased tumor radiosensitivity was observed when inhaling oxygen and when tumors reoxygenated, suggesting patient stratification for clinical implementation and for biological optimization of radiotherapy treatment planning systems. However, the timing of dose fractionation can be an important factor in regards to when reoxygenation of tumor cells are optimal and before suspected repopulation from an increased tumor cell survival because the increased time allowed (up to 7 days between dose fractions) for sublethal damage (SLD) repair. Consequently, future *in vivo* work should be implemented combining inhaling oxygen and hyperthermia with split-dose irradiation since heat delivery is known to inhibit SLD repair and increase radiosensitivity (also with inhaling oxygen during irradiation as reported in this dissertation).   Less radiation dose would be expected to achieve the same therapeutic outcome under these increased radiosensitivity conditions.

Appendix A

Explore accuracy and repeatability of R_1 measurements and evaluate the effect of

temperature stability on R_1

ABSTRACT

Purpose

Explore the intrinsic longitudinal relaxation rates of two (2) Gadavist phantoms, identify the range at which AT1 prostate tumor's relaxation rates exist within the phantom R_1 relaxation measurements, and demonstrate that inhaling oxygen affects R_1 relaxation rates similar to Gadavist phantoms.

Materials and Methods

All measurements were performed on Varian 4.7 T small animal MR scanner using a body coil or a 35 mm home-build transmission and receive solenoid volume coil. Phantom 1 was made from a 10 mL stock solution of 50 µL of gadolinium-DO3A-butrol (gadobutrol or Gadavist, Schering AG, Berlin, Germany) prepared and mixed in distilled water to a 50mL polypropylene conical tube (Blue Max™, Becton Dickerson Labware, Franklin, Lakes, NJ, USA). Obtained from the stock solution of Phantom 1, concentration volumes of 0 µL, 100 µL, 200 µL, 500 µL, 1,000 µL, and 2,000 µL in distilled water dispensed into 6 different 5,000 µL glass tubes and sealed Phantom 2 was made from a 10 mL stock solution of 50 µL of gadolinium-DO3A-butrol (gadobutrol or Gadavist, Schering AG, Berlin, Germany) prepared and mixed in saline to a 50mL polypropylene conical tube (Blue Max™, Becton Dickerson Labware, Franklin, Lakes, NJ, USA). Obtained from the stock solution of Phantom 2, concentration volumes of 50 µL in saline was dispensed into a 20 mL scintillation vial (Kimble®, Toledo, OH, USA) and sealed. During magnetic resonance (MR) imaging, the horizontal bore of the magnet was heated (for Phantom 2 only) using a heater module and the temperature was monitored and recorded using a 9-foot fiber optic temperature probe and module (MR-compatible Model 1025 Monitoring & Gating System, SA Instruments, Inc., Stony Brook, NY, USA). The temperature varied from approximately 25°C to 29°C and was found to vary less than 0.2°C during MR relaxation acquisition. The temperature of the magnet bore was allowed to stabilize between measurements by waiting sufficient time.

R_1 measurements

Quantitative R_1 (R_1 = 1 / T1) measurements were acquired as previously described [37] using a sequential variable repetition time (TR) 2-D multi-slice spin-echo sequence with TE/TR = (20 ms / 100, 200, 300, 500, 700, 900, 1500, 2500, 3500, 4500 ms). Three (3) coronal slices were acquired with slice thickness = 2 mm, FOV = 60 mm x 60 mm, matrix = 128 x 128, NEX = 1.

Data Processing

Voxel-by-voxel quantitative R_1 maps were generated using a nonlinear saturation recovery (SR) equation based on:

$$M_Z(t) = M_O(1 - e^{-R_1 \times tau})$$

where $M_Z(t)$ is the time-dependent longitudinal magnetization based on the recovery back to equilibrium after an excitation pulse, M_O is the equilibrium nuclear magnetization, and tau is the repetition times used as previously described [37]. Only the voxels that provided reliable fitting with a coefficient of determination $R^2 \geq 0.95$ throughout the processing of the digital images of the quantitative R_1 maps were used in data analysis.

Results

A strong linear relationship was observed between R_1 and different concentrations of Gadavist (R^2 = 0.9957) for Phantom 1. An inverse linear relationship was observed between temperature and R_1 (R^2 = 0.8753) for Phantom 2. The range at which AT1 tumor relaxation rates ($R_1 \approx 0.5$ s^{-1} [49]) exist was between concentration Gadavist volumes 0 μL (R_1 = 0.3545 s^{-1}) and 100 μL (R_1 = 0.8707 s^{-1}) when contained in distilled water and around 50 μL (R_1 = 0.4285 s^{-1}) when contained in saline at 25°C.

Conclusion

Paramagnetic materials with unpaired electrons (e^-) such as gadolinium and oxygen molecules do affect the intrinsic longitudinal relaxation rates. The intrinsic longitudinal relaxation rates are

affected also by temperature. Variation in temperature during MR imaging should be considered when interpreting R_1 values.

Conc. Vol. [Gd] mM	Tube Label	R_1 (s^{-1}) Scan 1	R_1 (s^{-1}) Scan1 std	R_1 (s^{-1}) Scan2	R_1 (s^{-1}) Scan2 std	R_1 (s^{-1}) Scan3	R_1 (s^{-1}) Scan3 std	R_1 mean (s^{-1})	R_1 std (s^{-1})	ΔR_1 (s^{-1})
0	baseline	0.347	0.0319	0.3554	0.026	0.3338	0.0284	0.3454	0.010889	0.00
100	2	0.8932	0.0255	0.8524	0.0305	0.8665	0.0333	0.8707	0.020722	0.58
200	3	1.4813	0.0847	1.396	0.1279	1.4954	0.1316	1.457567	0.053782	1.16
500	4	2.3928	0.0603	2.3085	0.0595	2.3568	0.057	2.3527	0.042299	2.06
1000	5	4.1387	0.0577	4.146	0.0848	4.0728	0.0581	4.119167	0.04032	3.83
2000	6	7.848	0.1875	7.8838	0.2074	7.7582	0.227	7.83	0.064706	7.54

154
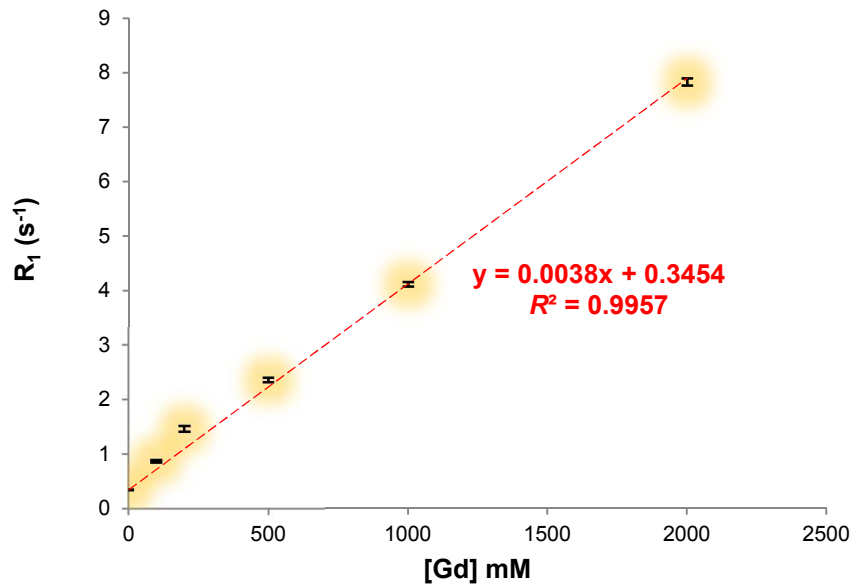
Multi-Slice Spin Echo (300ms/20ms)

$y = 0.0038x + 0.3454$
$R^2 = 0.9957$

1000 mM   0 mM   500 mM
2000 mM   100 mM   200 mM

Relaxivity Measurements of Gadavist Phantom #1

TR (sec)

0.1 0.2 0.3 0.5 0.7

0.9 1.5 2.5 3.5 4.5

zero conc.

0 µL

$R^2 = 0.9984$

Voxel (35,62)

$R_1 = 0.3562$ s^{-1}

R$_1$ @ 0 µL

(a)

TR (sec)

0.1 0.2 0.3 0.5 0.7

0.9 1.5 2.5 3.5 4.5

100 mM

100 µL

$R^2 = 0.9972$

Voxel (70,65)

$R_1 = 0.8447$ s^{-1}

R$_1$ @ 100 µL
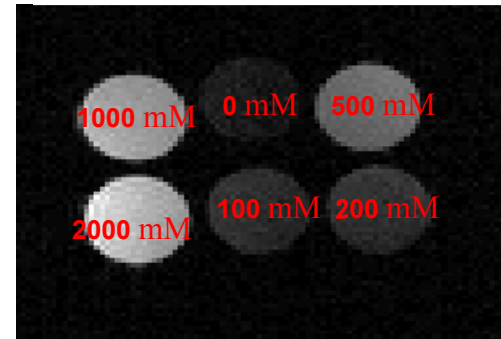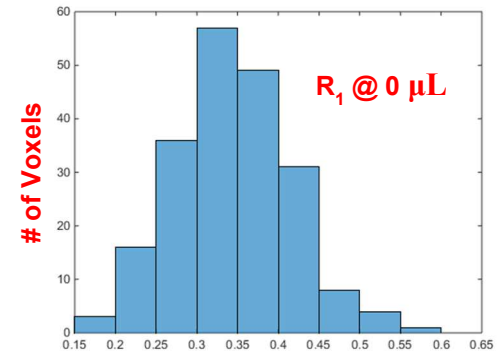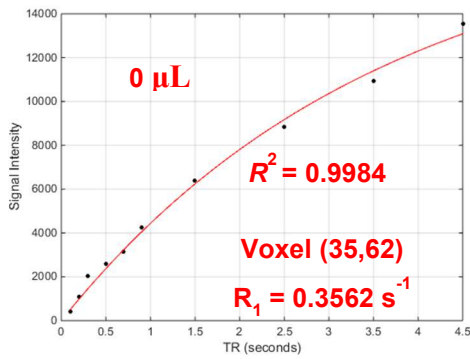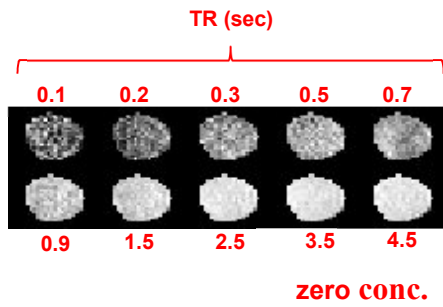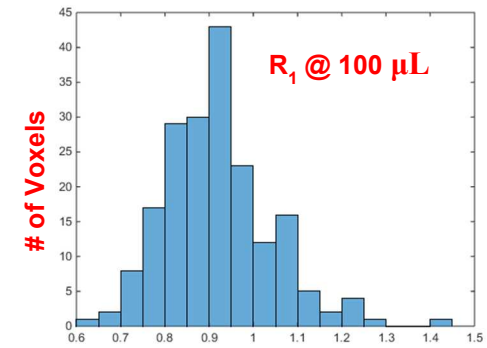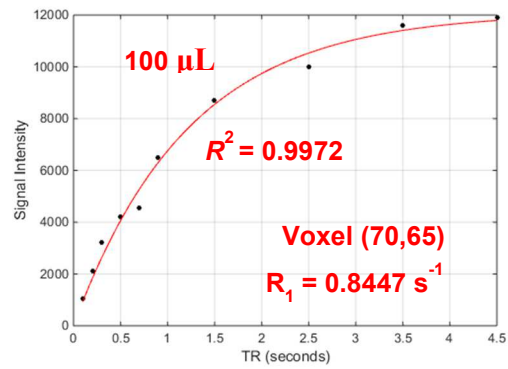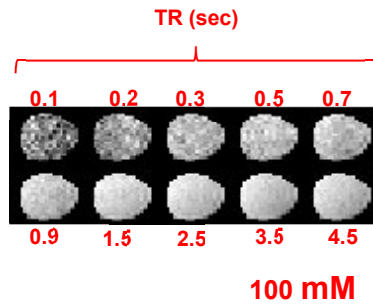
(b)

Relaxation Fitting of Gadavist Phantom #1
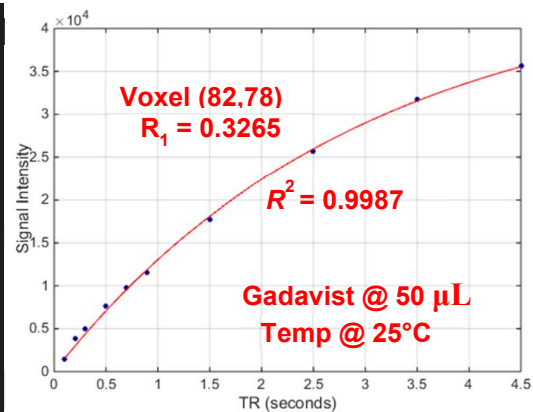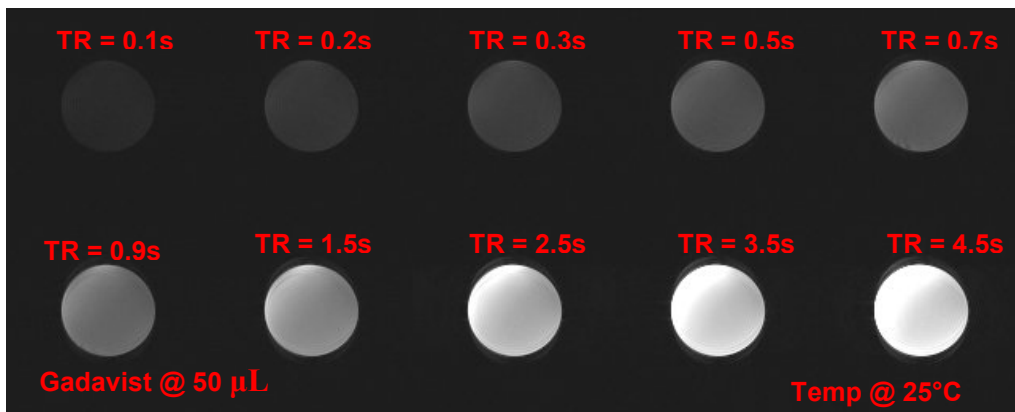
50 μL Conc. Volume			
Temp. (°C)	Temp. std.	Scan	Scan std.
25.0	0.07	0.4166	0.0081
26.7	0.13	0.4116	0.0081
27.2	0.18	0.3910	0.0082
28.9	0.16	0.3654	0.0078
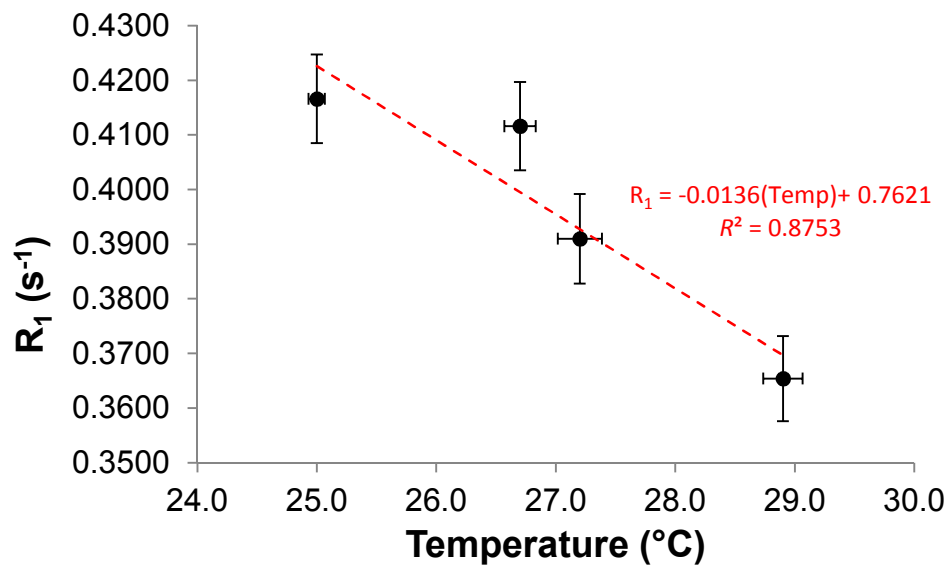
Relaxivity Measurements of Gadavist Phantom #2
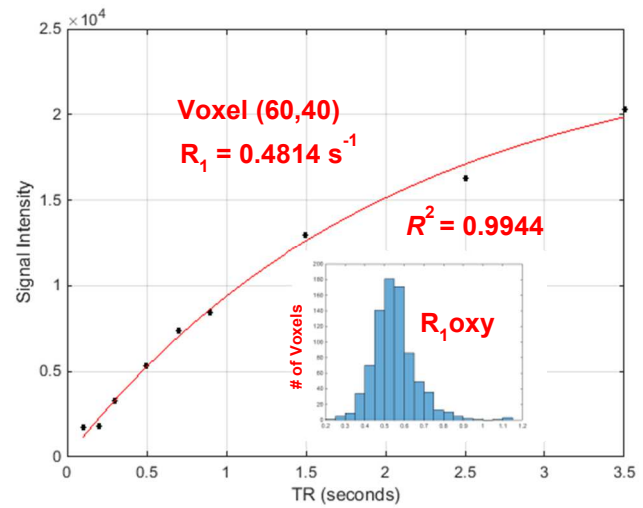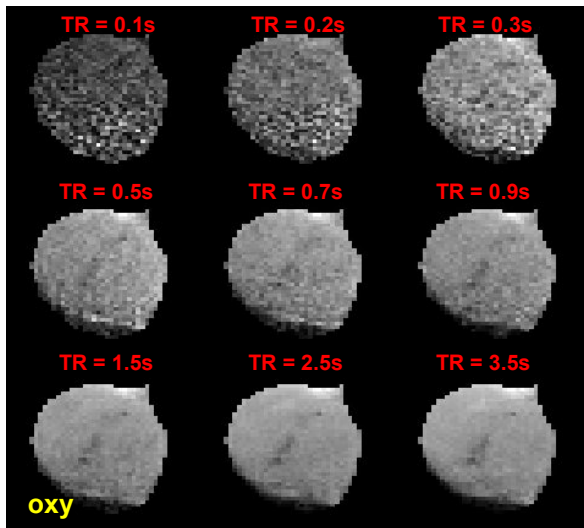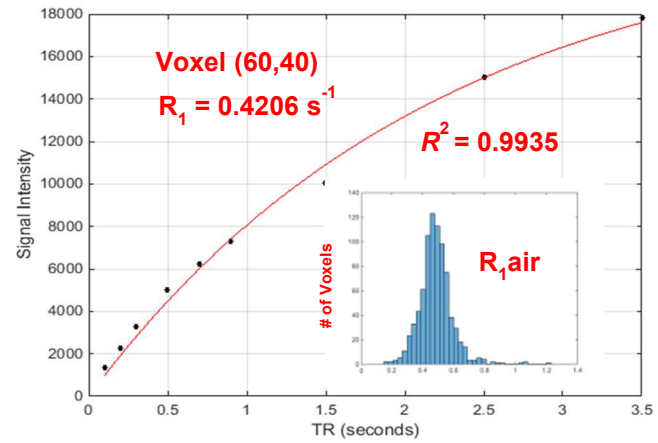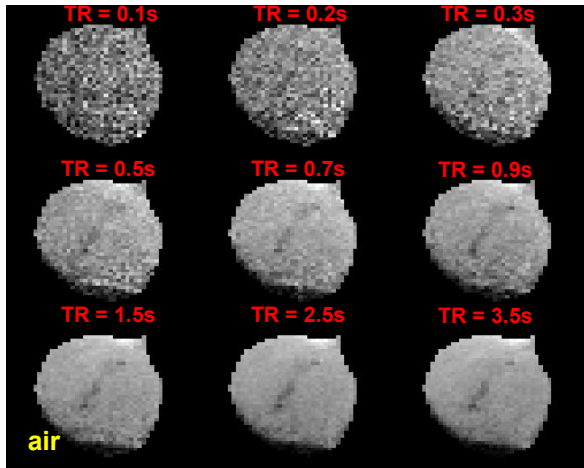
Relaxivity Fitting of a Representative AT1-SQ Prostate Tumor Inhaling Air and Oxygen

Appendix B

Method for Correlation Coefficient Mapping in AT1 Prostate Tumors

The following steps for processing the normalized threshold correlation coefficient maps were used to examine modulated voxels due inhaling oxygen from the BOLD effect (T_2^*-weighted images) or TOLD effect (T_1-weighted images) as presented in Figures A.1-A.7 on the next few pages. The statistical inferences about the change in voxel correlation values were determined from the basis of the Student's t-statistic using the "average waveform" from the BOLD and TOLD effects instead of the "ideal waveform". A positive correlation was interpreted as increased oxygenation in the vicinity of the voxel as the concentration of inhaled oxygen increased. A negative correlation was interpreted as decreased oxygenation in the vicinity of the voxel as the concentration of inhaled oxygen increased.

Pixel Temporal-Spatial Plot

PC3 ORTHOTOPIC PROSTATE TUMOR

Muscle

Tumor

Pixels Location

C2-R02 T$_2$-Weighted

Air

Oxygen

Air

160

MR Signal

Pixel 71, 71

Pixel 71, 72

Pixel 71, 73

Pixel 71, 74

Pixel 71, 75

0   10   30   40
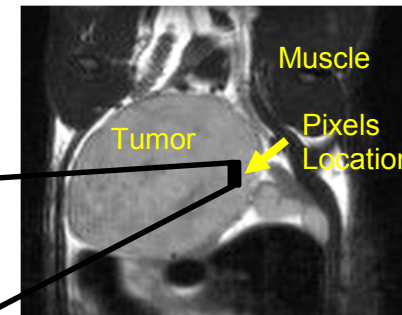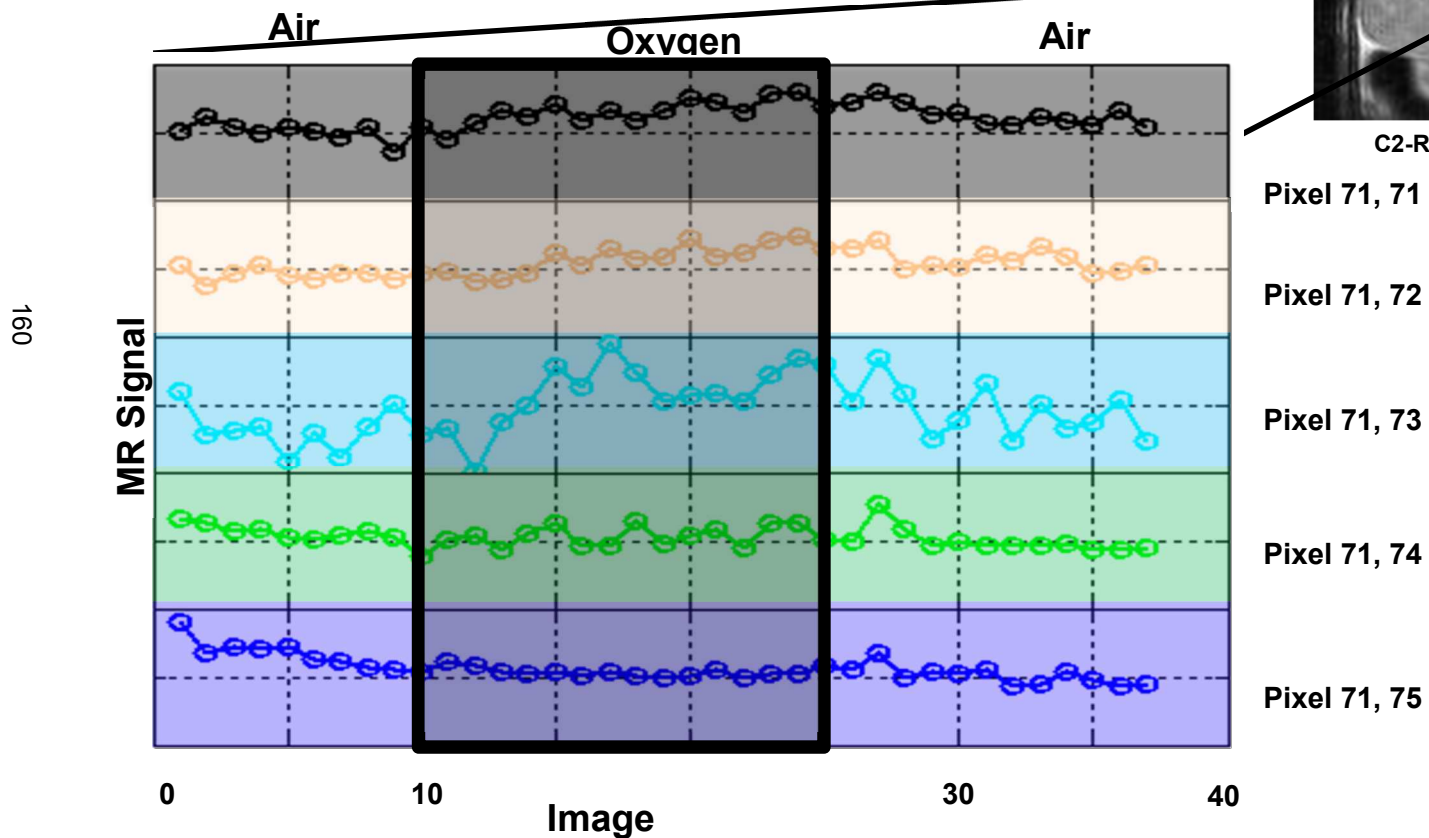
Image

Normalization of Raw MR Signal using Student's t-statistic
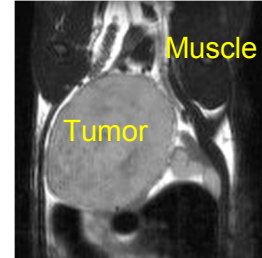
Normalization consists of centering and scaling the MR Signal Intensity by subtracting the mean pixel signal intensity value and dividing by the standard deviation

BOLD (R2*) Reference Time Waveforms

C2-R02 T$_2$-Weighted Image
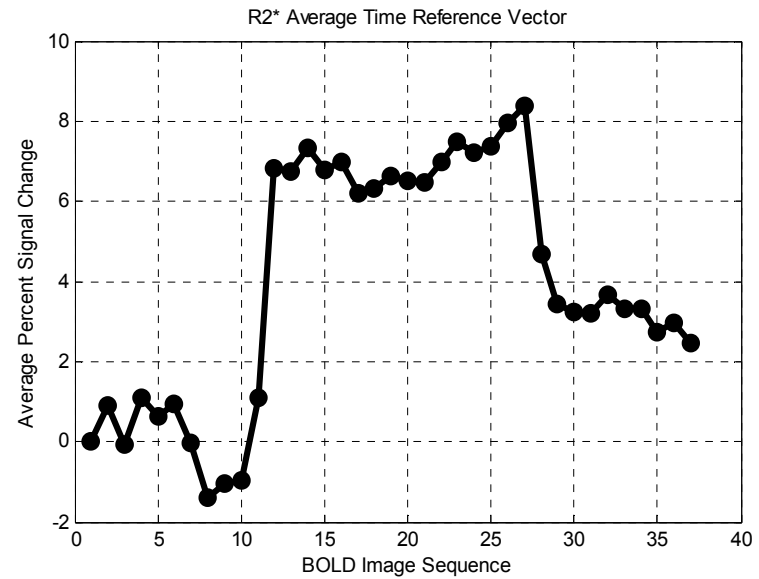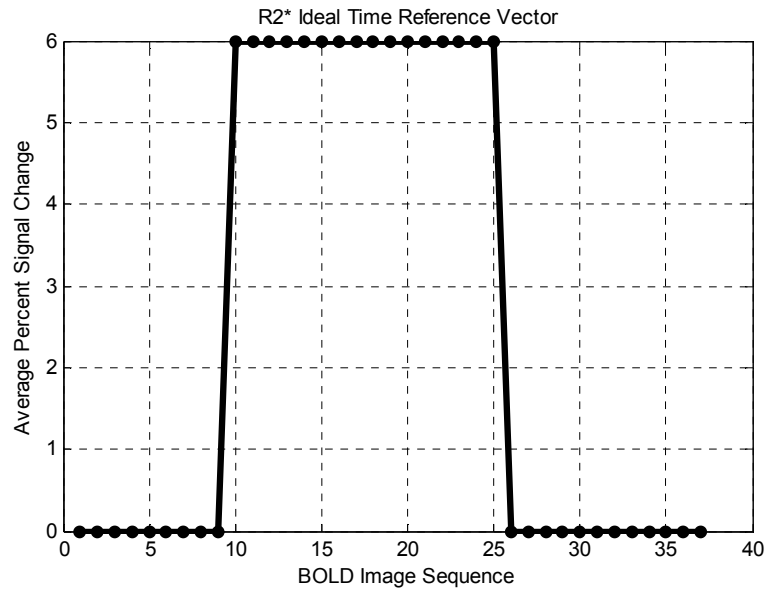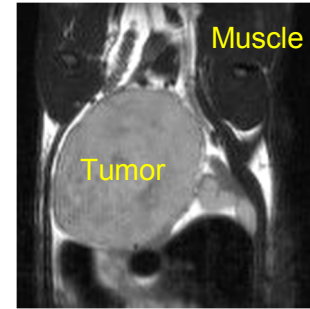
Bandettini PA, Jesmanowicz A, Wong EC, Hyde JS (1993) Processing strategies for time-course data sets in functional MRI of the human brain. *Magn Reson Med* 30: 161–173

Normalized MR Signal and Reference Time Waveforms
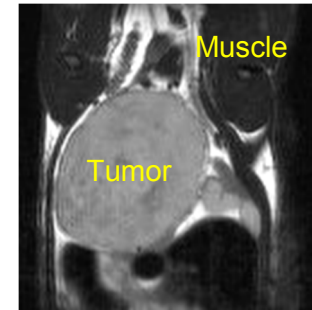
C2-R02 T_2-Weighted Image

Time-Domain of MR Signal Data

(Pixel 71, 71)

- Normalized MR Signal Waveform
- Ideal Time Reference Waveform

Time-Domain of MR Signal Data

(Pixel 71, 71)

- Normalized MR Signal Waveform
- Average Time Reference Waveform
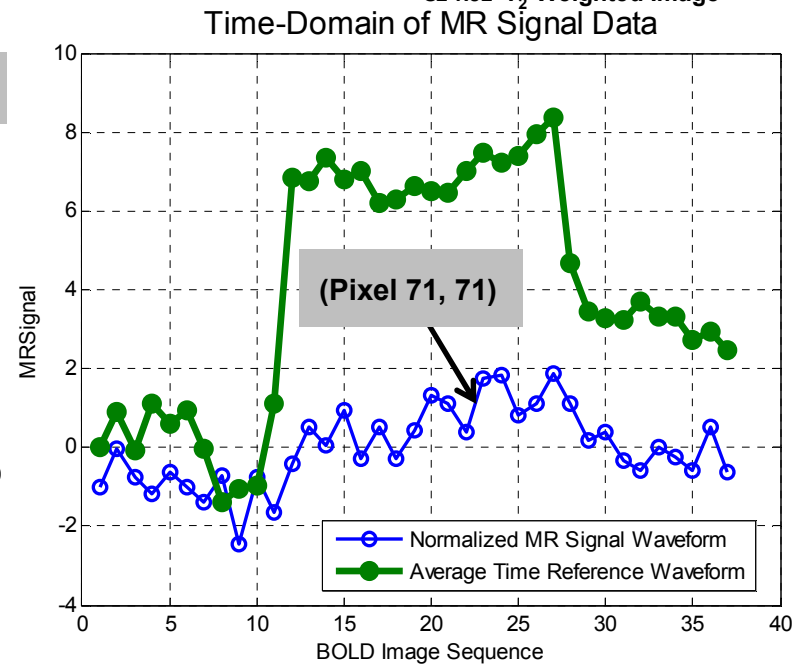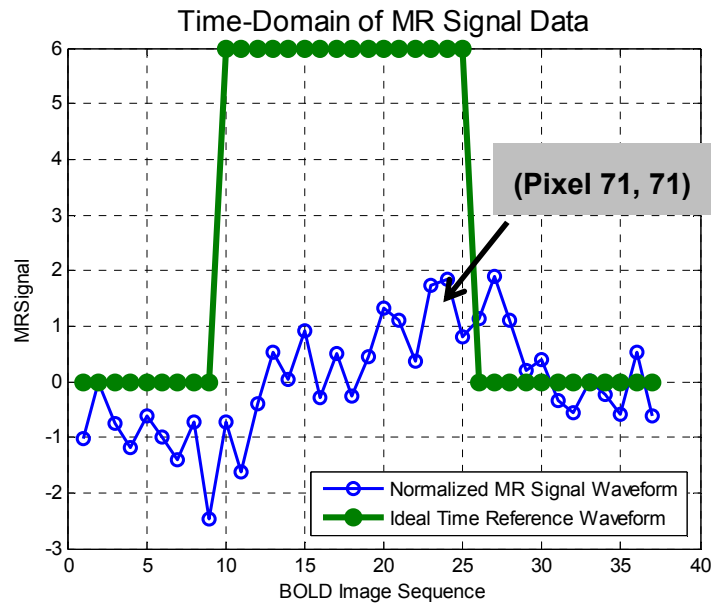
Normalized Correlation Coefficient Maps
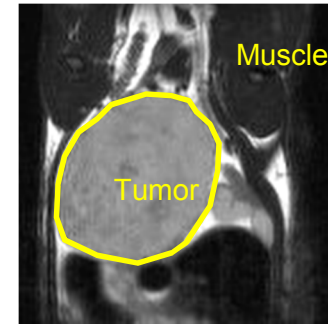
PC3-R02-ORTHO Anatomical Image
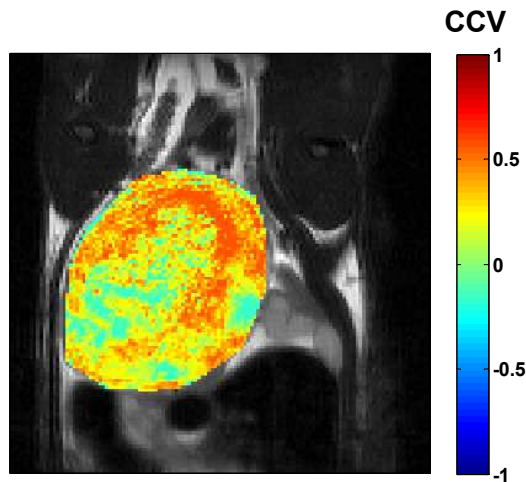
Normalized Correlation Coefficient map using *Ideal* Time Reference Waveform
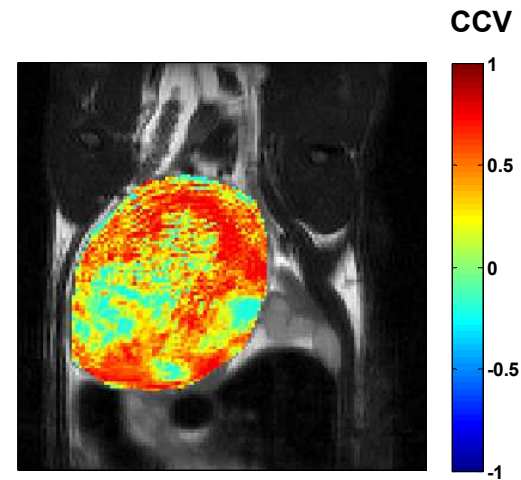
Normalized Correlation Coefficient map using *Average* Time Reference Waveform

Normalized Threshold Correlation Coefficient Maps

PC3-R02-ORTHO Anatomical Image

Threshold = 0.25

Threshold = 0.50

Threshold = 0.70
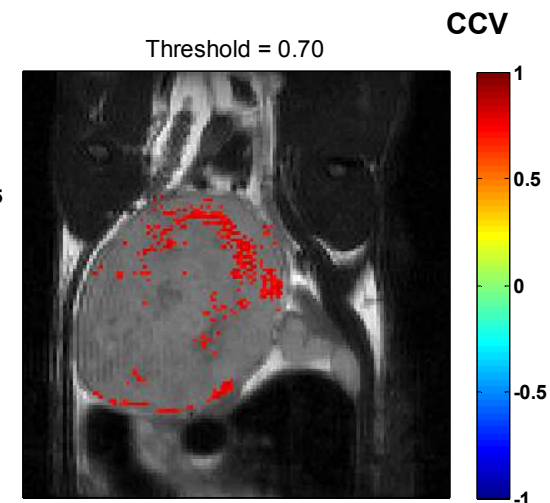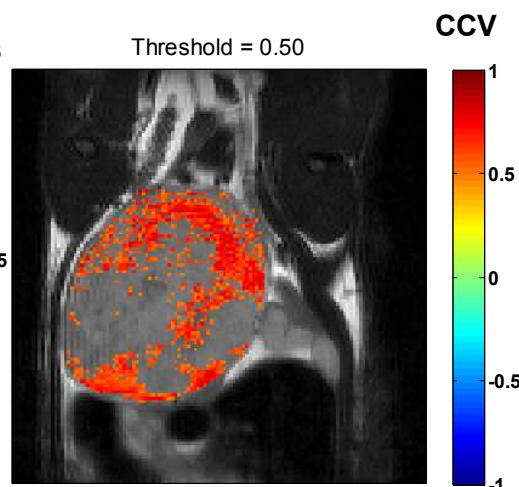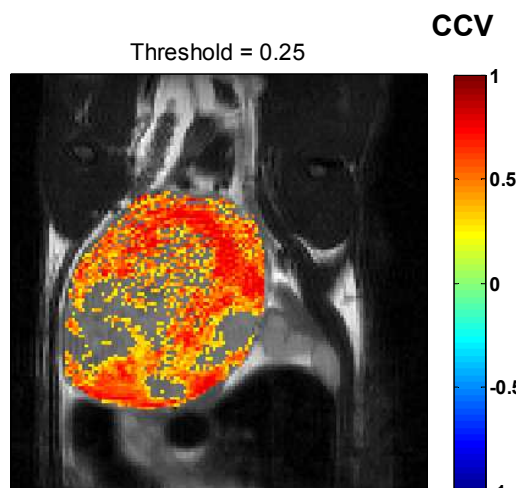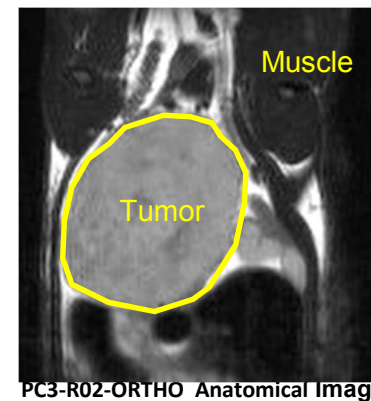
Threshold Correlation Coefficient maps using _Average_ Time Reference Waveform

BOLD and TOLD Normalized Threshold Correlation Coefficient Maps

Statistical Inferences for Setting Threshold on Correlation Coefficients Values

$$H_o: \rho_{12} = 0$$

$$H_a: \rho_{12} \neq 0$$

$$t^* = \frac{r_{12}\sqrt{n-2}}{\sqrt{1 - r_{12}^2}}$$

$$|t^*| > t\left(1 - \frac{\alpha}{2}; n-2\right)$$

Threshold = 0.45

CCV
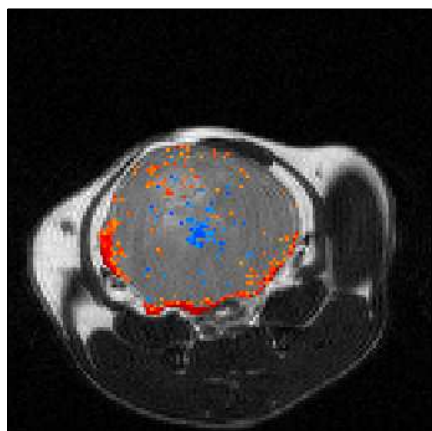
BOLD Response

Threshold = 0.45

CCV
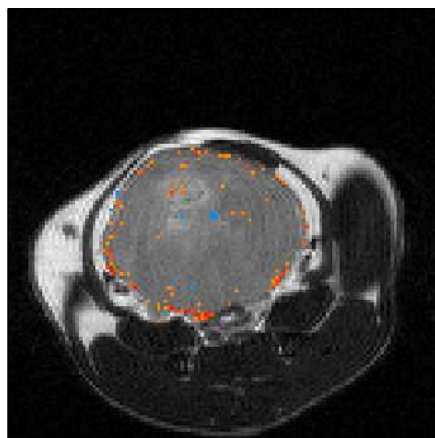
TOLD Response

(+) correlation

↑ O$_2$ Delivered
↑ Oxygenation
↓ O$_2$ Consumption?
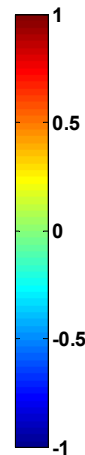
Tumor Volume:
~ 11.8 cm^3

Tumor

Muscle
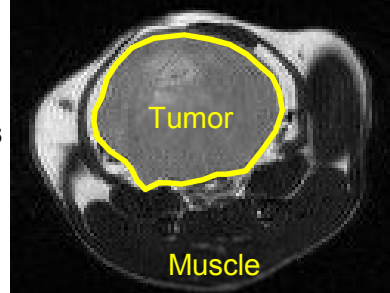
G5-R03-AT1-ORTHO Anatomical Image

(-) correlation

↑ O$_2$ Delivered
↓ Oxygenation
↑ O$_2$ Consumption?

Appendix C

List of Abstracts, Conference Presentations, and Publications

Peer-reviewed Conference Proceedings:

White DA, Zhang Z, Li L, Gerberich J, Zhou H, Zhang Z, Saha D, Peschke P, Zhang Z, Mason RP. Developing a Non-Invasive MRI Prognostic Biomarker to Predict Response to Hypofractionated Radiotherapy. American Association of Physicists in Medicine –57th Annual Meeting & Exhibition, Anaheim, CA, July 2015. Oral.

White DA, Zhang Z, Zhou H, Saha D, Peschke P, Zhang Z, Mason RP. Assessing the utility of Oxygen-Enhanced Magnetic Resonance Imaging (OE-MRI) to predict radiation response of rat prostate Tumors. International Society of Magnetic Resonance in Medicine Scientific 23rd Annual Meeting, Toronto, Ontario, Canada, June 2015.

White DA, Zhang Z, Peschke P, Mason RP. Quantitative Oxygen-Enhanced Magnetic Resonance Imaging (OE-MRI) Biomarkers of Tumor Response to Radiation. International Society of Magnetic Resonance in Medicine Scientific Workshop – Magnetic Resonance in Cancer: Challenges & Unmet Needs, Austin, Texas, USA, November 2014. Oral.

White D, Mason RP. Non-invasive pre-clinical MR imaging of prostate tumor hypoxia for radiation therapy prognosis. *Int J Cancer Ther Oncol* 2014;2(2):020243. DOI: 10.14319/ijcto.0202.43.

Conference Presentations:

"Limits of *In Vivo* Bioluminescence Imaging of Prostate Tumor Development: Caveat Emptor" **D. A. White**, J. Gunpat, R. Lopez**,** R. P. Mason, H. Liu, ACES, UT Arlington, TX March 2014.

"Mathematical modeling of tumor response to radiation: radio-sensitivity correlation with BOLD, TOLD, ΔR_1 and ΔR_2^* investigated in large Dunning R3327-AT1 rat prostate tumors" A. Belfatto*, **D. A. White**, Z. Zhang, Z. Zhang, P. Cerveri, G. Baroni, R. P. Mason, 37th Annual International Conference of the IEEE Engineering in Medicine and Biology Society of the IEEE Engineering in Medicine and Biology Society (EMBC'15) accepted (#1633), MiCo, Milano Conference Center, Milano, Italy, August 25-29, 2015.

"MRI predictions of split high-dose radiation response in rat prostate tumors" **D. A. White**, Z. Zhang, L. Li, J. Gerberich, H. Zhou, Z. Zhang, S. Stojadinovic, D. Saha, P. Peschke, R. P. Mason, 61st Annual Meeting Radiation Research Society, Weston, FL, September 19-22, 2015.

Peer-reviewed Journal Articles:

Accepted:

Zhao, D, Pacheco-Torres J, Hallac R, **White D**, Peschke P, Cerdan S, Mason R. Dynamic oxygen challenge evaluated by NMR T1 and T2* - insights into tumor oxygenation. NMR Biomed. 2015.

Under Preparation:

White DA, Gunpat J, Denney R, Li L, Peschke P, Mason RP. Assessment of Non-Invasive Prognostic Biomarker Measurements in Rat and Human Orthotopic Prostate Tumor Models using Oxygen-Enhanced Magnetic Resonance Imaging.

White DA, Zhongwei Z, Zhang Z, Peschke P, Mason RP. Evaluation of Oxygen-Enhanced Magnetic Resonance Imaging Non-Invasive Prognostic Biomarkers for Predicting Radiation Response of Large Prostate Tumors.

White DA, Zhongwei Z, Zhang Z, Gerberich J, Peschke P, Mason RP. Prostate Tumor Prognostic Factors in Split-Dose Irradiation: Predicting the Outcome Non-invasively using Oxygen-Enhanced Magnetic Resonance Imaging.

Belfatto A, **White DA**, Mason RP, Zhang Z, Stojadinovic S, Baroni G, Cerveri P. Tumor radio-sensitivity assessments by means of volume data and magnetic resonance indices measured on prostate tumor rats. Medical Physics.

References

1. Siegel RL, Miller KD, Jemal A. Cancer statistics, 2015. *CA-Cancer J Clin* 2015;65(1):5-29.
2. Jemal A, Siegel R, Xu J, Ward E. Cancer Statistics, 2010. *CA-Cancer J Clin* 2010;60(5):277-300.
3. Kelloff GJ, Choyke P, Coffey DS. Challenges in Clinical Prostate Cancer: Role of Imaging. *Am J Roentgenol* 2009;192(6):1455-1470.
4. D'Amico AV, Moul JW, Carroll PR, Sun L, Lubeck D, Chen M-H. Surrogate End Point for Prostate Cancer–Specific Mortality After Radical Prostatectomy or Radiation Therapy. *J Natl Cancer I* 2003;95(18):1376-1383.
5. Pisansky TM, Cha SS, Earle JD, Durr ED, Kozelsky TF, Wieand HS, Oesterling JE. Prostate-specific antigen as a pretherapy prognostic factor in patients treated with radiation therapy for clinically localized prostate cancer. *J Clin Oncol* 1993;11(11):2158-2166.
6. Pisansky TM, Kahn MJ, Rasp GM, Cha SS, Haddock MG, Bostwick DG. A multiple prognostic index predictive of disease outcome after irradiation for clinically localized prostate carcinoma. *Cancer* 1997;79(2):337-344.
7. Pisansky TM, Kahn MJ, Bostwick DG. An enhanced prognostic system for clinically localized carcinoma of the prostate. *Cancer* 1997;79(11):2154-2161.
8. Movsas B, Hanlon AL, Teshima T, Hanks GE. Analyzing predictive models following definitive radiotherapy for prostate carcinoma. *Cancer* 1997;80(6):1093-1102.
9. Bartoletti R, Meliani E, Bongini A, Magno C, Cai T. Fluorodeoxyglucose positron emission tomography may aid the diagnosis of aggressive primary prostate cancer: A case series study. *Oncology Letters* 2014;7(2):381-386.
10. Lee ST, Lawrentschuk N, Scott AM. PET in Prostate and Bladder Tumors. *Semin Nucl Med* 2012;42(4):231-246.
11. Ursula N, Wolfgang W, Michael H, Anca-Ligia G. Biological imaging in radiation therapy: role of positron emission tomography. *Phys Med Biol* 2009;54(1):R1.
12. Oyama N, Miller TR, Dehdashti F, Siegel BA, Fischer KC, Michalski JM, Kibel AS, Andriole GL, Picus J, Welch MJ. 11C-Acetate PET Imaging of Prostate Cancer: Detection of Recurrent Disease at PSA Relapse. *J Nucl Med* 2003;44(4):549-555.
13. Garcia JR, Romera N, Cozar M, Soler M, Moragas M, Escobar M. 11C-colina PET/TAC y RM multiparamétrica en la recidiva bioquímica del cáncer de próstata. *Actas Urol Esp* (0).
14. Cochet A, Kanoun S, Humbert O, Walker PM, Cormier L, Créhange G, Brunotte F. Quelle imagerie pour la prise en charge de la rechute biochimique du cancer de la prostate : TEP ou IRM ? *Cancer Radiother* 2014;18(5–6):509-516.
15. liu L, Wu N, Ouyang H, Dai J-R, Wang W-H. Diffusion-weighted MRI in early assessment of tumour response to radiotherapy in high-risk prostate cancer. *Brit J Radiol* 2014;87(1043):20140359.
16. Rud E, Baco E, Lien D, Klotz D, Eggesbø HB. Detection of Radiorecurrent Prostate Cancer Using Diffusion-Weighted Imaging and Targeted Biopsies. *Am J Roentgenol* 2014;202(3):W241-W246.
17. Gunnlaugsson A, Kjellen E, Hagberg O, Thellenberg-Karlsson C, Widmark A, Nilsson P. Change in prostate volume during extreme hypo-fractionation analysed with MRI. *Radiat Oncol* 2014;9(1):22.

18. Hall EJ, Giaccia, A. J. . Radiobiology for the Radiologist New York: Lippincott Williams & Wilkins; 2006.

19. Höckel M, Vaupel P. Tumor Hypoxia: Definitions and Current Clinical, Biologic, and Molecular Aspects. *J Natl Cancer I* 2001;93(4):266-276.

20. Gray L, Conger A, Ebert M, Hornsey S, Scott O. The concentration of oxygen dissolved in tissues at time of irradiation as a factor in radiotherapy. *Br J Radiol* 1953;26:638-648.

21. Khan FM. Treatment Planning in Radiation Oncology New York: Lippincott Williams & Wilkins; 2007.

22. Zhao D, Constantinescu A, Hahn EW, Mason RP. Tumor oxygen dynamics with respect to growth and respiratory challenge: investigation of the Dunning prostate R3327-HI tumor. *Radiat Res* 2001;156:510-520.

23. Zhao D, Constantinescu C, Hahn EW, Mason RP. Differential oxygen dynamics in two diverse Dunning prostate R3327 rat tumor sublines (MAT-Lu and HI) with respect to growth and respiratory challenge. *Int J Radiat Oncol Biol Phys* 2002;53(3):744-756.

24. Lyng H, Sundfør K, Rofstad E. Oxygen Tension in Human Squamous Cell Carcinoma and Adenocarcinoma of the Uterine Cervix. In: Hudetz A, Bruley D, editors. *Adv Exp Med Biol*. Volume 454, Advances in Experimental Medicine and Biology: Springer US; 1998. p 635-641.

25. Zhao D, Constantinescu A, Chang C-H, Hahn EW, Mason RP. Correlation of Tumor Oxygen Dynamics with Radiation Response of the Dunning Prostate R3327-HI Tumor. *Radiat Res* 2003;159:621-631.

26. Zhao D, Ran S, Constantinescu A, Hahn EW, Mason RP. Tumor oxygen dynamics: correlation of in vivo MRI with histological findings. *Neoplasia* 2003;5(4):308-318.

27. Movsas B, Chapman JD, Horwitz EM, Pinover WH, Greenberg RE, Hanlon AL, Iyer R, Hanks GE. Hypoxic regions exist in human prostate carcinoma. *Urology* 1999;53:11-18.

28. Movsas B, Chapman JD, Greenberg RE, Hanlon AL, Horwitz EM, Pinover WH, Stobbe C, Hanks GE. Increasing levels of hypoxia in prostate carcinoma correlate significantly with increasing clinical stage and patient age: an Eppendorf pO(2) study. *Cancer* 2000;89(9):2018-2024.

29. Movsas B, Chapman JD, Hanlon AL, Horwitz EM, Greenberg RE, Stobbe C, Hanks GE, Pollack A. Hypoxic prostate/muscle pO_2 ratio predicts for biochemical failure in patients with prostate cancer: preliminary findings. *Urology* 2002;60:634-639.

30. Tatum JL, Kelloff GJ, Gillies RJ, Arbeit JM, Brown JM, Chao KSC, Chapman JD, Eckelman WC, Fyles AW, Giaccia AJ, Hill RP, Koch CJ, Krishna MC, Krohn KA, Lewis JS, Mason RP, Melillo G, Padhani AR, Powis G, Rajendran JG, Reba R, Robinson SP, Semenza GL, Swartz HM, Vaupel P, Yang D, Croft B, Hoffman J, Liu GY, Stone H, Sullivan D. Hypoxia: Importance in tumor biology, noninvasive measurement by imaging, and value of its measurement in the management of cancer therapy. *Int J Radiat Biol* 2006;82(10):699-757.

31. Overgaard J. Hypoxic radiosensitization: Adored and ignored. *J Clin Oncol* 2007;25(26):4066-4074.

32. Krohn KA, Link JM, Mason RP. Molecular Imaging of Hypoxia. *J Nucl Med* 2008;49:129S-148S.

33. Hallac RR, Ding Y, Yuan Q, McColl RW, Lea J, Sims RD, Weatherall PT, Mason RP. Oxygenation in cervical cancer and normal uterine cervix assessed using

blood oxygenation level-dependent (BOLD) MRI at 3T. *NMR Biomed* 2012;25:1321–1330.

34.	Jiang L, Weatherall PT, McColl RW, Tripathy D, Mason RP. Blood oxygenation level-dependent (BOLD) contrast magnetic resonance imaging (MRI) for prediction of breast cancer chemotherapy response: A pilot study. *J Magn Reson Imaging* 2013;37:1083–1092.

35.	O'Connor JPB, Naish JH, Parker GJM, Waterton JC, Watson Y, Jayson GC, Buonaccorsi GA, Cheung S, Buckley DL, McGrath DM, West CML, Davidson SE, Roberts C, Mills SJ, Mitchell CL, Hope L, Ton C, Jackson A. Preliminary Study of Oxygen-Enhanced Longitudinal Relaxation in MRI: a Potential Novel Biomarker of Oxygenation Changes in Solid Tumors. *Int J Radiat Oncol Biol Phys* 2009;75(4):1209-1215.

36.	Zhang Z, Hallac RR, Peschke P, Mason RP. A noninvasive tumor oxygenation imaging strategy using magnetic resonance imaging of endogenous blood and tissue water. *Magn Reson Med* 2014;71(2):561-569.

37.	Hallac RR, Zhou H, Pidikiti R, Song K, Stojadinovic S, Zhao D, Solberg T, Peschke P, Mason RP. Correlations of noninvasive BOLD and TOLD MRI with pO2 and relevance to tumor radiation response. *Magn Reson Med* 2014;71(5):1863-1873.

38.	Peeters SGJA, Zegers CML, Lieuwes NG, van Elmpt W, Eriksson J, van Dongen GAMS, Dubois L, Lambin P. A Comparative Study of the Hypoxia PET Tracers [18F]HX4, [18F]FAZA, and [18F]FMISO in a Preclinical Tumor Model. *Int J Radiat Oncol Biol Phys* 2015;91(2):351-359.

39.	Matsuo M, Matsumoto S, Mitchell JB, Krishna MC, Camphausen K. Magnetic Resonance Imaging of the Tumor Microenvironment in Radiotherapy: Perfusion, Hypoxia, and Metabolism. *Semin Radiat Oncol* 2014;24(3):210-217.

40.	Jordan BF, Magat J, Colliez F, Ozel E, Fruytier A-C, Marchand V, Mignion L, Bouzin C, Cani PD, Vandeputte C, Feron O, Delzenne N, Himmelreich U, Denolin V, Duprez T, Gallez B. Mapping of oxygen by imaging lipids relaxation enhancement: A potential sensitive endogenous MRI contrast to map variations in tissue oxygenation. *Magn Reson Med* 2013;70(3):732-744.

41.	Colliez F, Neveu M-A, Magat J, Cao Pham TT, Gallez B, Jordan BF. Qualification of a Noninvasive Magnetic Resonance Imaging Biomarker to Assess Tumor Oxygenation. *Clin Cancer Res* 2014;20(21):5403-5411.

42.	Almos H. Dosimetry and Treatment Planning for Three-Dimensional Radiation Therapy. *Encyclopedia of Cancer*. 2nd ed. Volume 22002. p 109-118.

43.	Timmerman R, Paulus R, Galvin J, Michalski J, Straube W, Bradley J, Fakiris A, Bezjak A, Videtic G, Johnstone D, Fowler J, Gore E, Choy H. Stereotactic Body Radiation Therapy for Inoperable Early Stage Lung Cancer. *JAMA* 2010;303(11):1070-1076.

44.	Carlson DJ, Keall PJ, Loo BW, Chen ZJ, Brown JM. Hypofractionation Results in Reduced Tumor Cell Kill Compared to Conventional Fractionation for Tumors with Regions of Hypoxia. *Int J Radiat Oncol Biol Phys* 2011;79(4):1188-1195.

45.	Brown JM, Diehn M, Loo BW. Stereotactic Ablative Radiotherapy Should Be Combined with a Hypoxic Cell Radiosensitizer. *Int J Radiat Oncol Biol Phys*;78(2):323-327.

46.	Zhao D, Jiang L, Mason RP. Measuring Changes in Tumor Oxygenation. *Methods Enzymol* 2004;386:378-418.

47. Zhao D, Jiang L, Hahn EW, Mason RP. Comparison of ^{1}H blood oxygen level-dependent (BOLD) and ^{19}F MRI to investigate tumor oxygenation. *Magn Reson Med* 2009;62(2):357-364.

48. Mason RP, Zhao D, Pacheco-Torres J, Cui W, Kodibagkar VD, Gulaka PK, Hao G, Thorpe P, Hahn EW, Peschke P. Multimodality imaging of hypoxia in preclinical settings. *QJ Nucl Med Mol Imaging* 2010;54:259-280.

49. Zhang Z, Hallac RR, Peschke P, Mason RP. A noninvasive tumor oxygenation imaging strategy using magnetic resonance imaging of endogenous blood and tissue water. *Magn Reson Med* 2014;71(2):561-569.

50. Fenton B, Paoni S, Koch C, Lord E. Effect of Local Irradiation on Tumor Oxygenation, Perfused Vessel Density, and Development of Hypoxia. In: Hudetz A, Bruley D, editors. *Adv Exp Med Biol*. Volume 454, Advances in Experimental Medicine and Biology: Springer US; 1998. p 619-628.

51. O'Connor JPB, Naish JH, Jackson A, Waterton JC, Watson Y, Cheung S, Buckley DL, McGrath DM, Buonaccorsi GA, Mills SJ, Roberts C, Jayson GC, Parker GJM. Comparison of normal tissue R1 and R*2 modulation by oxygen and carbogen. *Magn Reson Med* 2009;61(1):75-83.

52. O'Connor JPB, Jackson A, Buonaccorsi GA, Watson Y, Cheung S, Jayson GC, Parker JG. Modulation of Tumour R1: A Novel Biomarker of Oxygenation Status. 2008; Toronto. p 1444.

53. Vaupel P, Thews O, Kelleher DK, Hoeckel M. Current Status of Knowledge and Critical Issues in Tumor Oxygenation. In: Hudetz A, Bruley D, editors. *Adv Exp Med Biol*. Volume 454, Advances in Experimental Medicine and Biology: Springer US; 1998. p 591-602.

54. Wilson D, Evans S, Jenkins W, Vinogradov S, Ong E, Dewhirst M. Oxygen Distributions within R3230AC Tumors Growing in Dorsal Flap Window Chambers in Rats. In: Hudetz A, Bruley D, editors. *Adv Exp Med Biol*. Volume 454, Advances in Experimental Medicine and Biology: Springer US; 1998. p 603-609.

55. Giancoli DC. Physics for Scientists and Engineers: Pearson Education; 2008.

56. Pittman R. Regulation of Tissue Oxygenation: Biota Publishing; 2011.

57. Silverthorn DU. Human Physiology: An Integrated Approach 4th Edition: Pearson/Benjamin Cummings; 2007. Print.

58. Garrett R, Grisham C. Biochemistry: Cengage Learning; 2008.

59. Hall EJ, Giaccia AJ. Radiobiology for the Radiologist. New York: Lippincott Williams & Wilkins; 2012.

60. Khan FM. The Physics of Radiation Therapy: Lippincott Williams & Wilkins; 2010.

61. Griffiths DJ. Introduction To Electrodynamics 3/e: Pearson Education; 2006.

62. Nishimura DG. Principles of magnetic resonance imaging: Stanford University; 1996.

63. Silverthorn DU. Human Physiology: An Integrated Approach: Pearson/Benjamin Cummings; 2007.

64. Popel AS. Theory of oxygen transport to tissue. *Crit Rev Biomed Eng* 1989;17(3):257-321.

65. Vaupel P. Tumor microenvironmental physiology and its implications for radiation oncology. *Semin Radiat Oncol* 2004;14(3):198-206.

66. Tatum JL. Hypoxia: Importance in tumor biology, noninvasive measurement by imaging, and value of its measurement in the management of cancer therapy. *Int J Radiat Biol* 2006;82(10):699-757.

67.   Horsman MR, Mortensen LS, Petersen JB, Busk M, Overgaard J. Imaging hypoxia to improve radiotherapy outcome. *Nat Rev Clin Oncol* 2012;9(12):674-687.

68.   Vaupel P, Kallinowski F, Okunieff P. Blood Flow, Oxygen and Nutrient Supply, and Metabolic Microenvironment of Human Tumors: A Review. *Cancer Res* 1989;49(23):6449-6465.

69.   Secomb TW, Hsu R, Dewhirst MW, Klitzman B, Gross JF. Analysis of oxygen transport to tumor tissue by microvascular networks. *Int J Radiat Oncol Biol Phys* 1993;25(3):481-489.

70.   Degner FL, Sutherland RM. Mathematical modelling of oxygen supply and oxygenation in tumor tissues: Prognostic, therapeutic, and experimental implications. *Int J Radiat Oncol Biol Phys* 1988;15(2):391-397.

71.   Groebe K, Vaupel P. Evaluation of oxygen diffusion distances in human breast cancer xenografts using tumor-specific in vivo data: Role of various mechanisms in the development of tumor hypoxia. *Int J Radiat Oncol Biol Phys* 1988;15(3):691-697.

72.   Dewhirst MW, Secomb TW, Ong ET, Hsu R, Gross JF. Determination of Local Oxygen Consumption Rates in Tumors. *Cancer Res* 1994;54(13):3333-3336.

73.   Gu Y, Bourke V, Kim JG, Constantinescu A, Mason RP, Liu H. Dynamic Response of Breast Tumor Oxygenation to Hyperoxic Respiratory Challenge Monitored with Three Oxygen-Sensitive Parameters. *Appl Optics* 2003;42:1-8.

74.   Thornton S, Rex A. Modern Physics for Scientists and Engineers: Cengage Learning; 2012.

75.   Hall EJ, Brown JM, Cavanagh J. Radiosensitivity and the Oxygen Effect Measured at Different Phases of the Mitotic Cycle Using Synchronously Dividing Cells of the Root Meristem of Vicia faba. *Radiat Res* 1968;35(3):622-634.

76.   Legrys GA, Hall EJ. The Oxygen Effect and X-Ray Sensitivity in Synchronously Dividing Cultures of Chinese Hamster Cells. *Radiat Res* 1969;37(1):161-172.

77.   Freyer JP, Jarrett K, Carpenter S, Raju MR. Oxygen Enhancement Ratio as a Function of Dose and Cell Cycle Phase for Radiation-Resistant and Sensitive CHO Cells. *Radiat Res* 1991;127(3):297-307.

78.   Podgoršak EB, Agency IAE. Radiation Oncology Physics: A Handbook for Teachers and Students: International Atomic Energy Agency; 2005.

79.   Michael RH, Bradly CW, Michael CJ, Jens O. The oxygen effect and fractionated radiotherapy. Basic Clinical Radiobiology Fourth Edition: CRC Press; 2009. p 207-216.

80.   Palcic B, Skarsgard LD. Reduced Oxygen Enhancement Ratio at Low Doses of Ionizing Radiation. *Radiat Res* 1984;100(2):328-339.

81.   Fyles A, Milosevic M, Hedley D, Pintilie M, Levin W, Manchul L, Hill RP. Tumor Hypoxia Has Independent Predictor Impact Only in Patients With Node-Negative Cervix Cancer. *J Clin Oncol* 2002;20(3):680-687.

82.   Parker C, Milosevic M, Toi A, Sweet J, Panzarella T, Bristow R, Catton C, Catton P, Crook J, Gospodarowicz M, McLean M, Warde P, Hill RP. Polarographic electrode study of tumor oxygenation in clinically localized prostate cancer. *Int J Radiat Oncol Biol Phys* 2004;58(3):750-757.

83.   Movsas B, Chapman JD, Hanlon AL, Horwitz EM, Greenberg RE, Stobbe C, Hanks GE, Pollack A. Hypoxic prostate/muscle po2 ratio predicts for biochemical failure in patients with prostate cancer: preliminary findings. *Urology* 2002;60(4):634-639.

84. Jordan BF, Sonveaux P. Targeting tumor perfusion and oxygenation to improve the outcome of anticancer therapy. *Frontiers in Pharmacology* 2012;3.

85. Horii K, Suzuki Y, Kondo Y, Akimoto M, Nishimura T, Yamabe Y, Sakaue M, Sano T, Kitagawa T, Himeno S, Imura N, Hara S. Androgen-Dependent Gene Expression of Prostate-Specific Antigen Is Enhanced Synergistically by Hypoxia in Human Prostate Cancer Cells. *Mol Cancer Res* 2007;5(4):383-391.

86. Johns HE, Cunningham, J. R. Physics of Radiology. Springfield, Illinois: Charles C Thomas; 1983.

87. Dewhirst MW, Oliver R, Tso CY, Gustafson C, Secomb T, Gross JF. Heterogeneity in tumor microvascular response to radiation. *Int J Radiat Oncol Biol Phys* 1990;18(3):559-568.

88. Diepart C, Karroum O, Magat J, Feron O, Verrax J, Calderon PB, Grégoire V, Leveque P, Stockis J, Dauguet N, Jordan BF, Gallez B. Arsenic Trioxide Treatment Decreases the Oxygen Consumption Rate of Tumor Cells and Radiosensitizes Solid Tumors. *Cancer Res* 2012;72(2):482-490.

89. Song CW, Levitt SH. Vascular Changes in Walker 256 Carcinoma of Rats Following X Irradiation. *Radiology* 1971;100(2):397-407.

90. Perez CA, Vijayakumar S. Technical Basis of Radiation Therapy: Springer-Verlag; 2006.

91. Kocher M, Treuer H, Voges J, Hoevels M, Sturm V, Müller R-P. Computer simulation of cytotoxic and vascular effects of radiosurgery in solid and necrotic brain metastases. *Radiother Oncol* 2000;54(2):149-156.

92. Kirkpatrick JP, Meyer JJ, Marks LB. The Linear-Quadratic Model Is Inappropriate to Model High Dose per Fraction Effects in Radiosurgery. *Semin Radiat Oncol* 2008;18(4):240-243.

93. Gerweck LE, Hetzel FW. PO2 in irradiated versus nonirradiated tumors of mice breathing oxygen at normal and elevated pressure. *Int J Radiat Oncol Biol Phys* 1995;32(3):695-701.

94. Rice BW, Cable MD, Nelson MB. In vivo imaging of light-emitting probes. *J Biomed Opt* 2001;6(4):432-440.

95. Feng DD. Biomedical Information Technology: Elsevier Science; 2011.

96. Bloch F. Nuclear induction. *Physica* 1951;17(3–4):272-281.

97. Young IR, Clarke GJ, Bailes DR, Pennock JM, Doyle FH, Bydder GM. Enhancement of Relaxation Rate with Paramagnetic Contrast Agents in NMR Imaging. *J Comp Tomogr* 1981;5(6):543-547.

98. Chopra S, Foltz WD, Milosevic MF, Toi A, Bristow RG, Menard C, Haider MA. Comparing oxygen-sensitive MRI (BOLD R_2*) with oxygen electrode measurements: A pilot study in men with prostate cancer. *Int J Radiat Biol* 2009;85(9):805 - 813.

99. Baudelet C, Gallez B. How does blood oxygen level-dependent (BOLD) contrast correlate with oxygen partial pressure (pO$_2$) inside tumors? *Magn Reson Med* 2002;48(6):980-986.

100. Howe FA, Robinson SP, Rodrigues LM, Griffiths JR. Flow and oxygenation dependent (FLOOD) contrast MR imaging to monitor the response of rat tumors to carbogen breathing. *Magn Reson Imaging* 1999;17(9):1307-1318.

101. Howe FA, Robinson SP, McIntyre DJO, Stubbs M, Griffiths JR. Issues in flow and oxygenation dependent contrast (FLOOD) imaging of tumours. *NMR Biomed* 2001;14(7-8):497-506.

102. Howe FA, Robinson SP, Griffiths JR. 100% N$_2$ breathing causes vascular collapse in some subcutaneous tumors. 2000; Denver. p 1043.

103. Jordan BF, Crokart N, Baudelet C, Cron GO, Ansiaux R, Gallez B. Complex relationship between changes in oxygenation status and changes in R-2(*): The case of insulin and NS-398, two inhibitors of oxygen consumption. *Magn Reson Med* 2006;56(3):637-643.

104. Zabala M, Alzuguren P, Benavides C, Crettaz J, Gonzalez-Aseguinolaza G, Ortiz de Solorzano C, Gonzalez-Aparicio M, Kramer M, Prieto J, Hernandez-Alcoceba R. Evaluation of bioluminescent imaging for noninvasive monitoring of colorectal cancer progression in the liver and its response to immunogene therapy. *Mol Cancer* 2009;8(1):2.

105. Zhang J, Hu H, Liang S, Yin J, Hui X, Hu S, He M, Wang J, Wang B, Nie Y, Wu K, Ding J. Targeted radiotherapy with tumor vascular homing trimeric GEBP11 peptide evaluated by multimodality imaging for gastric cancer. *J Control Release* 2013;172(1):322-329.

106. Zinn KR, Chaudhuri TR, Szafran AA, O'Quinn D, Weaver C, Dugger K, Lamar D, Kesterson RA, Wang X, Frank SJ. Noninvasive Bioluminescence Imaging in Small Animals. ILAR Journal 2008;49(1):103-115.

107. Munley MT, Kagadis GC, McGee KP, Kirov AS, Jang S, Mutic S, Jeraj R, Xing L, Bourland JD. An introduction to molecular imaging in radiation oncology: a report by the AAPM Working Group on Molecular Imaging in Radiation Oncology (WGMIR). *Med Phys* 2013;40(10):101501.

108. Tomayko MM, Reynolds CP. Determination of subcutaneous tumor size in athymic (nude) mice. *Cancer Chemother Pharmacol* 1989;24(3):148-154.

109. Khalil AA, Jameson MJ, Broaddus WC, Lin PS, Dever SM, Golding SE, Rosenberg E, Valerie K, Chung TD. The Influence of Hypoxia and pH on Bioluminescence Imaging of Luciferase-Transfected Tumor Cells and Xenografts. *Int J Mol Imaging* 2013;2013:9.

110. Brutkiewicz S, Mendonca M, Stantz K, Comerford K, Bigsby R, Hutchins G, Goebl M, Harrington M. The expression level of luciferase within tumour cells can alter tumour growth upon in vivo bioluminescence imaging. *Luminescence* 2007;22(3):221-228.

111. Welsh DK, Noguchi T. Cellular Bioluminescence Imaging. *Cold Spring Harb Protoc* 2012;2012(8):pdb.top070607.

112. Klerk CP, Overmeer RM, Niers TM, Versteeg HH, Richel DJ, Buckle T, Van Noorden CJ, van Tellingen O. Validity of bioluminescence measurements for noninvasive in vivo imaging of tumor load in small animals. *Biotechniques* 2007;43(1 Suppl):7-13, 30.

113. Puaux AL, Ong LC, Jin Y, Teh I, Hong M, Chow PK, Golay X, Abastado JP. A comparison of imaging techniques to monitor tumor growth and cancer progression in living animals. *Int J Mol Imaging* 2011;2011:321538.

114. Alhasan MK, Liu L, Lewis MA, Magnusson J, Mason RP. Comparison of Optical and Power Doppler Ultrasound Imaging for Non-Invasive Evaluation of Arsenic Trioxide as a Vascular Disrupting Agent in Tumors. *PLoS One* 2012;7(9):e46106.

115. Contero A, Richer E, Gondim A, Mason RP. High-throughput quantitative bioluminescence imaging for assessing tumor burden. *Methods Mol Biol* 2009;574:37-45.

116. Jenkins DE, Oei Y, Hornig YS, Yu SF, Dusich J, Purchio T, Contag PR. Bioluminescent imaging (BLI) to improve and refine traditional murine models of tumor growth and metastasis. *Clin Exp Metastasis* 2003;20(8):733-744.

117. Osorio F, de la Rosa J, Freije JM. Luminescence-based in vivo monitoring of NF-kappaB activity through a gene delivery approach. *Cell Commun Signal* 2013;11(1):19.
118. Park J, Jang S, Kang S, Park S, Hwang S-G, Kim W-J, Kang J, Um H-D. Establishment of animal model for the analysis of cancer cell metastasis during radiotherapy. *Radiat Oncol* 2012;7(1):153.
119. Thorne SH, Contag CH. Using in Vivo Bioluminescence Imaging to Shed Light on Cancer Biology. *P IEEE* 2005;93(4):750-762.
120. Rehemtulla A, Stegman LD, Cardozo SJ, Gupta S, Hall DE, Contag CH, Ross BD. Rapid and quantitative assessment of cancer treatment response using in vivo bioluminescence imaging. *Neoplasia* 2000;2(6):491-495.
121. Tuli R, Armour M, Surmak A, Reyes J, Iordachita I, Patterson M, Wong J. Accuracy of Off-Line Bioluminescence Imaging to Localize Targets in Preclinical Radiation Research. *Radiat Res* 2012;179(4):416-421.
122. Mullen P. The Use of Matrigel to Facilitate the Establishment of Human Cancer Cell Lines as Xenografts. In: Langdon S, editor. *Cancer Cell Culture*. Volume 88, Methods in Molecular Medicine™: Humana Press; 2004. p 287-292.
123. Kaighn ME, Narayan KS, Ohnuki Y, Lechner JF, Jones LW. Establishment and characterization of a human prostatic carcinoma cell line (PC-3). *Invest Urol* 1979;17(1):16-23.
124. Lein M, Jung K, Le DK, Hasan T, Ortel B, Borchert D, Winkelmann B, Schnorr D, Loenings SA. Synthetic inhibitor of matrix metalloproteinases (batimastat) reduces prostate cancer growth in an orthotopic rat model. *Prostate* 2000;43(2):77-82.
125. Heitjan DF, Manni A, Santen RJ. Statistical analysis of in vivo tumor growth experiments. *Cancer Res* 1993;53(24):6042-6050.
126. Hallac RR, Zhou H, Pidikiti R, Song K, Stojadinovic S, Zhao D, Solberg T, Peschke P, Mason RP. Correlations of noninvasive BOLD and TOLD MRI with pO2 and relevance to tumor radiation response. *Magn Reson Med* 2013.
127. Jensen MM, Jorgensen JT, Binderup T, Kjaer A. Tumor volume in subcutaneous mouse xenografts measured by microCT is more accurate and reproducible than determined by 18F-FDG-microPET or external caliper. *BMC Med Imaging* 2008;8:16.
128. Paroo Z, Bollinger RA, Braasch DA, Richer E, Corey DR, Antich PP, Mason RP. Validating bioluminescence imaging as a high-throughput, quantitative modality for assessing tumor burden. *Mol Imaging* 2004;3(2):117-124.
129. Jost SC, Collins L, Travers S, Piwnica-Worms D, Garbow JR. Measuring brain tumor growth: combined bioluminescence imaging-magnetic resonance imaging strategy. *Mol Imaging* 2009;8(5):245-253.
130. Tiffen J, Bailey C, Ng C, Rasko J, Holst J. Luciferase expression and bioluminescence does not affect tumor cell growth in vitro or in vivo. *Mol Cancer* 2010;9(1):299.
131. Andresen C CB, Pero R, Brightwell A, Bagi C. NIH/rnu: Are They All Created Equal? A Comparison of Taconic and Charles River Rat Strains. a poster session presented at the 59th meeting of the American Association for Laboratory Animal Science, Indianapolis, IN.2008.
132. Moriyama EH, Niedre MJ, Jarvi MT, Mocanu JD, Moriyama Y, Subarsky P, Li B, Lilge LD, Wilson BC. The influence of hypoxia on bioluminescence in luciferase-transfected gliosarcoma tumor cells in vitro. *Photoch Photobio Sci* 2008;7(6):675-680.

133. Burgos JS, Rosol M, Moats RA, Khankaldyyan V, Kohn DB, Nelson MD, Jr., Laug WE. Time course of bioluminescent signal in orthotopic and heterotopic brain tumors in nude mice. *Biotechniques* 2003;34(6):1184-1188.

134. Jiang L, Zhao D, Constantinescu A, Mason RP. Comparison of BOLD contrast and Gd-DTPA Dynamic Contrast Enhanced imaging in rat prostate tumor. *Magn Reson Med* 2004;51:953-960.

135. Matsumoto K, Bernardo M, Subramanian S, Choyke P, Mitchell JB, Krishna MC, Lizak MJ. MR assessment of changes of tumor in response to hyperbaric oxygen treatment. *Magn Reson Med* 2006;56(2):240-246.

136. Zhao D, Jiang L, Hahn EW, Mason RP. Comparison of 1H blood oxygen level-dependent (BOLD) and 19F MRI to investigate tumor oxygenation. *Magn Reson Med* 2009;62(2):357-364.

137. Ding Y, Mason RP, McColl RW, Yuan Q, Hallac RR, Sims RD, Weatherall PT. Simultaneous measurement of tissue oxygen level-dependent (TOLD) and blood oxygenation level-dependent (BOLD) effects in abdominal tissue oxygenation level studies. *J Magn Reson Imaging* 2013;38(5):1230-1236.

138. Burrell JS, Walker-Samuel S, Baker LCJ, Boult JKR, Jamin Y, Halliday J, Waterton JC, Robinson SP. Exploring ΔR2* and ΔR1 as imaging biomarkers of tumor oxygenation. *J Magn Reson Imaging* 2013;38(2):429-434.

139. Ogawa S, Lee TM, Kay AR, Tank DW. Brain magnetic resonance imaging with contrast dependent on blood oxygenation. *Proc Natl Acad Sci* 1990;87:9868-9872.

140. Alonzi R, Padhani AR, Maxwell RJ, Taylor NJ, Stirling JJ, Wilson JI, d'Arcy JA, Collins DJ, Saunders MI, Hoskin PJ. Carbogen breathing increases prostate cancer oxygenation: a translational MRI study in murine xenografts and humans. *Br J Cancer* 2009;100(4):644-648.

141. Diergarten T, Martirosian P, Kottke R, Vogel U, Stenzl A, Claussen CD, Schlemmer HP. Functional characterization of prostate cancer by integrated magnetic resonance imaging and oxygenation changes during carbogen breathing. *Invest Radiol* 2005;40(2):102-109.

142. Peschke P, Hahn EW, Wenz F, Lohr F, Braunschweig F, Wolber G, Zuna I, Wannenmacher M. Differential Sensitivity of Three Sublines of the Rat Dunning Prostate Tumor System R3327 to Radiation and/or Local Tumor Hyperthermia. *Radiat Res* 1998;150(4):423-430.

143. Alexopoulos EC. Introduction to multivariate regression analysis. *Hippokratia* 2010;14(Suppl 1):23-28.

144. Zhao D, Constantinescu A, Jiang L, Hahn EW, Mason RP. Prognostic Radiology: quantitative assessment of tumor oxygen dynamics by MRI. *Am J Clin Oncol* 2001;24:462-466.

145. Bourke VA, Zhao D, Gilio J, Chang C-H, Jiang L, Hahn EW, Mason RP. Correlation of Radiation Response with Tumor Oxygenation in the Dunning Prostate R3327-AT1 Tumor. *Int J Radiat Oncol Biol Phys* 2007;67(4):1179-1186.

146. Zhao D, Pacheco Torres J, Peschke P, Mason RP. DOCENT-Dynamic Oxygen Challenge Evaluated by NMR T1 and T2* of Tumors. 2007; Jackon, WY. p 16.

147. Pacheco-Torres J, Zhao D, Contero A, Peschke P, Mason RP. DOCENT-Dynamic Oxygen Challenge Evaluated by NMR T_1 and T_2* of Tumors. 2008; Toronto, Canada p450.

148. Millikan GA. The Oximeter, an Instrument for Measuring Continuously the Oxygen Saturation of Arterial Blood in Man. *Rev Sci Instrum* 1942;13(10):434-444.

149.   Lu H, Xu F, Grgac K, Liu P, Qin Q, van Zijl P. Calibration and validation of TRUST MRI for the estimation of cerebral blood oxygenation. *Magn Reson Med* 2012;67(1):42-49.

150.   Tanen DA, Trocinski DR. The use of pulse oximetry to exclude pneumonia in children. *Am J Emerg Med* 2002;20(6):521-523.

151.   Panacek EA. The use of pulse oximetry in the emergency department. *J Emerg Med* 1995;13(6):816-817.

152.   White D, Mason RP. Non-invasive pre-clinical MR imaging of prostate tumor hypoxia for radiation therapy prognosis. *Int J Cancer Ther Oncol* 2014;2(2):020243.

153.   Ling CC, Humm J, Larson S, Amols H, Fuks Z, Leibel S, Koutcher JA. Towards multidimensional radiotherapy (MD-CRT): biological imaging and biological conformality. *Int J Radiat Oncol Biol Phys* 2000;47(3):551-560.

154.   Rodrigues LM, Howe FA, Griffiths JR, Robinson SP. Tumor R2* is a prognostic indicator of acute radiotherapeutic response in rodent tumors. *J Magn Reson Imaging* 2004;19(4):482-488.

155.   O'Hara JA, Goda F, Demidenko E, Swartz HM. Effect on Regrowth Delay in a Murine Tumor of Scheduling Split-Dose Irradiation Based on Direct [image] Measurements by Electron Paramagnetic Resonance Oximetry. *Radiat Res* 1998;150(5):549-556.

156.   Isaacs JT, Heston WD, Weissman RM, Coffey DS. Animal models of the hormone-sensitive and -insensitive prostatic adenocarcinomas, Dunning R-3327-H, R-3327-HI, and R-3327-AT. *Cancer Res* 1978;38(11 Pt 2):4353-4359.

157.   Karger CP, Peschke P, Scholz M, Huber PE, Debus J. Relative Biological Effectiveness of Carbon Ions in a Rat Prostate Carcinoma In Vivo: Comparison of 1, 2, and 6 Fractions. *Int J Radiat Oncol Biol Phys* 2013;86(3):450-455.

158.   Yeh KA, Biade S, Lanciano RM, Brown DQ, Fenning MC, Babb JS, Hanks GE, Chapman JD. Polarographic needle electrode measurements of oxygen in rat prostate carcinomas: Accuracy and reproducibility. *Int J Radiat Oncol Biol Phys* 1995;33(1):111-118.

159.   Ljungkvist ASE, Bussink J, Kaanders JHAM, Rijken PFJW, Begg AC, Raleigh JA, van der Kogel AJ. Hypoxic cell turnover in different solid tumor lines. *Int J Radiat Oncol Biol Phys* 2005;62(4):1157-1168.

160.   Ljungkvist ASE, Bussink J, Kaanders J, Wiedenmann NE, Vlasman R, van der Kogel AJ. Dynamics of hypoxia, proliferation and apoptosis after irradiation in a murine tumor model. *Radiat Res* 2006;165(3):326-336.

161.   Ljungkvist ASE, Bussink J, Kaanders J, Van der Kogel AJ. Dynamics of tumor hypoxia measured with bioreductive hypoxic cell markers. *Radiat Res* 2007;167(2):127-145.

162.   Bandettini PA, Jesmanowicz A, Wong EC, Hyde JS. Processing strategies for time-course data sets in functional mri of the human brain. *Magn Reson Med* 1993;30(2):161-173.

163.   Mai VM, Tutton S, Prasad PV, Chen Q, Li W, Chen C, Liu B, Polzin J, Kurucay S, Edelman RR. Computing oxygen-enhanced ventilation maps using correlation analysis. *Magn Reson Med* 2003;49(3):591-594.

164.   Kaplan EL, Meier P. Nonparametric Estimation from Incomplete Observations. *J Am Stat Assoc* 1958;53(282):457-481.

165.   Kutner MH, Nachtsheim CJ, Neter J, Li W. Applied Linear Statistical Models: McGraw Hill; 2005.

166. Fuchsjäger MH, Pucar D, Zelefsky MJ, Zhang Z, Mo Q, Ben-Porat LS, Shukla-Dave A, Wang L, Reuter VE, Hricak H. Predicting Post–External Beam Radiation Therapy PSA Relapse of Prostate Cancer Using Pretreatment MRI. *Int J Radiat Oncol Biol Phys* 2010;78(3):743-750.

167. Gneiting T. Making and Evaluating Point Forecasts. *J Am Stat Assoc* 2011;106(494):746-762.

168. Bienz M, Hueber P-A, Al-Hathal N, McCormack M, Bhojani N, Trinh Q-D, Zorn KC. Accuracy of Transrectal Ultrasonography to Evaluate Pathologic Prostate Weight: Correlation With Various Prostate Size Groups. *Urology* 2014;84(1):169-174.

169. Peng J, Ran Z, Shen J. Seasonal variation in onset and relapse of IBD and a model to predict the frequency of onset, relapse, and severity of IBD based on artificial neural network. *Int J Colorectal Dis* 2015:1-7.

170. Wei C-H, Lee Y. Sequential forecast of incident duration using Artificial Neural Network models. *Accident Anal Prev* 2007;39(5):944-954.

171. Stuschke M, Budach V, Bamberg M, Budach W. Methods for Analysis of Censored Tumor Growth Delay Data. *Radiat Res* 1990;122(2):172-180.

172. Hosmer DW, Lemeshow S, Sturdivant RX. Wiley Series in Probability and Statistics : Applied Logistic Regression (3rd Edition). New York, NY, USA: John Wiley & Sons; 2013.

173. von Neubeck C. Radiobiological Experiments for Carbon Ion Prostate Cancer Therapy: Interplay of Normal and Tumor Cells in Co-culture and Measurement of the Oxygen Enhancement Ratio: GSI; 2009.

174. Mangoni M, Desideri I, Detti B, Bonomo P, Greto D, Paiar F, Simontacchi G, Meattini I, Scoccianti S, Masoni T, Ciabatti C, Turkaj A, Serni S, Minervini A, Gacci M, Carini M, Livi L. Hypofractionation in Prostate Cancer: Radiobiological Basis and Clinical Appliance. *BioMed Research International* 2014;2014:8.

175. Kim DNW, Straka C, Cho LC, Timmerman RD. Stereotactic Body Radiation Therapy for Prostate Cancer: Review of Experience of a Multicenter Phase I/II Dose Escalation Study. *Front Oncol* 2014;4.

176. Tree AC, Ostler P, Hoskin P, Dankulchai P, Nariyangadu P, Hughes RJ, Wells E, Taylor H, Khoo VS, van As NJ. Prostate Stereotactic Body Radiotherapy — First UK Experience. *Clin Oncol* 2014;26(12):757-761.

177. Cho LC, Timmerman R, Kavanagh B. Hypofractionated External-Beam Radiotherapy for Prostate Cancer. *Prostate Cancer* 2013;2013:11.

178. Hall EJ, Lehnert S, Roizin-Towle L. Split-Dose Experiments with Hypoxic Cells. *Radiology* 1974;112(2):425-430.

179. Ling CC, Robinson E. Moderate Hyperthermia and Low Dose Rate Irradiation. *Radiat Res* 1988;114(2):379-384.

Biographical Information

During Derek's tenth grade year in high school, one of his sisters who was a mechanical engineer inquired if Derek wanted to go into engineering and further explained what engineers did. After Derek researched different engineering fields, he mentioned to his sister that he was interested in the field of biomedical engineering mainly because he really liked math, science, and medicine and how they are integrated. In addition, Derek was very interested in the design and creation of new technology through research for persons in need of a better life. Personal reasons prevented Derek from pursuing that path. He married his high school sweet heart and immediately started a family. During that time, he worked full-time and attended college on a part-time basis. After taking a position with the City of DeSoto, Texas as an engineering technician, Derek decided to pursue civil engineering as a career and began to attend college full-time while working full-time. Derek's employer was gracious enough to allow him to make up time as needed. Derek completed a Bachelors and Masters in Civil Engineering and a few years later completed his goal to become a Licensed Professional Engineer in the State of Texas. After being laid-off after working 12 years as a Civil Engineer, Derek decided to pursue his doctoral degree in Biomedical Engineering and seek a hybrid independent research and clinical career in medical physics using advanced imaging techniques to improve radiotherapy treatment planning systems. Derek went to conferences to present posters and give oral presentations based on his studies in hypoxia imaging and tumor radiobiology. Derek won 2nd place at the AAPM Southwest Chapter's Young Investigators Symposium for his oral presentation on his submitted abstract in Spring 2014.